A MAGNETIC PAIR SPECTROMETER TO DETECT PHOTON SPLITTING

A Thesis

Submitted to the College of Graduate Studies and Research

in Partial Fulfillment of the Requirements

for the Degree of Master of Science

in the

Department of Physics and

Engineering Physics

University of Saskatchewan

by

James R. Sigurdson

Saskatoon, Saskatchewan

Canada

Fall, 1994

In presenting this thesis in partial fulfillment of the requirements for a postgraduate degree from the University of Saskatchewan, I agree that the libraries of this university may make it freely available for inspection. I further agree that permission for copying of this thesis in any manner, in whole or in part, for scholarly purposes may be granted by the Head of the Department or the Dean of the College in which my thesis work was done. It is understood that any copying or publication or use of this thesis or parts thereof for financial gain shall not be allowed without my written permission. It is also understood that due recognition shall be given to me and to the University of Saskatchewan in any scholarly use which may be made of any material in my thesis.

Requests for permission to copy or to make other use of material in this thesis in whole or in part should be addressed to:

Head of the Department of Physics

University of Saskatchewan

Saskatoon, Saskatchewan

Canada S7N 0W0

ABSTRACT

The subject of this thesis is the calibration, energy resolution and efficiency of a magnetic gamma ray pair spectrometer (PS), investigated using the photon tagger at the Saskatchewan Accelerator Laboratory (SAL). This instrument employs the well known process of pair production, with subsequent momentum analysis of the electron-positron pair to reconstruct the photon's energy.

Tagged photons impinged on different thicknesses and geometries of copper converters. The resulting charged pairs were recorded by six scintillation detectors (three per focal plane) that were positioned on the focal planes of the pair spectrometer dipole magnet. The total energy of the pair was compared to the photon energy according to the tagger. An adjustable iris and annular scintillation detector were placed at the outrun of the pair spectrometer to study beam halo.

The PS design specifications were dictated by the need to perform the first reliable observations on a process known as photon splitting. This phenomenon is characterized by the dissociation (in the electric field of a nucleus) of an incoming photon having energy ω_1 into two real photons whose energy sum ($\omega_2 + \omega_3$) is equal to that of the incident photon. This process is predicted by the theory of quantum electrodynamics and is a consequence of vacuum polarization. A secondary goal was to use this PS in the related experiment of Delbrück scattering. The PS can also be used as a beam monitor for diagnostic purposes and for photon tagger energy calibrations in the energy regime between 20 - 160 MeV.

The energy resolution is less than 2.0 MeV (FWHM) and the energy calibration of the pair spectrometer is within 1 MeV of the SAL tagger. The efficiency of the device is strongly dependent on small angle multiple scattering in the converter and the number of focal plane detectors (energy acceptance) but is sufficiently high to warrant use in an experiment on photon splitting. Simulations are presented that agree with experimental results. Recent results (1994) are given using the final configuration of the PS in energy calibration tests on the SAL photon tagger.

ACKNOWLEDGEMENTS

I would like to thank Dennis Skopik, the director of the Saskatchewan Accelerator Laboratory, for giving me the opportunity to work here (as an operator at first) and always being positive in his efforts. Initially it was an accelerator operator and long time friend James Keil who informed me about the possibilities at this first class facility. Without these two people I may have never had the opportunity to be a part of SAL.

My supervisor Henry Caplan provided timely and unambiguous suggestions and criticisms that I benefitted from. Many hours of writing and rewriting were done after discussions with him. Encouraged by his enthusiasm, the compilation progressed (no matter how hard I fought it) to the final form you have now. If there are any points that the reader is impressed by then it was his wisdom that was merely transcribed to paper. The converse can not be said, errors and omissions are my sole responsibility.

Additionally I gratefully acknowledge the assistance of Greg Retzlaff whose constant attention and involvement from the onset was appreciated. Greg contributed Monte Carlo simulations of the magnetic system and later assisted in simulations on various converters for the determination of the charged pairs' energy losses as well as performing the bulk of the experimental set up along with Darryl Jessie. Henry and Greg played a major role in the end product you are now reading. They are responsible for the smoothing of rough edges in myself and my work.

Special mention to certain people for their insight and assistance is given with many thanks. Kevin Fissum, for his explanation of the "big picture" in the method of data analysis and his relaxed style in a rather hectic workplace. Emil Hallin, Johannes Vogt and Ru Igarashi provided expertise in all facets of the data analysis during crucial periods when I was not certain which course of action should be taken next or when an ear was needed to listen to another one of my crazy ideas. Additionally Emil, Johannes and Greg conducted tests on the SAL tagger using the final configuration of the pair spectrometer during February, 1994. Some results of this study are presented in Chapter 5. Rob Pywell provided the results of an integration routine he developed to calculate an effective field boundary for the pair spectrometer dipole using center line mappings of the dipole. Addi-

tionally I would like to acknowledge the people who introduced me to the world of charged particle optics. Jack Bergstrom gave illuminating lectures on beam optics and Les Dallin smoothly introduced the concepts of circular machine theory.

The technical support staff are second to none in their knowledge and ability. They are the workhorses in any scientific endeavour at this facility. Given an idea and/or sketch, they have the talent to create the finished product. What impressed me was their many successes on the first try.

A special thanks to Don Cruickshank for his informative discussions on electronics, cars, guitars, and perceptions of the universe.

The visiting scientists, faculty and students at this facility were always available for question and answer sessions. Their wit and human commentary always raised eyebrows.

The emotional and financial support of my family will always be remembered. The value and power of the nuclear family should never be underestimated.

The financial assistance provided by the Saskatchewan Accelerator Laboratory and the Natural Science and Engineering Research Council is greatly appreciated.

TABLE OF CONTENTS

LIST OF FIGURES

LIST OF TABLES

LIST OF ABBREVIATIONS

ADC	Analog-to-Digital Converter
AL	Algebraic Logic
CAMAC	Computer Automated Measurement and Control
CFD	Constant Fraction Discriminator
CLR	Clear
CW	Continuous Wave
ECS	Energy Compression System
EFB	Effective Field Boundary
FWHM	Full Width at Half Maximum
LC	LeCroy
LINAC	Linear Accelerator
NIM	Nuclear Instrumentation Module
NS	Nanosecond
Or	Ortec
PCB	Printed Circuit Board
PMT	Photo-multiplier Tube
PS	Pair Spectrometer
PSR	Pulse Stretcher Ring
RF	Radio Frequency
TDC	Time-to-Digital Converter
TTL	Transistor-Transistor Logic

Chapter 1. MOTIVATION

1.1 Introduction

The topic of this thesis is the design, construction and testing of a magnetic pair spectrometer (PS) for the detection of γ-rays between 20 and 160 MeV in energy. This instrument is intended for a test of the non-linearity in quantum electrodynamics (QED) through the measurement of the unverified phenomenon of photon splitting. Although this difficult experiment is not the topic of this thesis, it sets the design criteria for the PS. Photon splitting refers to the dissociation of a photon having energy ω_1, into a virtual electron-positron pair in the strong electric field of the nucleus which may then form two real photons, with energies ω_2 and ω_3. These photons are normally produced at small angles (5 -15 mr) with respect to the primary beam. If the incident photon energy is negligible compared to the rest energy of the nucleus then the recoil of the nucleus may be neglected and the nuclear field can be regarded as a static field giving $\omega_1 = \omega_2 + \omega_3$. Since ω_2 and ω_3 can have any values satisfying this constraint, the experiment requires a PS, with good energy resolution (< 5 MeV) and a large energy acceptance for the detection of the split photons.

There is a program at the Saskatchewan Accelerator Lab (SAL) to study nonlinear effects in QED and one planned experiment is the splitting of a photon into two which is the driving force behind this thesis. The other is Delbrück scattering where the incident photon is merely scattered by the nuclear Coulomb field. The Feynman diagrams for both are shown in Figure 1.1. These effects are not predicted by Maxwell's linear equations of electromagnetics. They are purely quantum mechanical effects. Fourth order perturbation theory is the lowest order that allows these effects. The possibility that transitions involve pairs in intermediate states is a direct consequence of vacuum polarization and gives rise to the nonlinear interaction.

Similar phenomena with closed electron loops in their Feynman diagrams are photon-photon coalescence, and photon-photon scattering and are also shown in Figure 1.1. The scattering of photons by photons is presently impossible to verify at SAL due to its small cross section and the experimental difficulties associated with having two photons with known energies arriving together. The coalescence process can be thought of in terms of

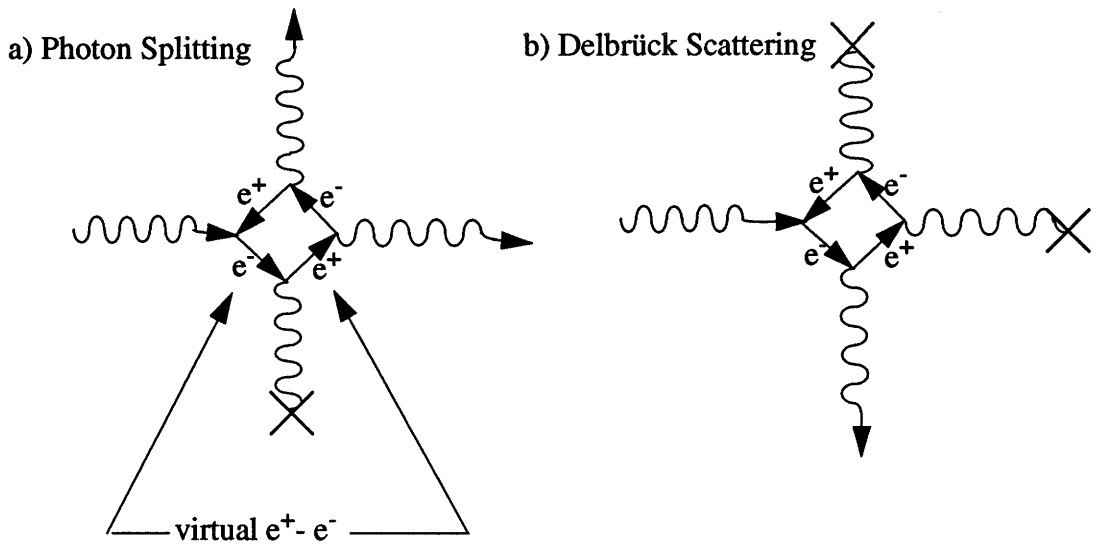

The photon lines ending in X are virtual photons interacting with the nucleus.

Each diagram has 3 permutations of the closed loop corners.

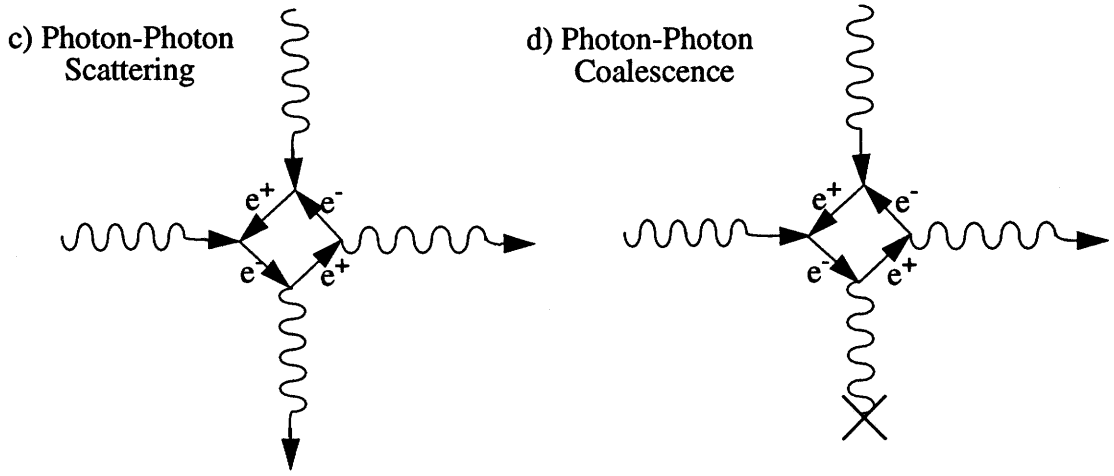

Figure 1.1. Selected Feynman diagrams for fourth order processes involving photons.

the inverse of photon splitting where two photons enter and one photon emerges with an energy equal to the sum of the incoming photons. It would be very difficult to observe for similar reasons.

Delbrück scattering is an elastic scattering process, however, it can not easily be distinguished from other types of elastic scattering since the reactions involved combine in a coherent manner. At low energy it is difficult to separate from electron resonance scattering where an incident photon of energy ω is absorbed by a bound atomic electron that is excited to a higher energy level and a photon of the same energy, ω is emitted upon the return of the electron to its initial state. There is also concern for coherent Rayleigh scattering which is the linear superposition of scattering for individual electrons in atoms or protons in the nucleus. The atoms do not excite or ionize. The situation is similar with nuclear Thomson scattering. Delbrück scattering is experimentally accessible at photon energies around 100 MeV and small angles (1-3 mr) with respect to the primary beam where the cross section dominates over competing processes [Jarlskog *et al.*, 1973].

Note that in Figure 1.1 photon splitting involves a single virtual photon exchanged with the nuclear field while Delbrück scattering has two virtual photons exchanged. Thus from QED it is predicted that Delbrück scattering has a cross section proportional to $Z^4\alpha^2$ (where α is the fine structure constant ~1/137), whereas the cross section for photon splitting is proportional to $Z^2\alpha$. For example, in identical Pb (Z=82) targets the cross section for Delbrück scattering is a factor of 50 larger than the cross section for photon splitting.

Total cross-sections for photon splitting were initially estimated at low or high energy limits relative to the rest mass of an electron ($m_ec^2 \sim E_\gamma$, or $E_\gamma >> m_ec^2$) and are described in the literature [Williams, 1935; Bolsterli, 1954; Bukhvostov, 1963]. Later, theoretical predictions of the differential cross section were obtained in the lowest orders of perturbation theory using the Born approximation for Coulomb field interactions [Boccaletti *et al.*, 1966; Shima, 1966].

While Shima's theoretical formulation was correct he did not integrate his differential cross sections. His main assumption was to regard the nucleus as a point charge with an infinite mass. Shima's work has been checked by others [Constantini *et al.* 1971, Johannessen, 1980]. Johannessen gave more complete results since he carried out the integrations omitted by Shima and applied them to a number of cases. Figure 1.2 shows

Johannessen's screened total cross section for a Uranium target which illustrates that it goes to zero as the incident photon energy goes to zero. Although results are available up to 1.5 GeV, we only reproduce here the region relevant to the present experiment. Figure 1.3 gives the Johannessen calculation of the differential cross section versus the angle for one exiting photon, θ_2 (relative to the incident beam direction). It is noticed that the cross section is very forward peaked which makes the experiment possible. We plan to detect the energies of the split photons at small angles with respect to the primary beam and compare it to the tagged photon energy.

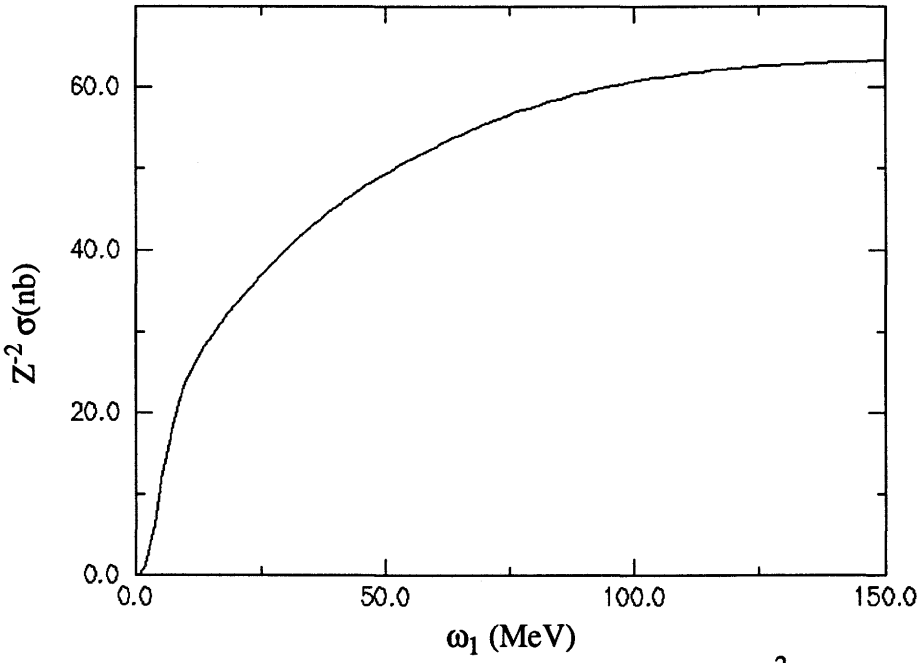

Figure 1.2. The total screened cross section divided by Z^2 for Uranium.

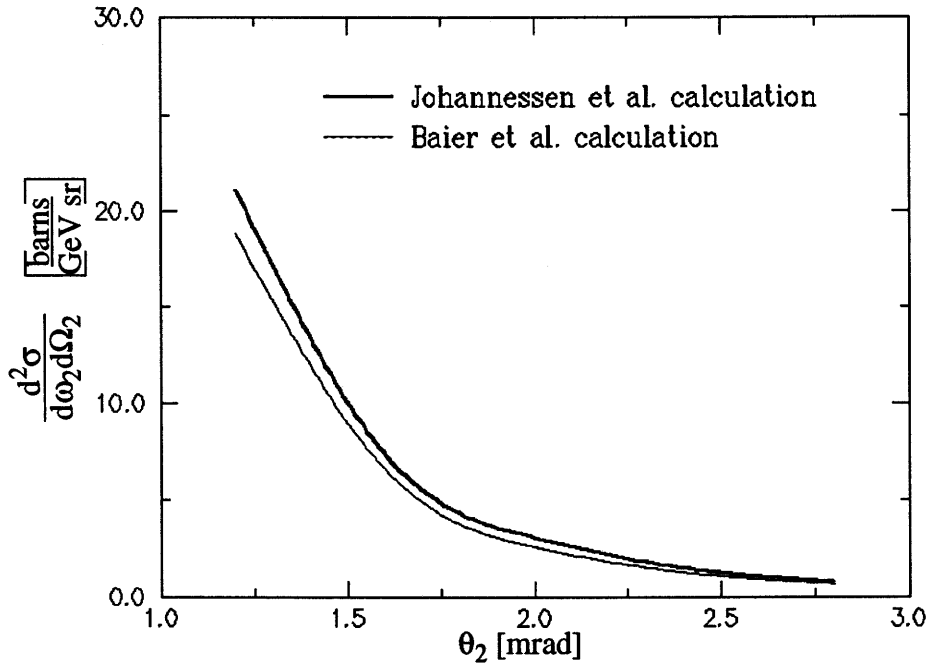

Figure 1.3. Differential cross sections for photon splitting on gold at 1.7 GeV for the ratio $\omega_2/\omega_1 = 0.87$.

There have been two previous attempts to detect photon splitting: one at low energy (~ 1 MeV); the other at very high energy (~ 5 GeV). In 1966 Adler and Cohen [Adler and Cohen, 1966] used 1.1 MeV γ–rays from a 2 Ci source of Zn^{65} and claimed the first observation of photon splitting. Figure 1.4 gives a schematic diagram of the setup used in the experiment. Splitting targets consisted of copper and cobalt (both were 0.35 cm thick). The solid angle that the target subtended at the source was 3.77×10^{-2} sr and that subtended by each of the two (3" × 3") NaI(Tl) scintillating crystal detectors at the target was 0.12 sr. Mercury shields were situated between the detectors in order to prevent radiation crosstalk. They obtained the sum of two simultaneous pulses in the detectors that were placed at backward angles with respect to the target and made an angle of ~105° with respect to the primary beam. True count rates for photon splitting were 1-2 every 10 hours and the corresponding measured experimental differential cross sections were of the order of 10^{-8} barns/sr which was six times larger than predicted by theoretical calculations given by Shima.

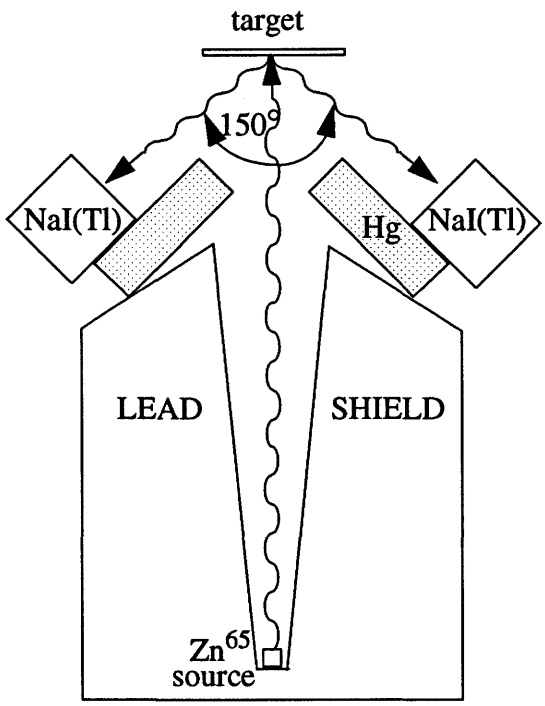

Figure 1.4. Experimental setup used by Adler and Cohen to detect photon splitting at backward angles.

Background contributions from double Rayleigh scattering were not accounted for in the experiment since accurate predictions were not available. Theoretical cross sections for nuclear Raman excitation [Maric and Mobius, 1959] or double Compton scattering from nuclear charge [Bolsterli, 1954] are not comparable to that of photon splitting [Adler and Cohen, 1966].

Another experiment was performed with much higher energy photons at Deutsches Elektronen-Synchrotron (DESY). This experiment was designed to detect Delbrück scattering. Figure 1.5 shows the experimental configuration. A well-collimated bremsstrahlung beam was obtained from the synchrotron target. The energy of the photons ranged from 1 to 7.3 GeV. The beam hit the Cu, Ag, Au, or U target, proceeded through a magnetic pair spectrometer and was absorbed in a quantameter. The scattered and or split photons were converted to e^-- e^+ pairs by an annular foil prior to the spectrometer and these pairs were bent in the magnetic field and detected by scintillators and wire chambers. This device allowed measurement of photon energy and coordinates of the conversion point in the angular range from 1 to 3 mr. A series of collimators and sweep

magnets were used to remove unwanted charged particles from the beam and decreased the amount of beam halo. In order to reduce spurious interactions, the photon beam was maintained in a vacuum.

The low energy part of the observed photon spectra was not explained fully by a combination of Delbrück scattering, Compton scattering, and secondary photons. They noticed a contribution from inelastically scattered photons which were believed to be the result of photon splitting. To test their hypothesis they plotted the number of these photons divided by Z^2 versus Z for four types of scattering targets. If the cross section is proportional to Z^2 then the result should be a horizontal line and this was observed. Table 1.1 reproduces the total cross section for the DESY experiment along with theoretical predictions by Bolsterli [Bolsterli, 1954] and Bukhvostov [Bukhvostov, 1963]. The determination of the cross section was difficult to extract due to the unknown initial photon energy and detection of only one split photon.

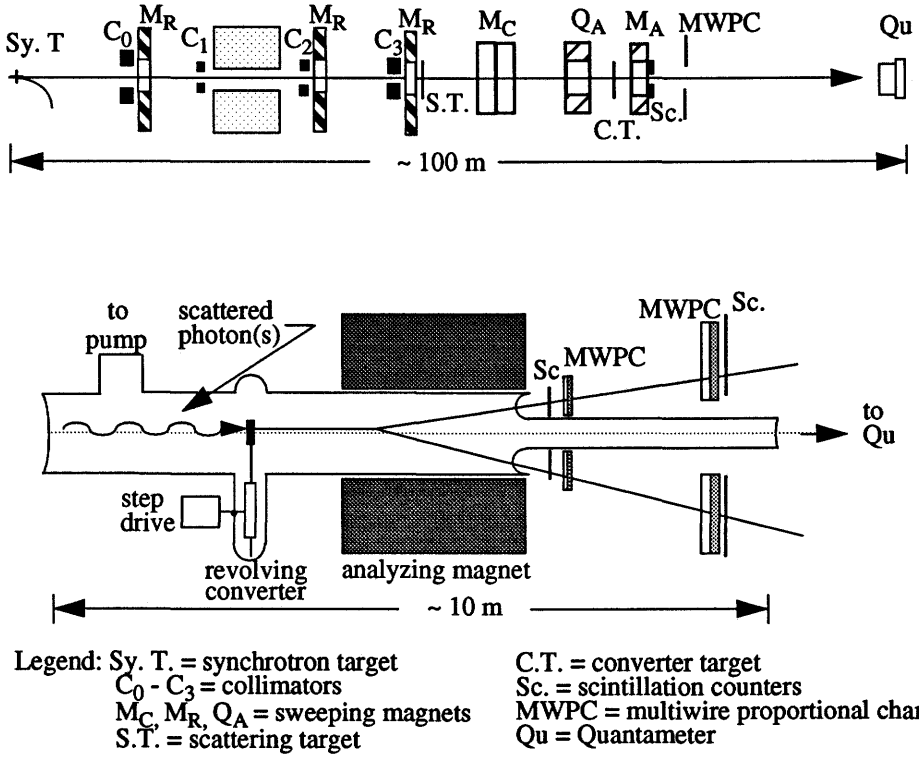

Figure 1.5. The experimental setup used by Jarlskog.

Table 1.1. Integrated total cross sections for photon splitting on gold for Jarlskog's experiment and theoretical predictions.

k (Gev)	σ_{exp} (mb)	σ (mb) [Bolsterli]	σ (mb) [Bukhvostov]
1.47-1.89	1.42 ± 0.05	0.78	4.8
3.00-3.84	0.80 ± 0.04	0.85	4.8
5.42-6.77	0.41 ± 0.03	0.91	4.8

Thus it is likely that photon splitting occurred but it was not well quantified. The need for further experimental observations is necessary. It is not clear whether background contributions were properly accounted for and the energy measurement of a single photon hinders conclusive results.

Background contributions are a serious problem in this type of experiment. One concern is pair production followed by hard photon bremsstrahlung of both electron and positron within the target, producing two photons whose energy sum is near the incident photon energy. This process has a cross section two orders of magnitude larger than that due to photon splitting [Baier *et al.*, 1974]. However, the angular spread of this process is wider than that for photon splitting due to multiple Coulomb (small angle, elastic) scattering of the charged pair in the target. A Monte Carlo simulation has been done [Retzlaff, 1991] for this process where 100 MeV photons were incident on a target. The energy sum of the two photons produced that was within 5 MeV of the endpoint energy was compared to the theoretical splitting rates from an identical target and it was found that the ratio of splitting events to pair production followed by hard bremsstrahlung satisfying the energy condition was seven to one. Thus this process will not wash out splitting events if the energy resolution is good enough (< 5 MeV) but will have to corrected for.

It must be ensured that the outgoing photons do not arise from other reactions such as double Compton scattering ($\gamma e \rightarrow \gamma\gamma e$), which is the lowest order approximation of photon-electron scattering where the final state consists of two photons and an electron. Due to small opening angles of the split photons, a well-collimated photon beam will have to be used with the split photons detected in the collimator's shadow in order to remove spurious secondary photons and at small angles relative to the primary beam.

1.2 The Spectrometer's Requirements

In this Section the requirements of a γ-ray spectrometer capable of detecting photon splitting will be given. SAL can produce electron beams with energies up to 300 MeV and in conjuction with the tagger can give tagged photons up to ~230 MeV. We propose to use tagged photons in the 50 - 70 MeV range to test the γ-ray spectrometer.

There are a few salient points worth mentioning again concerning photon splitting. The split photons are produced at small angles (θ ~ 5-15 mrad) with respect to the incident direction. The energy of the detected photons must add up to the incident tagged photon energy since recoil energy is negligible. The expected cross section is sufficiently high so the efficiency of the instrument is not a critical factor with our intended count rates. At photon energies around 130 MeV and a splitting target of 0.6 radiation lengths of Uranium, the total cross section should be near 200 μb for exit photon angles between 5 and 20 mrad [Milstein *et al.*, 1991]. We plan to measure photon splitting cross sections using a similar energy and geometry.

As seen from previous attempts, background processes which mimic the signature of photon splitting are a severe problem and must be minimized. The major background process (above 10 MeV) is pair production followed by hard photon bremsstrahlung of both e^- and e^+ in the target giving two photons whose energy sum is nearly equal to that of the incident photon. The required four way coincidence in the PS focal plane (five-way with the photon tagger) reduces background effects. We require a spectrometer with good energy resolution (< 5 MeV) capable of detecting split photons ~ 1 cm off beam axis after a distance of 1 m from the splitting target (10 mr from the primary beam axis) which will discriminate against most background processes.

A conceptual drawing for the photon splitting experiment is shown in Figure 1.6. The diagram shows a tagged photon incident on a target that produces two photons at small opening angles and reach the γ-ray spectrometer to be measured.

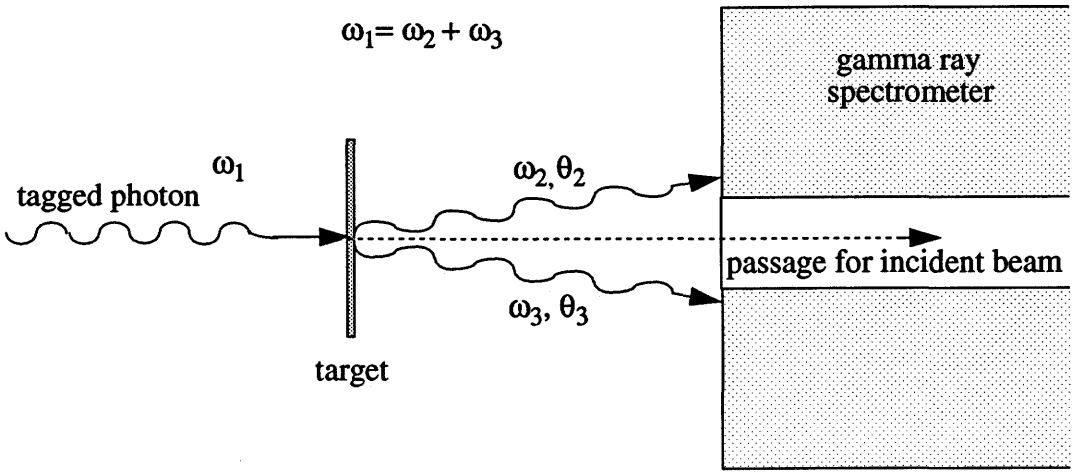

Figure 1.6. The conceptual drawing for the detection of photon splitting.

1.3 Choice of gamma ray spectrometer

Measuring the energy of a γ-ray is not as easy as for charged particles because the interaction of γ-rays with matter is quite different. For example charged particles continuously lose energy while traversing a medium through ionizing collisions and this may be detected directly. Gamma rays do not lose energy due to ionization until they are converted to charged particles. Thus γ-rays must produce charged particles by scattering or absorption before they can be detected. Therefore, a γ-ray spectrometer utilizes some process in which the γ-ray interacts and then infers the photon energy from the products of the reaction.

For the energy regime (20 - 160 MeV) under consideration the γ-rays predominantly interact with matter through the process of pair production while the Compton effect is a much smaller effect. For an extended medium the electrons and positrons produced will suffer bremsstrahlung loss and generate secondary photons. These in turn can pair produce or Compton scatter (depending on their energy) producing more charged particles that can re-radiate, giving rise to an electromagnetic shower process. A possible shower or cascade is depicted in Figure 1.7. As mentioned, in addition to bremsstrahlung there is a constant ionization energy loss of electrons/positrons due to collisions in the

medium. Ultimately, if the medium is large enough, all the energy from the initial γ-ray appears as ionization energy loss even though only the charged particles cause this directly.

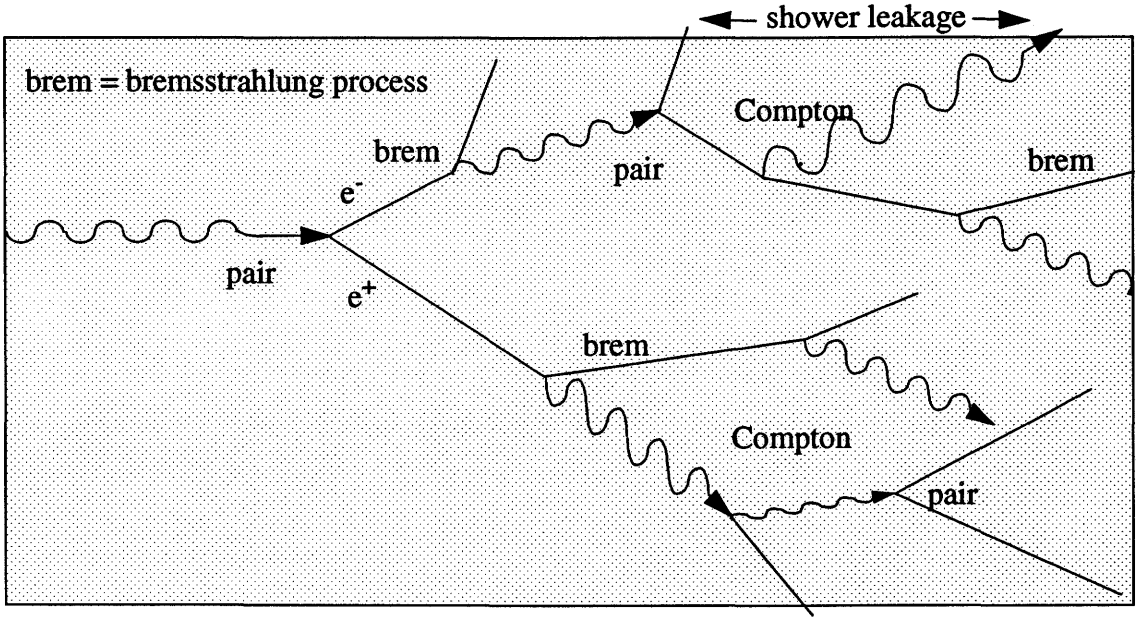

Figure 1.7. A typical electromagnetic shower process in a medium.

During the passage of electromagnetically interacting particles through an isotropic medium, most of the dependence on the medium is contained in the radiation length [Particle Properties Data Booklet, 1990]. One radiation length, L_R (cm) is defined for a high energy electron beam as that thickness of material for which the beam energy is reduced by a factor of 1/e due to bremsstrahlung. For a homogenous element of atomic number Z (> 5) and atomic mass A, one can express the inverse of a radiation length as in Equation 1.1. For example, in Al, Cu, Pb, Au,and U the unit radiation lengths are (8.89, 1.43, 0.56, 0.34, 0.32) cm, respectively.

$$1/L_R = \frac{4\alpha r_e N_A Z^2}{A}\left(ln\left[184.15/Z^{\frac{1}{3}} \right] + \frac{1}{Z} ln\left(\frac{1194}{Z^{2/3}} \right) - 1.202\alpha^2 Z^2 \right.$$

$$\left. 1.0369\alpha^2 Z^4 - 1.008\alpha^6 \frac{Z^6}{(1+\alpha^2 Z^2)} \right) \qquad (1.1)$$

Gamma ray spectrometers generally fall into one of two categories: total absorption spectrometers (sometimes called calorimeters) that absorb the total energy of the shower process; and spectrometers which detect the charged particle(s) from the first interaction of the photon. The total absorption spectrometer by its very nature has almost 100% efficiency. The latter are either pair spectrometers where the electron and positron are detected after pair production or Compton spectrometers where the single recoil electron is detected along with its exiting angle. The second class of spectrometers use thin converters to minimize the energy loss within it and a magnetic field for momentum analysis. However, these types of spectrometers are plagued by low efficiency predominantly due to small converter thickness and solid angle of acceptance.

The total absorption spectrometer can be a large instrument since it contains the whole shower produced. These devices are highly efficient, have a large angular acceptance and can possess good energy resolution (typically 2-5% FWHM). An example is an inorganic sodium iodide crystal doped with thallium, NaI(Tl). This crystal produces a pulse of light in a short time interval (< 10 ns) after the passage of a charged particle. The excitation generated by the ionizing particles in the shower propagate through the crystal lattice and impurity centers capture them. The recombination process gives rise to an excited center that emits light when it returns to ground state. The sum of this light energy is proportional to the ionization energy loss in the crystal and is detected by an array of photo-multiplier tubes surrounding the device allowing determination of the ionization energy loss. With proper design this energy loss is proportional to the incident γ–ray energy.

An example is the BUNI (Boston University NaI(Tl)) spectrometer (used in SAL experiments). It has an optimum energy resolution of 1.3% and 1.7% FWHM for 130 MeV photons and 330 MeV electrons, respectively [Miller, 1988]. BUNI consists of a cylindrical core and 4 annular pieces forming a cylinder 53.3 cm in diameter and 55.8 cm in length. It is an impressive structure due to its large size of crystals. It is large since electromagnetic showers can spread up to 10 radiation lengths in diameter and for NaI this gives a typical shower diameter of 20 cm. To completely contain a shower the crystal must be infinite in extent. This is impractical so one must be content to use finite sizes and contend with shower leakage (refer back to Figure 1.7). It is believed that this leakage is mainly responsible for most of the loss in energy resolution of the spectrometer.

However, the BUNI spectrometer if used for the present experiment, would have to allow passage of the primary beam. This could conceivably be accomplished by cutting a hole through the crystal (as well as cutting it in half) and inserting a beam pipe. The cost of such a spectrometer with a hole through it would be approximately $500,000. This method would enable energy determination of the split photons but the resulting showers may migrate across the primary beam pipe, pass through and end up in the other half of the crystal giving ambiguous results due to the internal crosstalk. With these modifications the crystal would be overtaxed as even a well collimated photon beam seems to have a halo around it. Considerations such as these dismiss the possibility of using such a device for our purposes.

The second type of gamma ray spectrometer converts photons to charged particles in a thin foil and momentum analyses them in a bending magnet. A device such as this is called a magnetic γ-ray spectrometer which can be a pair or Compton spectrometer. In a collimated, monoenergetic beam of photons, the number of photons that remain after travelling through a medium of thickness dx is given by Equation (1.2). The total cross section per atom is denoted by σ and above 10 MeV is the sum of the partial cross sections for Compton scattering and pair production. The number of nuclei per cm^3 is denoted by n, μ is the linear attenuation coefficient (cm^{-1}), ρ is the density and N_A is Avogadro's number.

$$I(x) = I_o e^{-\sigma_{total} nx} \tag{1.2}$$

$$where\ \sigma_{total} = \frac{\mu A}{\rho N_A} \cong (\sigma_c + \sigma_p)$$

The intensity of the photon beam will decrease in an exponential manner traversing the medium. It is one of these two processes that allow energy determination of the initial photon(s). For the present experimental purpose a concept diagram of the two magnetic spectrometers and their implementation is given in Figure 1.8.

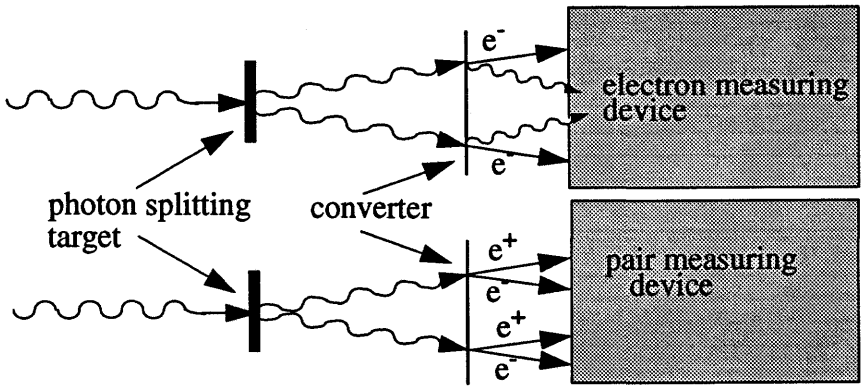

Figure 1.8. Conceptual views of a Compton and pair spectrometer for use in photon splitting.

There are normally two categories of magnets in magnetic γ-ray spectrometers. These are the dipole and solenoidal type magnets. The dipole type has the magnetic field normal to the particle motion with particles moving in almost planar orbits while the solenoidal type magnet has a field that is nearly parallel to the direction of motion and the charged particles move in a spiral orbit. The purpose of a magnet is twofold: to change the direction of motion in order for the projectile to reach some target or detector; and to separate particles of different momenta from each other.

Solenoidal spectrometers are useful for high transmission rates from a small source area. In a solenoidal lens the field is often homogeneous and parallel to the axis containing the source and detector. After World War II laboratories started using solenoidal spectrometers regularly. The uniform field inside the solenoid made the trajectory easy to calculate and their use began to grow. These magnetic lenses found applications in beta spectroscopy where the acceptance of particles from the source was controlled by inserting slits. Defining slits and baffles were also used to shield detectors from incident radiation.

Minor consideration was given to this type of magnet since at our proposed energies an extremely strong magnetic field would be required to keep the bend radius tight to conserve space and prevent the cost from rising dramatically. This type of magnet is most suitable to lower energies ($E_\gamma < 20$ MeV). The interested reader is referred to the literature for solenoidal type spectrometers [Siegbahn, 1966].

Dipole magnets are good for analyzing forwardly produced particles since their solid angle acceptance is relatively small. Often constant field dipoles are used in magnetic Compton or pair spectrometers owing to their simplicity.

Compton spectrometers are based on the Compton effect and to a first approximation the scattered electron was originally free and at rest. In most cases the design stipulates forward recoiling electrons since the cross section is highest in the forward direction. It is necessary to measure two secondary quantities in order to reconstruct the photon energy. The kinetic energy of the recoiling electron and either the direction of the electron or the scattered photon are two such quantities.

A disadvantage with such devices is that they are usable only when dealing with energy ranges where the Compton effect predominates and it is sufficient to detect a single electron. In lead (Z = 82) the cross section for pair production overtakes that of Compton scattering at ~ 5 MeV, thus we will be dealing almost exclusively with pair production at our proposed energies.

Pair production in the field of a nucleus begins at photon energies above threshold (1.022 MeV) and rises quickly while the cross section for the other two processes falls off rapidly with increasing energy. Pair production can also take place in the field of atomic electrons with the recoiling electron gaining a large amount of kinetic energy. In this case there are three charged particles produced (having total energy near that of the incident photon) which will have to be discriminated against. For pairs produced from the field of the nucleus, the cross section is proportional to Z^2 of the absorber. One can consider pair production the inverse of bremsstrahlung since their Feynman diagrams are the same except for the directions of the incoming and outgoing particles. This explains why they are treated similarly in theory [Fernow, 1986]. The relative production rates for pair

production is about 7/9 of that corresponding to bremsstrahlung in the high energy limit (for $\omega_1 >> 137 m_e Z^{-1/3}$). Equation 1.3 gives the pair production cross section for this case where r_e is the electron radius.

$$\sigma_{pair} = 4\alpha Z^2 r_e^2 \left[\frac{7}{9} \ln\left(\left(183 Z^{-\frac{1}{3}} \right) - \frac{1}{54} \right) \right] \tag{1.3}$$

In a pair spectrometer the γ-ray is converted to an electron - positron pair which is momentum analyzed by the magnetic spectrometer and often recorded by scintillation detectors or wire chambers. The only measurements required are energies of the two charged particles. The coincidence required greatly reduces the amount of background in the focal planes of the PS, and the energy over which the spectrometer can be utilized is broader than the corresponding Compton spectrometer due to the energy ranges of the two processes.

It will become clear in Chapter 2 that our most suitable choice is a dipole magnet. Since an in-house dipole magnet was available, the major concern was for a set of detectors properly positioned and a judicious choice of shapes and thicknesses of converter foils. Minor adjustments will have to be made to the experimental setup to detect photon splitting and Delbrück scattering.

Chapter 2 discusses design considerations involved with the assembly and testing of a magnetic γ-ray spectrometer. Chapter 3 details the SAL facility with the tagger unit and the experimental setup used for the test of the PS. The raw or on-line data is presented here along with a summary of the various test runs. The method of off-line data filtering is presented in Chapter 4 with critical analysis. Conclusions and recommendations are given in the final Chapter. References and appendices follow the main body of the thesis. While the test configuration and operation of the spectrometer is stated in the first four chapters it is only in the last Chapter that the final design is presented incorporating a vacuum system and 32 detectors as well as other new developments.

Chapter 2. DESIGN CONSIDERATIONS

2.1 Preliminaries

Ideally it would be reported that a careful analysis of pair spectrometers was carried out and the most suitable design for the present experiment was decided upon. Reality dictated that this would not be done. Initial estimates of the cost for an ideal magnet were about $200,000 including power supply and it would take approximately two years for design, construction and implementation. Thus the path chosen was heavily influenced by economic and time constraints. The design was based on an existing magnet and the process was to verify that this magnet was adequate as opposed to ideal for the photon splitting experiment. Therefore, rather than achieving maximum performance from the best design, the work was to determine what would be lost by using the existing magnet and to decide if this was acceptable.

In this Section a brief look at the history of magnetic spectrometers is presented while in 2.2 enough of the theory of magnetic spectrometers is given in order to understand their specifications. The objective is to give a clear discussion of magnetic systems and how their use has evolved starting from first principles. Section 2.3 deals with the key design parameters and illustrates them by describing state of the art pair spectrometers. The final section deals with design considerations for the SAL pair spectrometer.

Magnetic spectrographs came into subatomic physics in the early 1900's in step with the revolutionary views of the atom. They were used as a means to determine the momentum of charged particles. As early as 1899 Becquerel used a magnetic spectrograph that bent particles by 180^{o} to verify that the particles of beta radiation were indeed the same as the electrons in Thomson's cathode ray tube. During the Rutherford period many magnetic spectrographs were used in the study of natural alpha decay and beta decay spectra. Today other detectors are used in conjunction with magnetic analysis, such as proportional gas counters, semiconductor counters and scintillation counters. In these devices the pulse height is proportional to the energy deposited by the charged particle in the detector but magnetic analysis affords the most accurate means of measuring beta and alpha-ray spectra. However, it was the measurement of atomic masses that stimulated the development of high precision magnetic spectrometers.

In a uniform magnetic field of induction B [T], the path of a charged particle, having charge q (|q|=1 for electrons) and momentum **p**, having magnitude p [MeV/c], is bent into an arc of a circle of radius ρ [m] according to Equation (2.1).

$$p = 299.8B\rho q \tag{2.1}$$

A good rule of thumb is that a magnetic induction of 1 Tesla will give a 300 MeV electron a radius of curvature of 1 meter.

Early designs of uniform field dipole magnets used in alpha and beta spectroscopy incorporated the semicircular focussing principle where analyzed particles were bent by 180° giving an easy method of determining the orbit diameter. Figure 2.1 illustrates this concept. Provided the magnetic field was known, an absolute determination of the electron's momentum could be made using Equation (2.1) without initially calibrating the instrument.

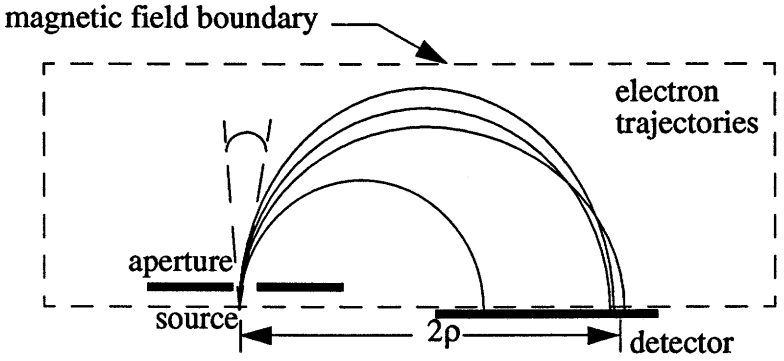

Figure 2.1. The semicircular focusing principle.

The advantages of the 180° spectrograph were that it had a broad energy range of operation especially when different magnetic field settings were used. However, the instrument also had disadvantages. For example, the range for simultaneous measurement of energies (at a fixed field setting) was about 10% and only measurements made at a single angle with respect to the primary beam were easily attainable. There was also the problem of being somewhat limited in the type of experiments able to be performed since the source and detectors are both situated in the uniform field. These limitations stimulated further research into new designs of magnetic spectrometers.

By the 1950's there were increasing demands for improved specifications due to the greater maturity of nuclear physics and magnetic spectrographs changed accordingly. With the rise of computers in the 1960's further precision was achieved in these instruments and compound (more than one magnet) spectrometers with complicated fields could be built after extensive computer simulations had been done.

2.2 Theoretical Aspects

A major consideration when designing a magnetic spectrograph is an unambiguous spatial separation of particles with differing momenta. The ability of the instrument to distinguish between particles of similar but differing momenta is termed the momentum resolution. Additionally, the spectrograph should be able to span a wide range of momenta thus saving time by using only a single magnetic field setting to cover the necessary energy range. The instrument should accept particles with a large solid angle from the source making for efficient operation. The optimization process involves minimizing aberrations in focussing while maximizing the solid angle of the device and its resolution.

It is useful to begin with a discussion of a relatively simple device that allows calculation of its characteristics using only analytic geometry. One of the earlier dipole magnets used for momentum analysis was the Browne-Buechner magnetic spectrograph [Browne and Buechner, 1956]. This instrument focussed particles in a radial plane normal to the magnetic field (i.e. the bend or dispersive plane) and is termed single focussing. Figure 2.2 shows a schematic drawing for the spectrograph. This sector type dipole had curved entrance and exit faces. Notice that the poles for the dipole are in areas where the field is needed. Its simple elegance made it appealing for many experiments.

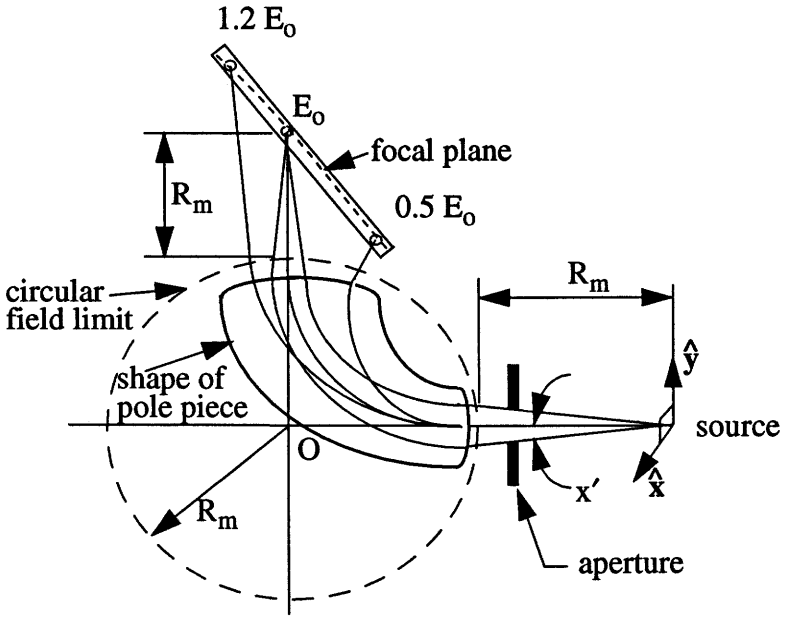

Figure 2.2. The Browne-Buechner spectrograph (not to scale).

The geometry used for the Browne-Buchner spectrograph is straightforward. A uniform magnetic field was produced and the limit of its boundary is represented by the dashed circle having radius R_m. The source of charged particles was placed at a distance $2R_m$ from the center of the circular field boundary. Particles were focussed towards a hyperbolic focal plane and detected. Particle energies varying by a factor of 2.5 could be simultaneously recorded.

In this configuration reference rays normal to the field upon entrance will be normal upon exit. Further, deflected particles, independent of momentum, appear to originate from the center of the field. The situation is understandable in terms of conservation of angular momentum in the magnetic field (**L** =0).

The focussing properties are best described in Figure 2.3. The bend angle, α, may be found (Appendix B.1 contains the derivation along with other useful equations used in beam optics) as a function of bend radius, ρ, and is shown in Equation (2.2).

$$\cos\alpha = \frac{\rho^2 - R_m^2}{\rho^2 + R_m^2}, \tan\frac{\alpha}{2} = \frac{R_m}{\rho} \qquad (2.2)$$

Focussing in magnetic spectrometers can be calculated by two ways. One may use analytical equations from beam optics or graphically construct the focal plane. Analytically the object distance, L_{ox} (in units of bending radius), measured to the effective field edge is equal to $S_o/\rho = R_m/\rho = \tan\xi$ and similarly the image distance, L_{ix}, is $S_{ix}/\rho = \tan\psi$ (refer to appendix B.1). The expression relating the image distance to the object distance and the bend angle [Livingood, 1969] is used in Equation (2.3) and appropriate substitutions lead to (2.4).

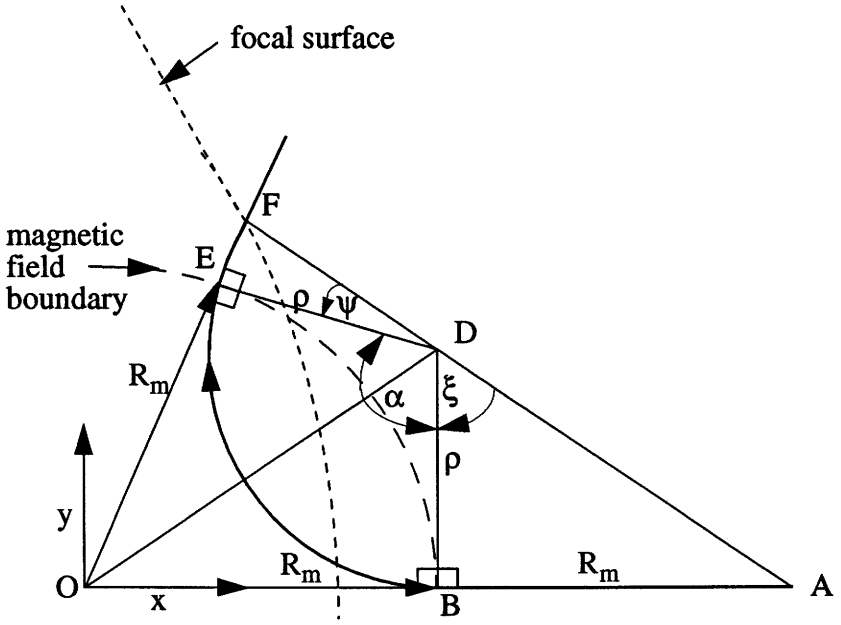

Figure 2.3. Construction of the focal plane by Barber's rule.

$$L_{ix} = \frac{L_o \cos\alpha + \sin\alpha}{L_o \sin\alpha - \cos\alpha} \,. \tag{2.3}$$

$$\tan\psi = -\frac{\tan\xi + \tan\alpha}{1 - \tan\xi\tan\alpha} \tag{2.4}$$

Consider a particle having a momentum of magnitude p and bend radius ρ denoted by ABEF as shown in Figure 2.3. Barber's rule [Barber, 1933] states that for a uniform field the source (A), center of curvature (D) and image (F) all lie on the same straight line. To show that $\overline{ADF}$ is a straight line it is sufficient to show that angles ADB, ODB, ODE and EDF add to 180°. If Barber's rule is valid then $\alpha + \psi + \xi = 180^o$ and $\psi = 180^o - (\alpha + \xi)$.

Taking the tangent of ψ yields Equation (2.5) and a trigonometric identity gives Equation (2.6) which is identical to (2.4). Therefore one can conclude that the object, center of curvature and image are colinear which verifies Barber's rule.

$$\tan\psi = -\tan(\alpha + \xi) \tag{2.5}$$

$$\tan\psi = -\frac{\tan\xi + \tan\alpha}{1 - \tan\xi\tan\alpha} \tag{2.6}$$

The focal point is located at F for particles (of a specific momentum) diverging at A. It is a simple task to extract the locus of focal points (the curved dotted line passing through F) for particles of differing momenta by describing F in terms of Cartesian coordinates whose origin is at C. For example, if a particle starts at A and is focussed then equations (2.7) and (2.8) give the x, y coordinates for the point F.

$$x = \overline{OF}\cos AOF \tag{2.7}$$

$$y = \overline{OF}\sin AOF \tag{2.8}$$

The sine law is used to obtain equations (2.9) and (2.10). The Equation of a hyperbola is obtained for the focal plane from these two equations when ρ is eliminated. The focal surface is normally approximated by a straight line since the focal plane will be finite and outside the field boundary in a practical configuration.

$$x = 2R_m\left(\frac{R_m^2 - \rho^2}{3R_m^2 - \rho^2}\right) \tag{2.9}$$

$$y = 4\rho\left(\frac{R_m^2}{3R_m^2 - \rho^2}\right) \tag{2.10}$$

The dispersion is another useful quantity that can be determined. For example, the angular dispersion can be found by differentiating (2.2) with respect to ρ and the result is shown in (2.11). The significance of the minus sign is that the bend angle increases while the bending radius decreases.

$$\frac{\partial\alpha}{\partial\rho} = \frac{\partial\alpha}{\partial\cos\alpha}\cdot\frac{\partial\cos\alpha}{\partial\rho} = \frac{-4\rho R_m^2}{\sin\alpha\left(\rho^2 + R_m^2\right)^2} \tag{2.11}$$

Equation (2.12) gives the relationship between the bend radius and the distance along the focal plane, κ. This distance is measured from the origin and is the square root of the sum of the squares of the x,y coordinates. There are various representations for dispersion but it is common to relate how far the image moves along the focal plane for a ±1% change in kinetic energy (or momentum). To determine the change in distance along the focal plane for a given change in momentum one can relate the bend radius to the momentum of the electron by differentiating (2.1) for a constant magnetic field strength and multiply by the inverse of (2.12) to obtain (2.13). To obtain the standard units of mm/%, Equation (2.13) is normalized by the momentum then multiplied by 100. Other parameters can be calculated from a consideration of Figure 2.3 (for example, the magnification of the image) but will not be presented here.

$$\frac{\partial \kappa}{\partial \rho} = \sqrt{\left(\frac{\partial x}{\partial \rho}\right)^2 + \left(\frac{\partial y}{\partial \rho}\right)^2} = \frac{4R^2{}_m\left(9R^4{}_m + 10R_m^2\rho^2 + \rho^4\right)^{1/2}}{\left(3R_m^2 - \rho^2\right)^2} \tag{2.12}$$

$$\frac{\partial p}{\partial \kappa} = \frac{\partial p}{\partial \rho}\cdot\frac{\partial \rho}{\partial \kappa} = \frac{p}{\rho}\cdot\frac{\left(3R_m^2 - \rho^2\right)^2}{4R^2{}_m\left(9R^4{}_m + 10R_m^2\rho^2 + \rho^4\right)^{1/2}} \tag{2.13}$$

2.2.1 Mathematics of magnetic systems

There are a few points that need careful explanation when describing a magnetic system. The concept of a central trajectory (CT) is valuable when analyzing magnetic systems. A CT is defined relative to the origin, O, of a coordinate system as the path through a magnetic system that an ideal beam (monoenergetic particles with parallel trajectories) would follow. Symmetry considerations normally dictate the CT passing along the centerline of the magnetic system in the same manner as an axial ray in an optical system. The means of describing a real beam of particles is presented with reference to Figure 2.4.

Path length, S is measured along the CT from the entrance to the exit of the magnetic element. In Figure 2.4.a two particles are considered travelling through the midplane of a uniform static magnetic field with momentum p_0 (the CT) and $p_0 + \Delta p$ (the arbitrary ray) having bending radii ρ_0 and $\rho_0 + \Delta\rho$, respectively. In Figure 2.4.b the effect of radial displacements is seen and in Figure 2.4.c particles with zero offset but having radial slope $\pm x_0' = dx_0/dS$ (proportional to the angle, θ_0,these rays make with the CT) are shown.

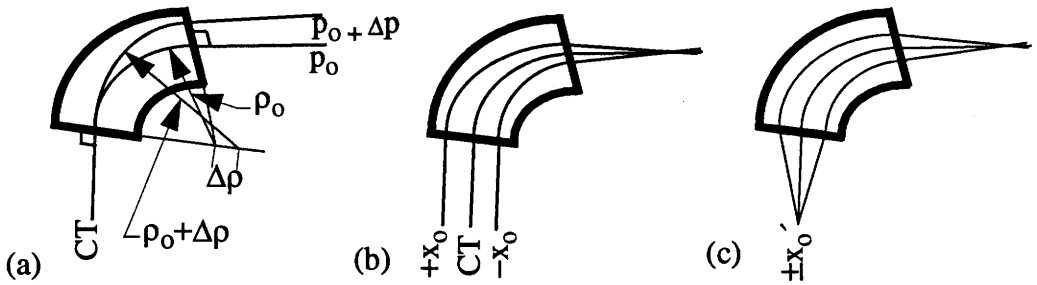

Figure 2.4. (a) First order momentum dispersion, (b) parallel to point, and (c) point to point focussing.

An arbitrary particle has initial designation given by the vector $\mathbf{X_0}$ in Equation (2.14) where x is the radial displacement of this ray with respect to the CT, θ (= x′, paraxial approximation) is the angle the ray makes in the radial plane with respect to the CT, δ (= $\Delta p/p_o$) is the fractional momentum deviation of the ray from the central trajectory and is a constant in a static magnetic field. Additionally the output vector is $\mathbf{X_f} = \mathbf{R}\,\mathbf{X_0}$ where **R** is the transfer matrix connecting the exit parameters to the initial ones.

$$\vec{X}_0 = \begin{bmatrix} x_0 \\ x_0' \\ \delta \end{bmatrix} \tag{2.14}$$

Using such coordinates which measure the deviation through the magnet from the CT, one can make a linear approximation to the final coordinates. Of course the matrix elements have to be calculated, once and for all for each type of magnetic element by geometry or integration of the equations of motion. In a beam of particles where deviations are small (i.e. $x/\rho << 1$, $x' << 1$, $\delta << 1$, etc.), a first order description of particles will often suffice.

In first order optics the uncoupled transfer matrices from source A to detection point B are given (refer to Figure 2.5) for the dispersive and nondispersive planes in equations (2.15) and (2.16), respectively. Notice that both equations contain matrices that allow for a drift space (M_d) before and after the magnet (M). It is apparent that $x_1 = R_{11}x_0 + R_{12}x_0' + R_{13}\delta$. To facilitate remembering the matrix elements, the notation $R_{11} = (x_1|x_0)$

clearly shows the dependence of x_1 on x_0. The beauty of the matrix formalism is that the effect of several elements in succession in a magnetic system can be obtained by matrix multiplication (proceeding from right to left).

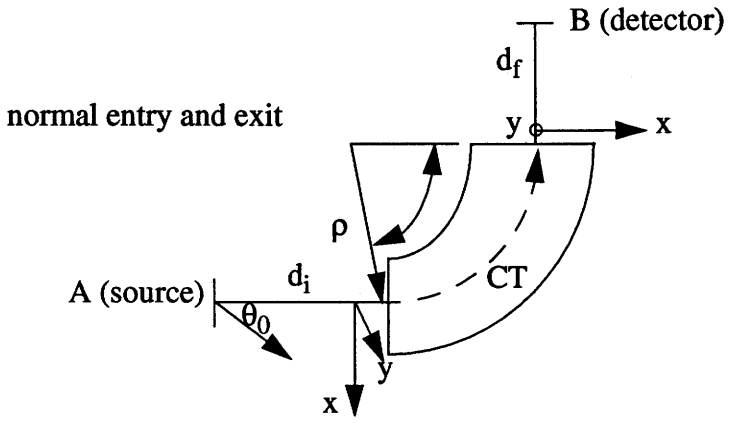

Figure 2.5. The first order transfer matrix for a spectrometer.

$$\begin{bmatrix} x \\ x' \\ \delta \end{bmatrix} = \begin{bmatrix} R^x_{11} & R^x_{12} & R^x_{13} \\ R^x_{21} & R^x_{22} & R^x_{23} \\ 0 & 0 & 1 \end{bmatrix} \begin{bmatrix} x_0 \\ x_0' \\ \delta_0 \end{bmatrix}, \; where \; R^x = M^x{}_{d_f} M^x M^x{}_{d_i} \tag{2.15}$$

$$\begin{bmatrix} y \\ y' \end{bmatrix} = \begin{bmatrix} R^y_{11} & R^y_{12} \\ R^y_{21} & R^y_{22} \end{bmatrix} \begin{bmatrix} y_0 \\ y_0' \end{bmatrix}, \; where \; R^y = M^y{}_{d_f} M^y M^y{}_{d_i} \tag{2.16}$$

For a focus in the x-direction that has x independent of the original direction, x_0', requires $R_{12} = 0$ and this is termed point to point focussing. If the corresponding matrix element for the z-plane is also zero (i.e. $R_{z,12} = 0$) then there is point to point focussing in this direction and the term used is double focussing. In a completely analogous manner if $R_{x,11} = 0$ then there is parallel to point focussing where the focus is independent of radial displacement.

The explicit transfer matrices for a drift space and uniform field dipole are shown in equations (2.17) and (2.18) for the x (bend) and y (non-bend) planes. These matrices would simply be inserted into equations (2.15) and (2.16) to describe the particles leaving the system.

$$M^{y}{}_{d}= \begin{bmatrix} 1 & L \\ 0 & 1 \end{bmatrix}, \quad M^{y}= \begin{bmatrix} 1 & \rho\alpha \\ 0 & 1 \end{bmatrix} \tag{2.17}$$

$$M^{x}{}_{d}= \begin{bmatrix} 1 & d \\ 0 & 1 \end{bmatrix}, M^{x}= \begin{bmatrix} \cos\alpha & \rho\sin\alpha & \rho(1-\cos\alpha) \\ -\frac{\sin\alpha}{\rho} & \cos\alpha & \sin\alpha \\ 0 & 0 & 1 \end{bmatrix} \tag{2.18}$$

So far, we have only considered entry and exit from our wedge magnets normal to the pole face. For non-normal entry and exit, the faces of a bending magnet behave like thin lenses in both the x and y planes. Figure 2.6 shows the geometry and the additional transfer matrices. Again these matrices would be inserted just before and after the dipole matrix to account for this effect.

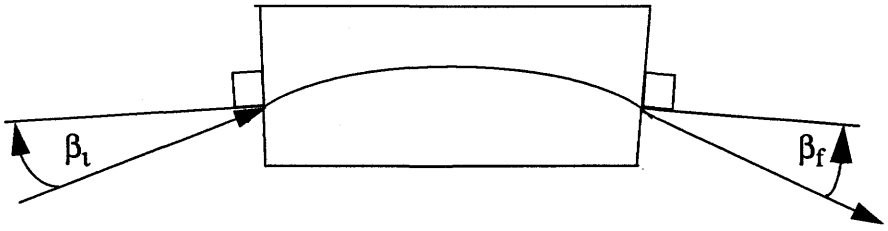

$$f^{x,y}= \mp R/\tan\beta$$

$$R^{x} = \begin{bmatrix} 1 & 0 & 0 \\ -\frac{1}{f_x} & 1 & 0 \\ 0 & 0 & 1 \end{bmatrix}, \qquad R^{y} = \begin{bmatrix} 1 & 0 \\ \frac{-1}{f_y} & 0 \end{bmatrix}$$

Figure 2.6. The transfer matrices for non-normal entry and exit for a magnetic system.

A nonnormal entry angle causes a focussing in one direction (the y-plane) and defocussing in the other, similar to a quadrupole field. This is called edge focussing and is a consequence of fringing fields. The breakdown of the uniform field is obvious in Figure 2.7. It has been shown that for uniform field spectrometers the focussing action of the fringing field can be used to obtain focussing in the y-plane and slightly improve radial focussing [M.S. Mladjenovic, 1979]. The action of fringing fields is a second order effect.

In first order optics an approximation is made where the uniform field strength of the dipole abruptly changes from full value to zero. This is termed the effective field boundary and is examined in Appendix A.2.

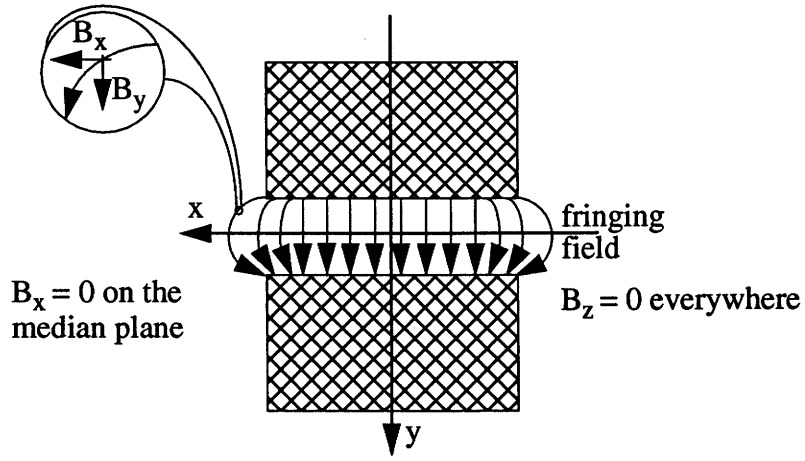

Figure 2.7. Edge focussing in a dipole.

The preceding discussion applied to the transformation of a single but arbitrary trajectory traversing a static magnetic system. The natural next step is to consider a number of rays or bundles. The physical size of these bundles is called a beam envelope. Focussing of such a real beam is not to a point (since not all trajectories are parallel) but to what is termed a waist.

Consider the particle at point C in Figure 2.8. The set of linear equations can be expressed in matrix form as shown in Equation (2.19) or the compact notation of Equation (2.20) and is equivalent to that used in magnetic ray tracing codes such as *Transport* (Brown *et al.*, 1966). Note that a number of elements go to zero as a result of motion in the magnetic midplane of a uniform, static magnetic field. The matrix element $R_{66} = 1$ since the total energy of the particle remains unchanged. It is the above simplification that justifies the uncoupling of the transfer matrix into a 3×3 matrix for the dispersive plane and a 2×2 matrix for the nondispersive plane.

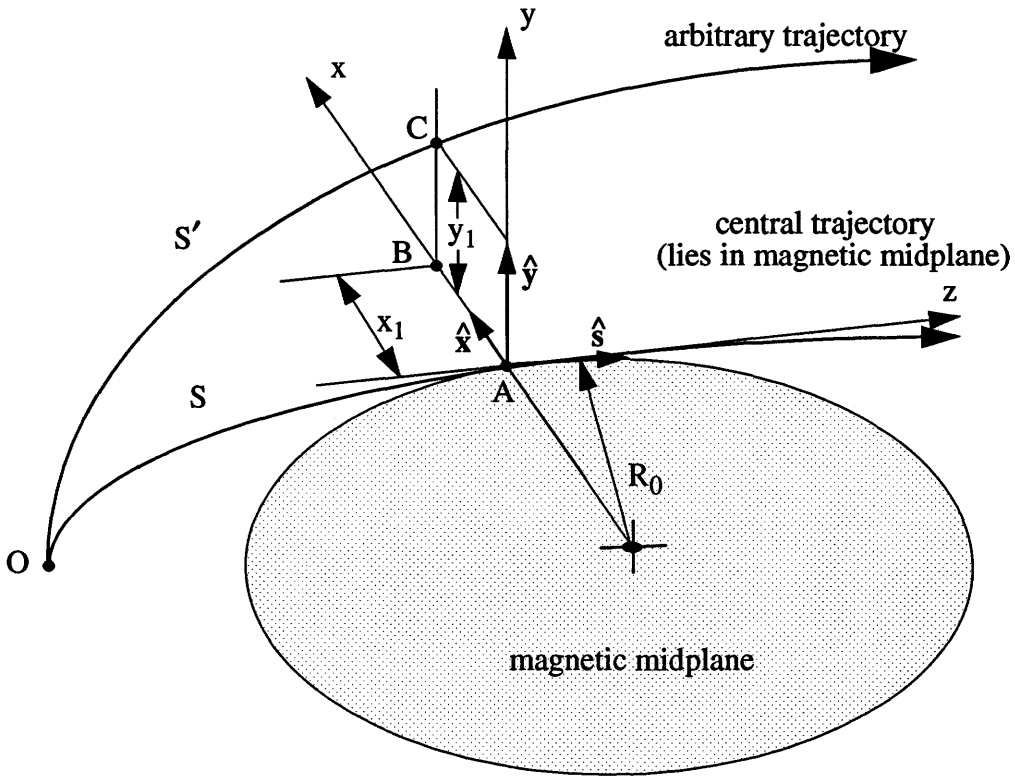

S' = path length O - C

S = path length O - A

$l = S - S'$

Figure 2.8. The curvilinear coordinate system used in studying trajectories through magnetic volumes.

$$\begin{bmatrix} x \\ x' \\ y \\ y' \\ l \\ \delta \end{bmatrix} = \begin{bmatrix} (x|x_o) & (x|x_o') & 0 & 0 & 0 & (x|\delta_o) \\ (x'|x_o) & (x'|x_o') & 0 & 0 & 0 & (x'|\delta_o) \\ 0 & 0 & (y|y_o) & (y|y_o') & 0 & 0 \\ 0 & 0 & (y'|y_o) & (y'|y_o') & 0 & 0 \\ (l|x_o) & (l|x_o') & 0 & 0 & (l|l_o) & (l|\delta_o) \\ 0 & 0 & 0 & 0 & 0 & (\delta|\delta_o) \end{bmatrix} \begin{bmatrix} x_o \\ x_o' \\ y_o \\ y_o' \\ l_o \\ \delta_o \end{bmatrix} \tag{2.19}$$

$$\vec{X} = R\vec{X}_o \tag{2.20}$$

It is not obvious from Equation (2.19) that the matrix may have been obtained after the passage of the bundles through one element in the beam line or after passage through many elements. It is of no consequence from a theoretical standpoint since one can consider a single magnet as the system or a group of magnets, with any combination of multipole fields, and associated drift spaces. To produce a matrix after beam passage through many elements one starts at the first element and multiplies its transfer matrix by that of the next element until the desired endpoint is reached. Matrix multiplication proceeds from right to left since the first element's matrix is located on the far right in order to operate on the initial state vector.

2.2.2 Definition of spectrometer parameters

In this section the pertinent parameters will be defined in an introductory fashion after some general considerations (from a first order transfer matrix point of view) have been studied with reference to spectrometers. Useful equations in beam optics are given in Appendix B.1 and B.2.

The momentum resolution is defined as the fractional change in momentum that can be detected as different momenta. It is usually normalized by a given central momentum. This quantity can be stated in other forms as given by Equation (2.21), where w_0 is the radial width of the object ($= 2X_0$), M_x is the radial magnification, D is the dispersion, ρ is the radius of curvature of a particle having momentum p, and F is the resolution function. It is apparent that a magnification less than unity is desirable to improve the resolution.

$$R_p = \frac{\Delta p}{p} = -\frac{M_x w_o}{D} = \frac{w_o}{\rho F} \tag{2.21}$$

The resolution function can be stated for uniform field magnets having normal entry by Equation (2.22) in terms of the object distance, S_0, the bend angle, α, and the bend radius, ρ, or in terms of the effective field radius by use of Equation (2.2). For extremely relativistic electrons the energy resolution equals the momentum resolution since the rest mass of the electron is a negligible contribution to the total energy of the particle. Inspection of F reveals that the resolution improves with increasing object distance and increasing bend angle up to 90^o.

$$F = \frac{S_o}{\rho}(1 + \cos\alpha) + \sin\alpha = \left[\frac{S_0}{R_m} + 1\right]\sin\alpha \tag{2.22}$$

The general transfer matrix to a point "s" is normally described by cosine and sine like functions as shown in Equation (2.23) for the dispersive plane and a similar expression for the nondispersive plane.

$$M_x(s) = = \begin{bmatrix} C_x(s) & S_x(s) & D_x(s) \\ C'_x(s) & S'_x(s) & D'_x(s) \\ 0 & 0 & 1 \end{bmatrix} \tag{2.23}$$

where

$C_x(s)$ = cosine-like trajectory: $C_x(0) = 1$; $C'_x(s) = dC_x(s)/ds$, $C'_x(0) = 1$

$S_x(s)$ = sine-like trajectory: $S_x(0) = 0$; $S'_x(s) = dS_x(s)/ds$, $S'_x(0) = 1$

$D_x(s)$ = dispersion function: $D_x(0) = 0$; $D'_x(s) = dD_x(s)/ds$, $D'_x(0) = 0$

Note that $C'_x(s) \neq S_x(s)$. It is apparent that the radial displacement of the exiting ray is related to these functions in a linear manner (to first order) and is explicitly stated in Equation (2.24).

$$X(s) = X_o C_x(s) + X'_o S(s) + \delta D(s) \tag{2.24}$$

2.3 Discussion on design parameters

In this section the pertinent quantities affecting the performance of a pair spectrometer will be discussed.

2.3.1 Resolution and Efficiency

One of the most important characteristics of a pair spectrometer is its energy resolution. There are three important components contributing to the overall energy resolution of a pair spectrometer. They are the intrinsic resolution of the magnet, the effect of the converter, and the choice of detectors. The magnet resolution is defined as the full width half maximum of the response function, normalized by the incident energy, produced by the spectrometer when analyzing particles of a certain energy. In practice this may be accomplished by sending monoenergetic particles through the spectrometer and observing the resulting spread in energy. The effect of the type and thickness of the

converter will be covered in the following section. We hope to have an overall energy resolution less than 3% (~4 MeV/150MeV) to successfully detect photon splitting and to use the PS for other applications such as a beam monitor at SAL.

The optimum relationship between the width of a detector, d_w and the distance between successive images, Δ having momentum p and $p+\Delta p$ is now obtained. For example, if the magnet can resolve images differing by 0.5 MeV but the detectors have an energy bite of 1.0 MeV then these detectors are clearly the limiting component of the overall energy resolution.

Consider the case where the image separation is greater than the detector size which is greater than the image size (refer to Figure 2.9.a). The response signals are maximal, however, the distance of no signal (Δ - d_w) is too long. In other words the images corresponding to momenta p and $p+\Delta p$ are farther apart than they need be for the signals to be just resolved. Stated in other terms the magnet has better resolution than is required since it is limited by the detector size. The other situation shown in Figure 2.9.b has the image separation, image size and detector size all equal. This is the condition when the signals are just resolved and is the ideal scenario. If the detector size is less than the image width then there is a loss of intensity in transmission and a reduction in the amount of useful data. Therefore one must be careful in choosing the appropriate detector(s) since one wishes to match their energy bite to the resolution of the magnet.

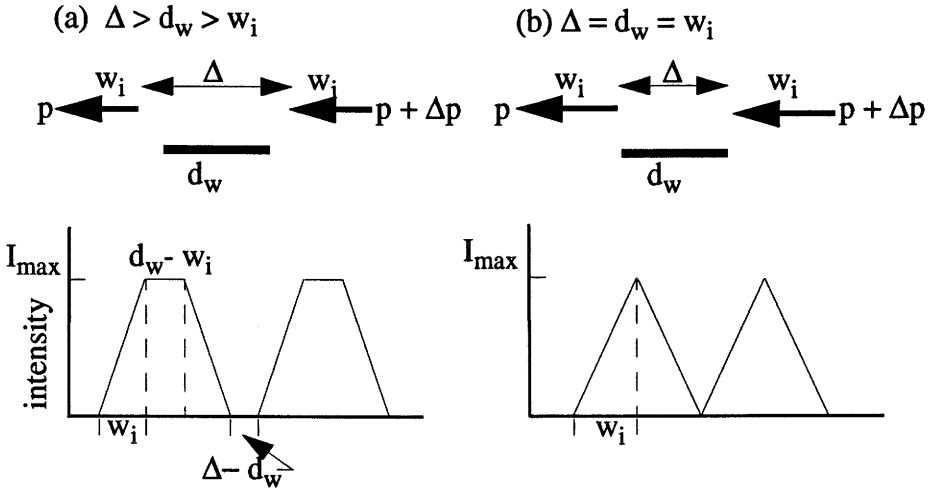

Figure 2.9. Matching the magnet resolution to the detector size.

The efficiency of the system can be simply stated as the fraction of incident γ-rays detected by the instrument. It will be shown that a compromise must be made between efficiency and resolution. The efficiency of the pair spectrometer is naturally related to the pair production conversion efficiency (among other factors). The efficiency of detection also depends on the solid angle acceptance and the kinematics of the reaction. For example, in a forward peaked reaction (such as pair production), a large solid angle acceptance in the magnetic system would gain nothing.

The number of photons incident on the converter is the number of tagged photons that make it through the collimator. The acceptance, $A(E_\gamma)$, is defined as the number of photons incident on the converter that get detected. The probability that a certain photon will pair produce (α_{pp}) is the first term in Equation (2.25). Once pair production has taken place in the converter there is a finite probability of bremsstrahlung of the resulting charged particles in the converter (α_{brem}). There is also a geometrical acceptance factor for both the electron and positron trajectories (α_{geom}) resulting from the physical constructs of the magnet and detector system. This term also includes the effects of small angle elastic scattering. Photon energy and excitation level of the magnet are implicitly defined in Equation (2.25) which gives the expression for overall acceptance. An accurate representation of this acceptance is possible with simulation of the PS using a relevant software package.

$$A(E_\gamma) = \alpha_{pp}\alpha_{geom}(1-\alpha_{brem}) \tag{2.25}$$

The preceding discussion applied to a single photon being measured. For our intended splitting experiment the efficiency is very low since the split photons must produce pairs in the converter and be detected. The efficiency of the spectrometer for photon splitting is the same as outlined if the square of the conversion probability for a single photon is inserted into Equation (2.25).

2.3.2 Effect of converter thickness

In a given thickness of converter, pair production probability is governed weakly by incident photon energy and the atomic number. For example, the probability of pair production is typically 1-2% in foil converters of high Z materials having a thickness of 2.8% L_R [Davies et al., 1954].

The cross section for pair production is proportional to Z^2. A high energy limit of the total cross section for pair production is given in Equation (2.26) where $\sigma_0 = 5.80 \times 10^{-28}$ cm^2 ($= \alpha Z^2 r_e^2$).

$$\sigma_{pair} = 4\sigma_0 \left[\frac{7}{9} \ln\left(183 Z^{-\frac{1}{3}} \right) - \frac{1}{54} \right] \tag{2.26}$$

The probability of detecting the converted pair is proportional to the energy range spanned by the detectors and their solid angle. There is also a factor for the efficiency of the detectors which is normally close to unity.

Additional spectrometer efficiency is possible if the converter thickness is increased since more charged pairs will be produced, however, there is a trade-off to be considered. Increasing the converter thickness has two effects. The first one is an increase in the energy loss due to ionizing collisions of the charged particles and this results in poorer resolution since the response function has widened. To avoid this unknown energy loss it is necessary to use very thin foil converters. The second effect results in decreasing the number of charged particles being momentum analyzed since there are also losses from bremsstrahlung, straggling and small angle scattering. Straggling results from fluctuations in energy loss of particles in the converter. If the converter is thick enough the particles will have different energy losses although they are monoenergetic. The amount of multiple scattering is a function of type of converter, thickness and energy of the particles. The angular spread arising from multiple Coulomb scattering, if severe enough, will cause particles to be scattered out of the acceptance of the magnetic spectrometer.

2.3.3 State of the art pair spectrometers

There is a semicircular pair spectrometer at Chalk River allowing independent, accurate energy measurements with an efficiency function that is known, permitting relative intensity measurements for the study of neutron capture γ-rays up to 11 MeV [Bartholomew and Lee-Whiting, 1979]. It was surmised that the slit design was the most important factor affecting the peak energy width and magnitude of the low energy tail. Three slits were constructed with each geometry having a relative advantage. Figure 2.10 shows the geometry of these apertures.

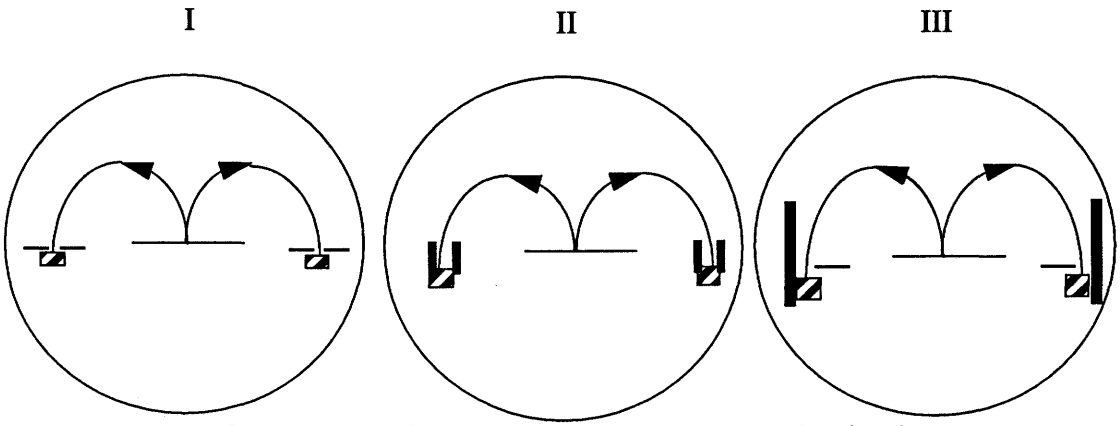

Figure 2.10. Three types of aperture geometries for the CRNL pair spectrometer.

It was shown, by analytic means, that type I apertures give the highest transmission for low resolution operation while type III does likewise for high resolution. A comparison was made of the energy tails and energy resolution for various choices of slits. Type I and II worked well with broad converters while type III was sensitive to converter size. It was determined that type II apertures gave the best overall characteristics. It had good energy resolution, high counting rates and a reduced low energy tail. The resolutions were typically 1% with type III, 0.4% in the best possible scenario. The efficiency increased by two orders of magnitude when the energy increased by a factor of 5. Unfortunately the top end on the efficiency was 10^{-6}.

A compact high resolution pair spectrometer has been developed and tested using a clamshell-shaped dipole [Höistad *et al.*, 1990] at Uppsala University. Its use is in studying nuclear reactions, especially those involving light nuclei. The FWHM energy resolution of the instrument is about 0.6 MeV over its operating range (up to 200 MeV). The compact size of the magnet allows movement to different angles with respect to the primary beam, however, this is difficult due to its bulkiness. The reduced acceptance can be balanced by increasing the beam current. This device is capable of measuring cross sections at 1 nb/sr and has been tested in a study of the $^{11}B(p,\gamma)^{12}C$ reaction at 98 MeV. A schematic diagram for the magnet is given in Figure 2.11 and Table 2.1 lists some of its specifications.

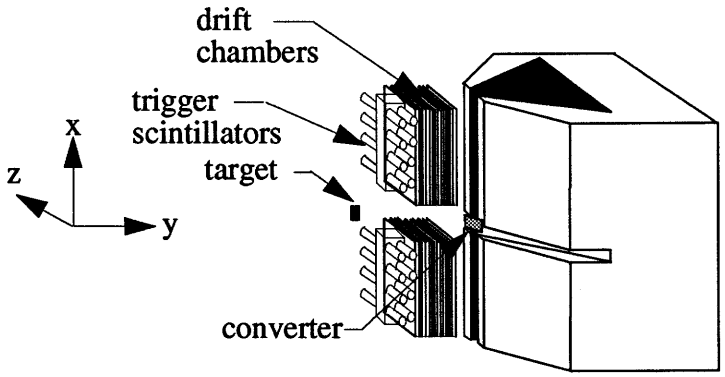

Figure 2.11. A Compact high resolution PS.

Table 2.1

Selected Specifications for the Compact PS in Uppsala.

Magnet	
Weight	45 tonnes
Pole area	220 ×70 cm^2
Pole tilt	8.3^o
Maximum momentum	200 MeV/c
Angular range	35^o to 140^o
Photon detection	
Converter type	gold
Converter thickness	0.1 mm (2.8% L_R)
Converter geometry	20.6 ×12.0 cm
Target-converter distance	58.5 cm
Solid angle	70.8 msr
Conversion probability (@ 100 MeV)	1.7%
Acceptance (@ 100 MeV)	2.5×10^{-5}
Measured energy resolution (@ 100 MeV)	0.6 MeV
Angular resolution	2.0^o

The field configuration was chosen to be non-uniform since the homogeneity causes limitations in the amount of usable volume available for momentum analysis, and a large fringe field which contributes to poor focussing properties. Variation of the magnetic field is of the form $B_o(y) = K\, y^{-n}$, where K is a constant, and n is the field gradient index. The initial photons enter along the y-axis, get converted, are bent in the vertical x-plane by 180^o and are detected by high resolution drift chambers. From the orientation of the measured pair trajectories and knowledge of the magnetic field a trace can be made back to the point of conversion in the fringe field. With this information the energy and direction of photons incident on the converter is known.

2.4 Specifications for the SAL pair spectrometer

The properties of the SAL pair spectrometer are discussed in this section and summarized in Table 2.2. In the best of all possible worlds we would probably have chosen a magnet able to bend particles by 180° with point to point focussing in two dimensions. We chose an existing flat, uniform field, circular dipole which was adequate for our purposes. A power supply borrowed from an off-line magnet was used as the mains for our dipole.

Table 2.2

Pair Spectrometer data

Magnet:	
Weight	~2 t
Pole area	2×125660 mm^2
Pole gap	50 mm
Solid angle at converter (defined by collimator)	4.38 μsr
Momentum acceptance	20 - 180 MeV/c
Dispersion (at 60 MeV)	5.45 mm/%
Magnification (at 60 MeV)	-1.17
Momentum resolution (for 1 mm beam spot)	< 2 MeV
Maximum field at P_o	10 kG
Power consumption (maximum)	13 kW
Maximum current	350 A
Resistance of coils	0.11 Ω
Dimensions	443 mm × 578 mm × 781 mm
Scintillation detectors:	
Scintillator material	NE 110
Scintillator size	25 mm × 50 mm × 3.2 mm
Number of cells	2 ×3/side

2.4.1 Optics and focussing system

Appendix B.1 gives the details of calculating the charged particles' energies (for a given detector) due to their deflection in a uniform magnetic field. Charged particle trajectories were determined using the software package *Raytrace* [Kowalski and Enge, 1986]. *Raytrace* integrates the equations of motion to generate the trajectories. Appendix B.3 shows the transfer matrix for the PS to first order obtained using this software.

The trajectory of a particle having charge q is determined by the Lorentz force which is given in Equation (2.27) where **E** is the electric field, **B** is the magnetic field and **v** is

$$F = \frac{dp}{dt} = q\,[E + v \times B] \tag{2.27}$$

the velocity. *Raytrace* solves this Equation for each component of motion using a step wise fourth order Runge-Kutta integration routine. Every element has an initial coordinate system and a final coordinate system. The existing package can have 200 elements and trace 100 rays through them. For further information on *Raytrace* one should consult the reference manual.

For the magnetic field setting chosen for the test, the focal plane was calculated using beam optics equations and was consistent with results from *Raytrace*. It was found that the focal plane had a slight curve. The best fit straight line was found for the focal plane. Using a coordinate system whose origin was situated at the center of the dipole the best fit line for the focal surface was y[mm] = 1.928x[mm] + 410.2 and started at position (-41.6, 330.2) mm and ended at (181.0, 758.9) mm. An angle near 65° was made between the focal plane and the beam direction.

2.4.2 Acceptance of the PS

The purpose of this section is to determine the acceptance of the PS. Assuming a point electron beam spot at the tagger radiator, Figure 2.12 shows the tagger radiator, the converter, the PS pole pieces, halo detector and divergence of the photon beam upon exit from the dipole yoke.

The solid angle subtended at the converter by the photon beam was defined by the downstream side of the square (3 × 3) mm lead collimator. Assuming a circular collimator of diameter 3 mm, the solid angle was approximately 4.38 (±3%) μsr.

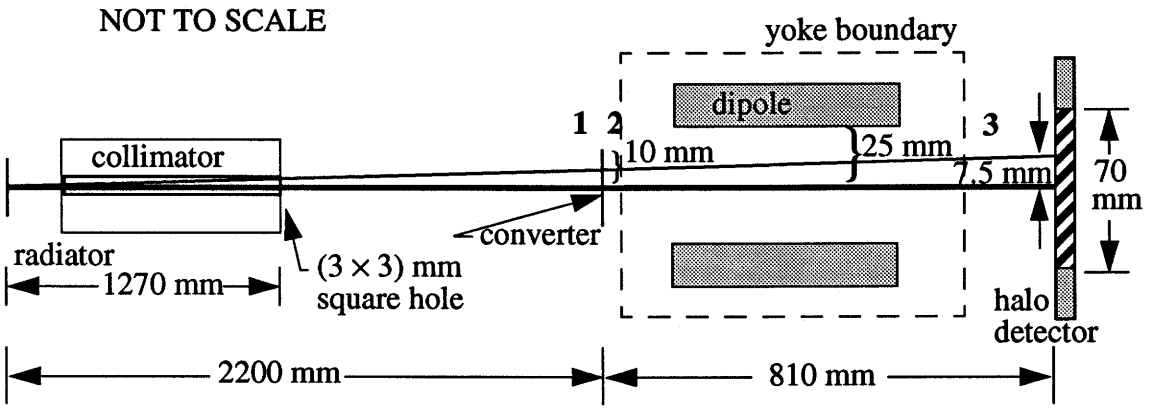

Figure 2.12. The divergence of the photon beam.

The resulting beam spot height was 5.2 mm at the converter. Photographic results gave a beam spot height of 5.0 mm on the upstream side of the converter. The downstream side of the converter produced a beam spot height of 6.0 mm and width that was 5.5 mm which was due to charged pairs being produced and scattering. Exiting from the PS yoke (along the photon beam line) the diameter of a circular photon beam spot should be about 7.1 mm. On the downstream side of the PS but before the mechanical iris the photon beam had an overall height of 7.5 mm and width of 6.5 mm. The three placements of photographic film are labelled as **1**, **2**, and **3** in Figure 2.12. This vertical spread suggests that the vertical emittance may pose a problem if smaller converters are used. For our test purposes this spread was acceptable.

The distance that charged particles (produced in the converter) travelled to reach the nearest detector was calculated from knowledge of the bend radius and position of the particle upon exit from the effective field boundary. The corresponding diagram is shown in Figure 2.13 and has the bend stretched into a straight line.

The limiting angular factor for the charged particles being accepted by the PS detectors was multiple Coulomb scattering especially in the non-dispersive plane. This scattering would cause them to miss the detectors. For example in the thickest converter (refer to Table 2.3), the root mean square (rms) scattering angle was 406 mr for electrons that travelled through this entire thickness. In the thinnest square converter the rms scattering angle was reduced to 144 mr. For comparison the opening angle for pair production is less than 10 mr. Simulations using Raytrace gave point to point focussing for angles up to ±

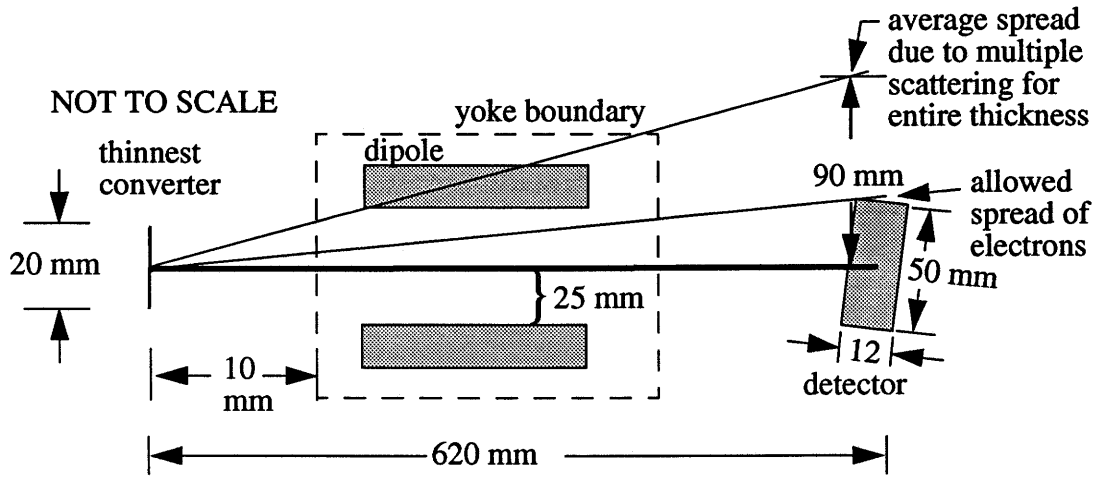

Figure 2.13. The effect of multiple scattering.

200 mr in the radial (bend) plane. The vertical angle limit was determined from the height of the scintillation detector to be ± 40 mr hence many particles miss the detectors. The scintillators had an active area of (12 ×50) mm due to their edge on placement.

2.4.3 Detectors

We chose to use scintillators and photomultiplier tubes since SAL has extensive experience with these devices. We used the design made for the SAL tagger focal plane as our detectors. The energy lost by a charged particle may excite the atoms in a scintillator and the de-excitation produces light. The light output from the scintillator is directly proportional to the ionization energy deposited in the scintillator which excited it. The time response of the detector is another characteristic that needs attention, faster detectors enable us to use higher counting rates and reduces background.

There were three detectors per focal plane in the test configuration of the PS, one at each end and one approximately in the middle. A detailed drawing of a single detector and its circuit board is given in Figure 2.14. In each of the six detectors was a 25 mm × 50 mm × 3.2 mm wafer of NE 110 scintillator. This type of scintillator has a light attenuation length of 400 cm, a risetime of 1 ns, a decay time of ~3 ns and a pulse FWHM of 4.2 ns. Attached to the scintillator was an adiabatic, tapered light guide having a length of 215 mm. The light guide was fitted into an aluminum mounting piece that enabled it to be optically coupled to a spring-loaded photomultiplier tube (PMT).

These PMTs (Philips XP 1110) have a gain of ~1.0×10^6 (at 1200 V) and a risetime of 2.4 ns. The light guides transport scintillation light to the photocathode which has a low work function to aid in electron emissions. The light produces photoelectrons that are accelerated to the first stage (dynode) of the tube which promotes secondary emissions of electrons at a ratio of about 4 per incident electron. Several such stages are passed through to produce the output current that is collected at the anode.

2.4.3.a Fabrication, testing and mounting

Spare SAL tagger detectors were available so they were used in the test run. After this commissioning test the detectors were modified to include a straight light guide as requested for the final configuration of the PS. For these new detectors shop time was used for the wiring, fabrication of light guides, aluminum tubing, and end connectors. The printed circuit boards were manufactured by Custom Circuits of Regina.

Regardless of the type of detector used, testing consisted of the same three steps. First the photomultiplier tube bases were checked alone to ensure they could handle -1200 V, next the base and phototube were connected and checked to ensure that no light leaked in. If light was leaking in then there should be noise produced on an oscilloscope connected to the output. The final step for testing the PS detectors consisted of setting the photomultiplier tube voltage to detect minimum ionizing particles (MIP) such that the response on an oscilloscope showed a pulse height greater than 30 mV and was the same for each tube since 30 mV corresponded to the discriminator threshold. Minimum ionizing particles deposit between 1.9 to 2.0 MeV/(g cm^2), fairly independent of their energy, thus they give very similar pulse heights when traversing the detectors.

A Ru^{106} source was used to produce MIP since it beta decays to Rh^{106} which in turn beta decays almost immediately, giving electrons with an endpoint energy of 3.54 MeV. Some of these electrons would pass through the detector under test and strike a secondary detector that was placed directly behind the first one. Using the second detector as a trigger, the nearly uniform pulse heights (of the minimum unionizing particles) from the test detector were observed on the oscilloscope. The pulse height was then set by adjusting the negative high voltage to the tube.

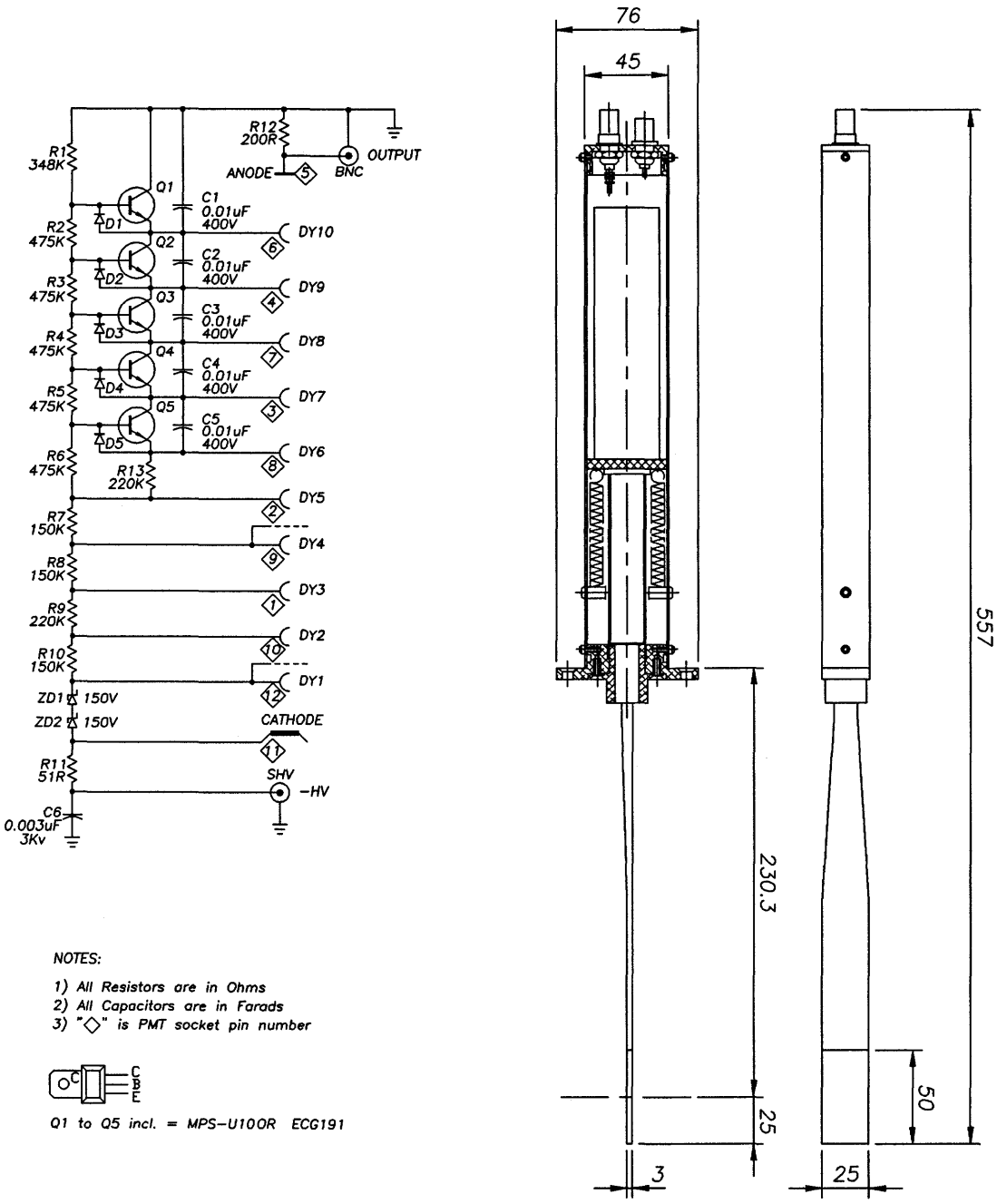

NOTE: All dimensions are in mm.

Figure 2.14. Circuit diagram for printed circuit board and scale drawing of a single detector.

2.4.4 Photon Converters

The size and shape of the copper (radiation length, L_R, of copper is 14.3 mm) converters used in the test are summarized in Table 2.3.

Table 2.3. Converter specifications

converter	shape	radiation length (%)	thickness (±0.05 mm)
1	square [20 ×20] mm	31.8	4.55
2	square [20 ×20] mm	11.2	1.60
3	square [20 ×20] mm	4.9	0.70
4	annular (ID = 7 mm, OD =16 mm)	8.7	1.25
5	over/under [6 × 6] mm, air gap =7 mm	9.1	1.30

As was discussed in Chapter 1, the kinematics of the reaction dictate that splitting occurs at small forward angles. Therefore an annular converter will be used to allow the unsplit photons to pass through the inner annulus but the split photons would hit the annular converter.

The first three converters were simple foils. The annular converter allowed photons to convert if they were off axis (in any direction) by an amount between 3.5 and 8 mm. This converter had an effective area of 162.6 mm^2. The last type of converter was the over/ under converter, consisting of two copper foils separated by 7 mm. Similar to the annular converter, photons that were vertically off axis by an amount between 3.5 and 9.5 mm could be converted.

A detailed drawing of the pair spectrometer used in the test run is shown in Figure 2.15. The coordinate system used in the test is superimposed on the drawing.

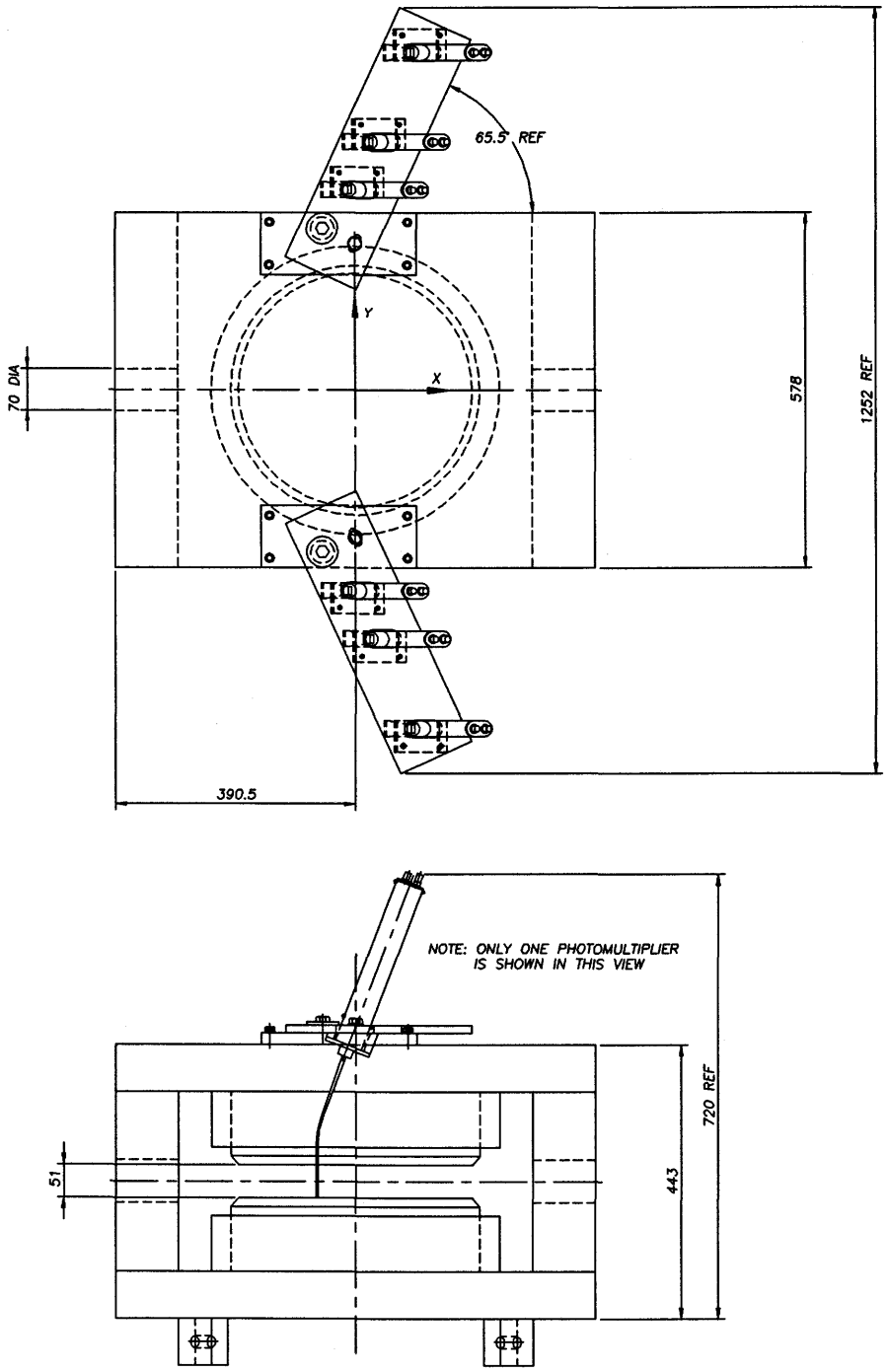

Figure 2.15. A scale drawing of the pair spectrometer.

Chapter 3. THE COMMISSIONING TEST

3.1 The SAL Facility

The SAL facility consists of a 6 section electron linear accelerator (linac), an energy compression system (ECS) and a pulse stretcher ring (PSR) that produces a nearly monochromatic electron beam with low emittance at a high duty factor. It also has experimental areas to utilize this beam. The electron beam can be used for bremsstrahlung experiments or electron scattering. Figure 3.1 illustrates the floor plan of the facility. The system has been detailed previously [Amendt 1991].

Electrons from a button cathode are accelerated in an electron gun to approximately 220 keV. The electron beam is velocity modulated to form bunches which drift into accelerating sections where they gain up to 50 MeV/section, boosting them to a maximum peak energy of about 300 MeV. The linear accelerator sections consist of an evacuated waveguide with a periodic array of cavities, complete descriptions have been given [Neal et al., 1968]. Each section is driven by a 2856 MHz klystron transmitter whose peak power is about 22 MW. Beam pulses are up to 1μs in length with a repetition rate of 360 Hz, therefore the duty cycle of the pulsed electron beam is about 0.03%.

Following the linac is the ECS, whose function is to reduce the momentum spread of the electron beam by a factor of 10, to ~0.1% (under optimal conditions), without degrading the beam current. It consists of three dipole magnets, in a chicane configuration, with the center dipole having a reverse bend. This is followed by a compact RF accelerating section. The ECS magnets were designed to form an achromat (no transverse dispersion) but have a longitudinal dispersion of 1.7 cm/% and has been described elsewhere [Laxdal,1980]. Electrons emerging from the three dipole system have lower energy particles lagging those of higher energy because of a longer path length through the magnets. The original tight electron bunch is thus spread out longitudinally as it enters the RF correcting section. Low energy electrons are accelerated and high energy ones are decelerated by the correcting field giving a smaller momentum spread in the beam.

The injection line bends the beam by 180^{o} and transports it up to the plane of the PSR. The injection line was designed to give the correct phase-space matching of the beam to the PSR machine parameters.

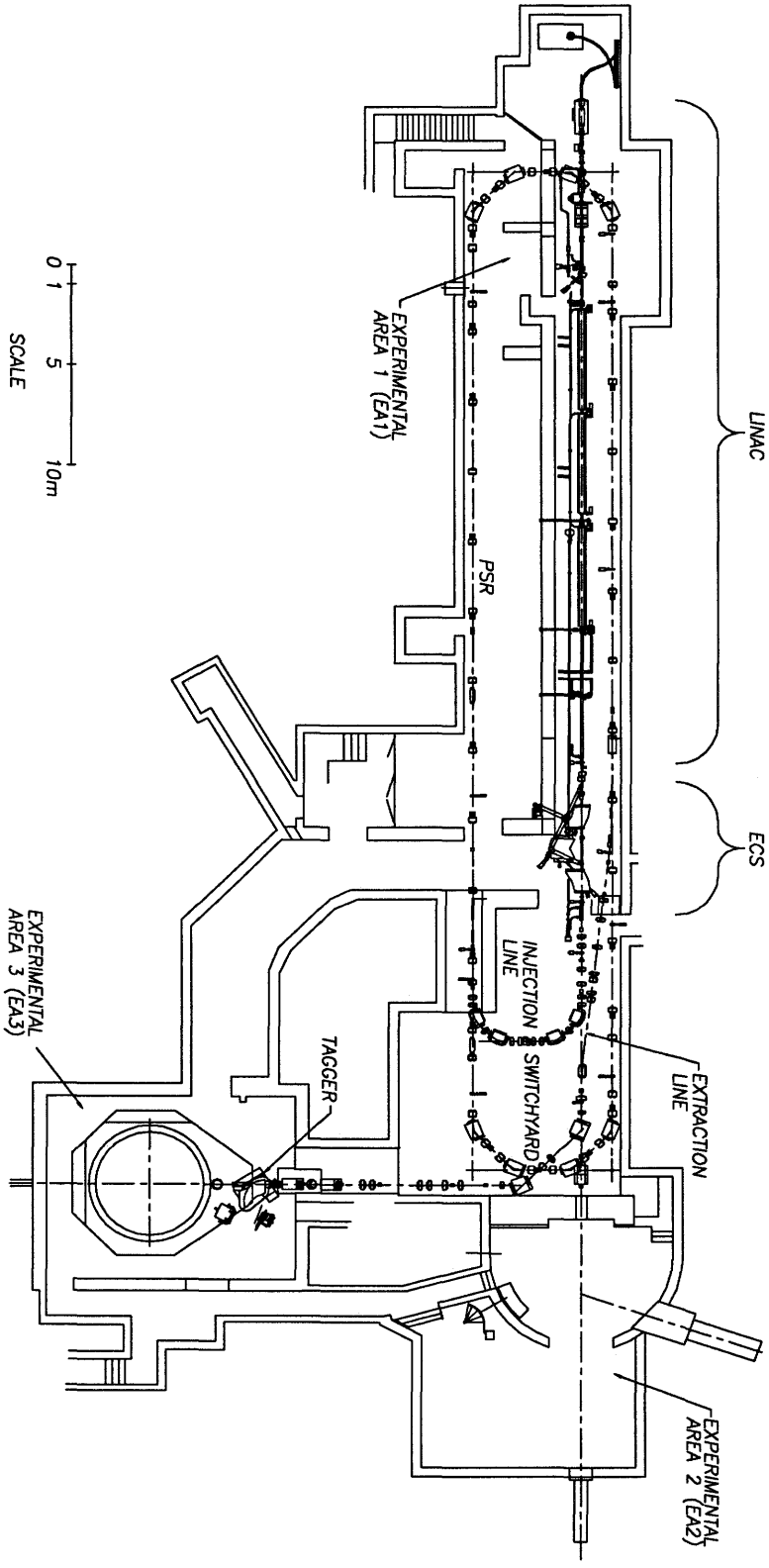

Figure 3.1. The floor plan of the Accelerator Laboratory.

The PSR accepts the intermittent pulses emerging from the accelerator (using one turn injection), stores it, and continuously extracts it prior to the arrival of the next pulse. The ring has two 180° bends consisting of 4 equivalent cells designed for 2π phase advance and to be achromats in first order theory. The two straight section have three identical cells. There is an RF cavity in the straight section whose purpose is to control the rate of energy loss or re-supply energy to the circulating electrons. The operation of the PSR has been described elsewhere [Dallin, 1990].

The electron beam is extracted slowly via betatron oscillations (using a one-third resonance tune) between linac pulses resulting in a nearly continuous beam of monoenergetic electrons. The energy at injection is slightly above that for extraction. As the electrons lose energy (by synchrotron radiation emissions) they approach the resonance tune and are extracted. Extraction is accomplished using an electrostatic extraction septum to "peel off" electrons. The oscillation amplitude becomes large enough such that the electrons enter the septum's electrostatic field and are deflected to the magnetic septum which finally directs them down the extraction line. Next the beam enters the switchyard and is directed to the desired experimental area.

3.2 The SAL Tagger

The SAL tagger was originally used in Experimental Area three (EA3) but has since been moved to EA2 (see Figure 3.1) and allows measurements of nuclear reactions using tagged photons in a bremsstrahlung beam. Bremsstrahlung is the dominant mode of energy loss for high energy electrons. Energy is conserved according to $E_\gamma = E_0 - E_e$ (where E_0 is the energy of the electron beam and E_e is the energy of the recoiling electrons, and E_γ is the tagged photon energy) since the recoiling nucleus required to conserve momentum takes up negligible energy. The bremsstrahlung spectrum (Figure 3.2) is highly peaked for low energy photons. The bremsstrahlung photons are emitted at small

angles relative to the electron beam. The characteristic angle of the bremsstrahlung cone is $\bar{\theta}_o = m_0c^2/E_e$ where m_0c^2 is the electron rest energy. In our case the electron beam energy was close to 146 MeV, thus $\bar{\theta}_o \cong 3.5$ mr.

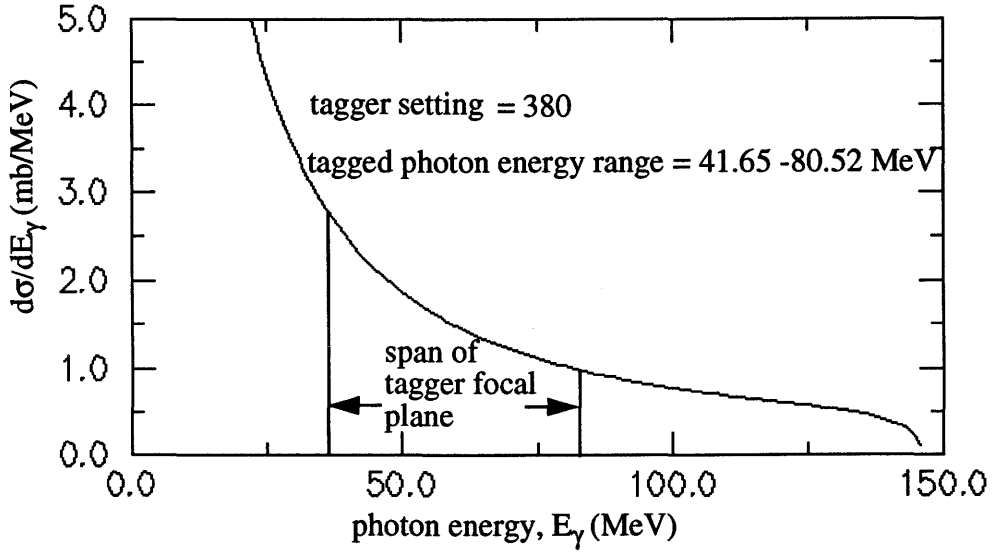

Figure 3.2. Energy range of tagged photons.

Figure 3.3 shows a schematic diagram of the tagger at SAL and Table 3.1 gives its specifications. The concept behind the principle of photon tagging is to measure E_e, the energy of the post bremsstrahlung electron, and then apply energy conservation to obtain the energy of the tagged photon. Incident electrons having energy E_0 interact with a thin metal foil (115 μm, ~0.1% L_R) producing the bremsstrahlung beam. These electrons and the noninteracting electrons are bent by the clamshell type tagger magnet. However, the maximum tagged photon energy is not equal to the photon energy that corresponds to the tip of the bremsstrahlung spectrum since the yoke of the tagger magnet would interfere with these electrons. The vast majority of electrons do not radiate and are directed to a shielded primary electron beam dump. An excellent description of the SAL photon tagger has been given previously [Vogt et al., 1993].

The energy loss from ionizing collisions in a radiator was discussed earlier in Section 2.3.1. Here we are concerned with the amount of multiple scattering which increases the angular spread of the electron and photon beams. Thus there is more background in the tagger focal plane and a larger photon beam spot size. The 0.1% radiator was chosen to produce bremsstrahlung at a rate the SAL tagger could process, while keeping multiple scattering and energy loss within acceptable limits.

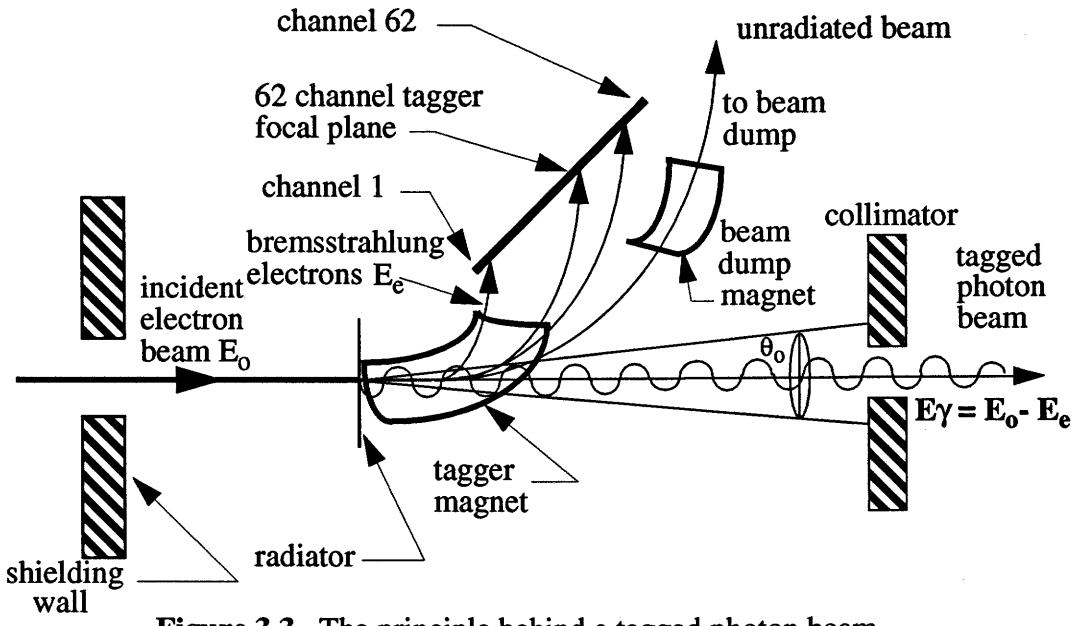

Figure 3.3. The principle behind a tagged photon beam

Table 3.1

Specifications for the SAL photon tagging spectrometer

maximum central momentum, P_0	200 MeV/c
energy acceptance	40% (0.6 - 1.4 P_0)
solid angle acceptance	10 msr
dispersion (for P_0)	1.15 cm/%
magnification (for P_0)	-1.2
first order optics	
horizontal	point to point
vertical	parallel to point
momentum resolution (for 1 mm beam spot)	0.1%
angle between pole faces	100 mrad
pole gap	80 - 150 mm
power consumption (for P_0)	53 kW

The 62 channel focal plane detector is positioned such that only the interacting electrons are recorded. Each channel had an energy bite less than 0.5 MeV. It is apparent (from Figure 3.3) that electrons with higher energies have a larger radius of curvature in the tagger magnet and will strike higher numbered tagger channels. After production, the photon beam is collimated to define the size of the beam, remove any beam halo and is then ready for use in photonuclear experiments.

Users choose their tagged photon energy range efficiently using an in-house program called "tageng" [Pywell, 1992]. Input required is the electron beam energy (146 MeV for this test run) and the setting number (380) or alternatively, the tagger central momentum which determines the energy range of analyzed electrons. Refer back to Figure 3.2 for a conceptual view of the user defined tagged photon energy range. Appendix D.1 contains the output from such a program which shows the range of photon energies.

So far we have shown how the arrival of the electron at a particular detector in the tagger focal plane gives the energy of the corresponding tagged photon. The time of arrival of the recoiling electron is now used to indicate the time the photon hits the photo-nuclear target. If a detector looking at the target detects a product (X) within the timing window set between the tagger and experimental arm (i.e. a coincidence) then we assign the reaction to that tagged photon. This is not always so, however, since there are random coincidences. Random coincidences are caused by uncorrelated (in time) post-bremsstrahlung electrons (or cosmic rays) and X-arm products from a reaction due to an untagged photon.

A tagger TDC (time-to-digital converter) spectrum of the time difference between the X-arm detector's signal and the electron recorded in the tagger focal plane will show a sharp prompt peak superimposed on a relatively flat background from random coincidences. Figure 3.4 shows a typical sharp peak obtained from a coincidence in the focal plane and in both arms of the pair spectrometer. This is due to events in the tagger focal plane that are correlated with a particle(s) detected in the X-arm electronics. These are labelled as correlated events, that is they fell within the prompt peak of the TDC spectrum. They consist of valid tagged events above a relatively flat background and the background itself which consists of random events. The other type is due to random hits in the tagger focal plane and they correspond to particles detected in the X-arm that are uncorrelated with hits in the tagger focal plane. These are labelled as uncorrelated events and occur on either side of the prompt peak and under it, too. Thus there are uncorrelated events inside the prompt peak which must be subtracted out to obtain the true yield. It is usual to treat the uncorrelated events in the tagger focal plane in a similar manner to the correlated events when they are beneath the prompt peak and subtract the normalized spectra of the foreground/background ratio. Chapter 4 details the analysis method and background subtraction.

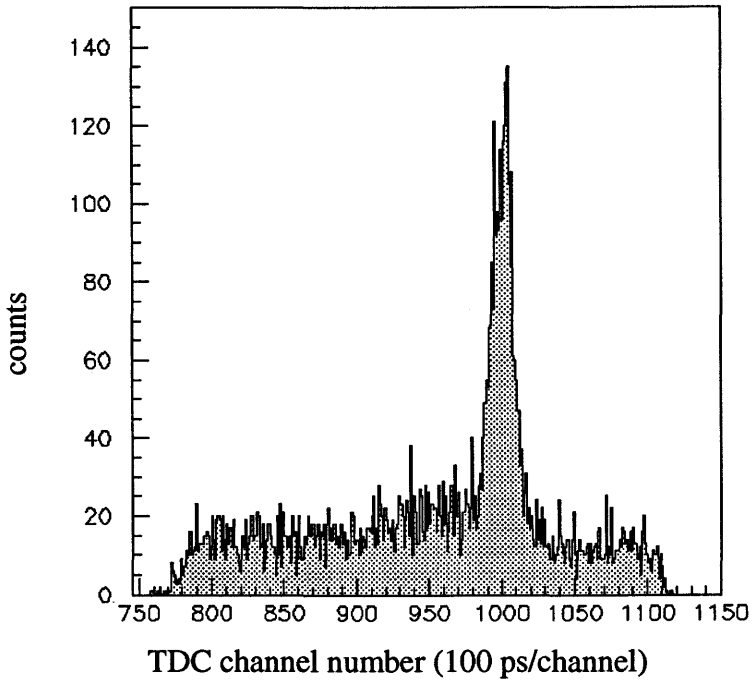

Figure 3.4. A typical tagger channel TDC spectrum.

It would appear that there is a simple one to one relation between a hit in the tagger focal plane and the experimental arm. However, there may be multiple electron hits in the tagger focal plane occurring within the resolving time between the tagger and the experimental arm detectors, therefore the interpretation is complicated. This is commonly termed multiple hits in the tagger focal plane or simply multiples. This leads to an ambiguity in the energy of the recoiling electron and thus the tagged photon energy. As the counting rate is increased, by use of a thicker radiator and/or increasing the beam current, the rate of bremsstrahlung radiation is also increased, increasing the multiplicity in the tagger focal plane, and increasing the background.

3.2.1 Other Considerations

Effects such as random coincidences and multiple hit events depend on the instantaneous counting rate. For example, an important consideration in reducing the number of random coincidences is a low instantaneous incident electron rate which in turn requires a high duty factor beam to give constant luminosity. The method of measuring the duty factor (using the tagger) is based on the formula for the number of random coincidences given in Equation 3.1 where N_A is the number of counts in tagger channel A (similarly for detector B), N_{AB} is the number of random coincidences, d is the duty factor, T is the

real time and τ is the resolving time of the coincidences. In our case the number of hits in two counters (two separated tagger channels), is just the number of counts which are independent since they are separated by several channels on the tagger focal plane and the number of coincidences between them are random. Solving (3.1) for d one obtains the duty factor which is as precise as the resolution of the random coincidences' resolving time. A duty factor meter based on Equation (3.1) [Vogt et al., 1994] has been built and is in operation in conjunction with the tagger.

$$N_{AB} = \frac{N_A N_B \tau}{d \cdot T} \tag{3.1}$$

Another concern is the tagging efficiency which is essential for determining the total flux of photons and is required for determining experimental cross sections. A number of photons produced at the radiator do not make it through the collimator and are therefore not incident on the reaction target. The fraction of tagged photons which pass through the collimator(s) and hit the target is defined as the tagging efficiency. Appendix D.2 contains further details on the tagging efficiency.

3.3 Experimental Layout

The equipment used for the test was mounted in the tagged photon beam immediately after the tagger outrun window. The outrun window was the interface from vacuum to air for the tagged photons and was made as thin as possible (Al, 0.5 mm) to suppress undesirable reactions. After the tagger outrun window the beam was entirely in air. Shielding walls were strategically placed to protect the PS detectors from particles that were scattered from the electron beam dump. Figure 3.5 shows the layout of our apparatus after the tagger. The overall length of our apparatus was under 2 m.

Emerging from a shielding wall, the tagged photon beam was immediately collimated by a 3×3 mm square hole cut in a 15 cm long lead brick. After 2 cm the beam passed through a secondary Pb shielding wall with a hole in it and entered an air drift space that was about 30 cm. A small horseshoe type sweep magnet was placed after a second Pb shielding wall to deflect any charged particles produced up to this point. After another drift space (~50 cm) in air, the clean, collimated photon beam was ready for interaction with a copper converter.

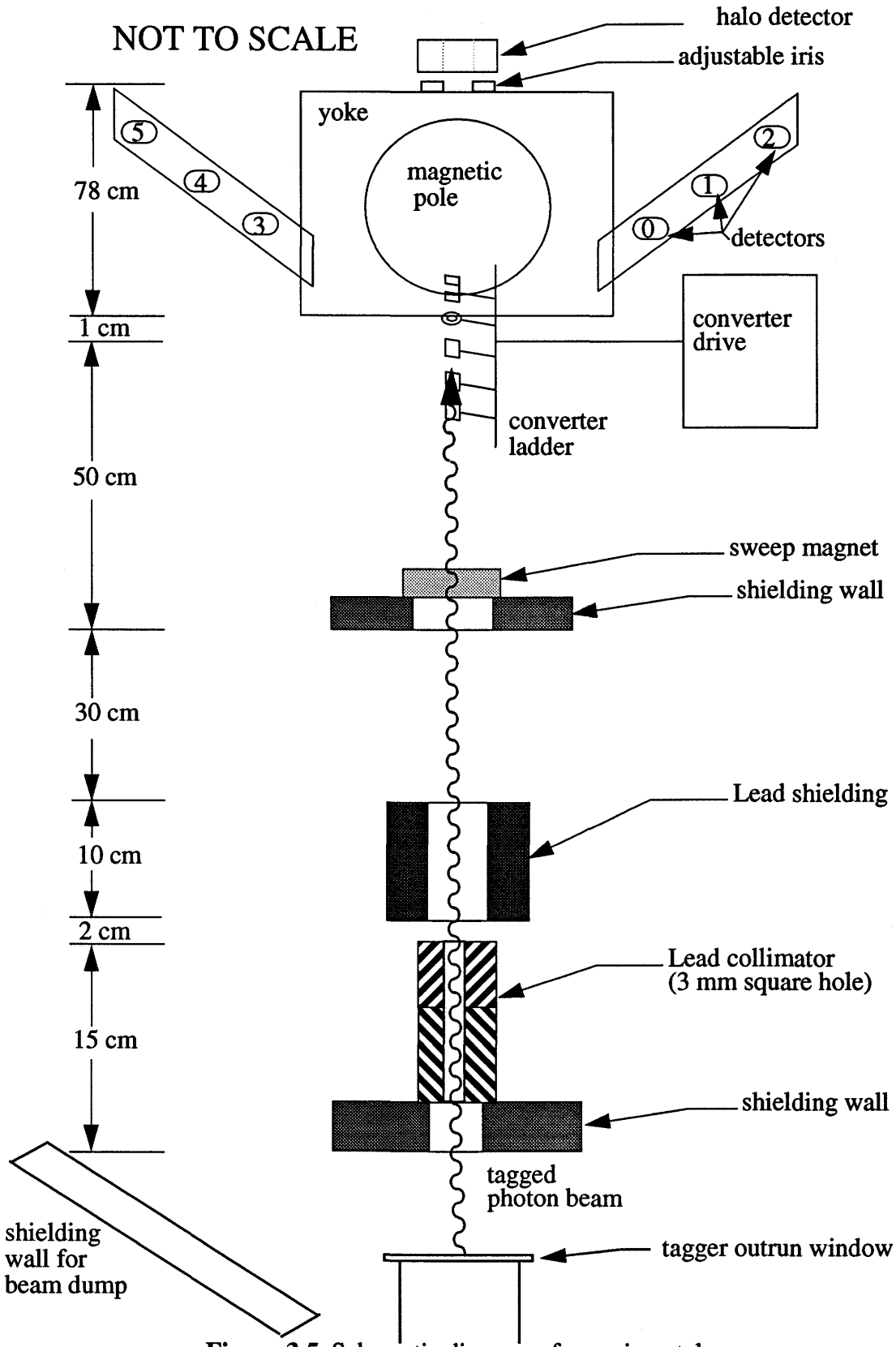

Figure 3.5. Schematic diagram of experimental arrangement used for the pair spectrometer test

The remotely controlled converter ladder contained five converters and was situated 1 cm from the outer yoke of the magnet. A specific converter could be positioned in the beam line to an accuracy of better than 1 mm. The distance from the converter to the effective field boundary of the dipole (refer to Appendix A.2) is termed the object distance and was 21.5 cm. It was possible to observe which converter was in place with a television camera focussed on the converter drive. The unconverted photon beam and charged particles passed through a 7 cm hole in the PS magnet yoke. The tagged photon beam exited through a hole of similar diameter on the other side.

On the downstream side of the second hole in the yoke was the halo detector, consisting of an adjustable plastic iris followed by an annular scintillation detector. The purpose of this detector was to get an indication of the relative amount of beam halo. A cam and stepping motor enabled remote control of the iris. The iris had movement from 4.8 mm to 42.0 mm diameter. Any beam outside the iris radius would interact with the iris and produce counts in the annular detector. Calibration of the iris was done prior to the experiment to an accuracy of better than 1 mm in diameter. An aperture value was known from a camera focussed on the stationary graduated scale on the iris. The halo detector had a inner diameter of 50 mm, an outer diameter of 150 mm, and a thickness of 15 mm. The amount of beam halo greater than a certain radius was measured by adjusting the iris to this radius and observing the count rate seen by the halo detector. A series of iris settings can give an integrated estimate of the amount of beam halo. During all runs, except the dedicated halo runs, the iris aperture was maximal. It was estimated that the alignment accuracy of the iris and halo detector relative to the PS was approximately 1 mm.

The six scintillation detectors used have already been described in Chapter 2. Their placement in the focal plane was vertical having the center of the scintillators in the magnetic midplane but outside the magnetic field. The orientation of the scintillators (at right angles to the incident photon beam) was such that the charged particles passed through at an angle as opposed to striking normal to the scintillators. The geometry is depicted in Figure 3.6 and the particles' average deviation from the normal of the PS scintillator face are given in Table 3.2 along with their relative placements. Again, it should be mentioned that the angles are only correct if the spectrometer is used in a Browne-Buchner configuration where all particles appear to originate from the center of the

magnet. The scintillators then, were placed nearly edge on to the deflected particles which was not planned. However, this placement reduced the detectors' energy bite since the scintillator area *seen* by the particles was about half of the physical area and improved the energy resolution of the PS.

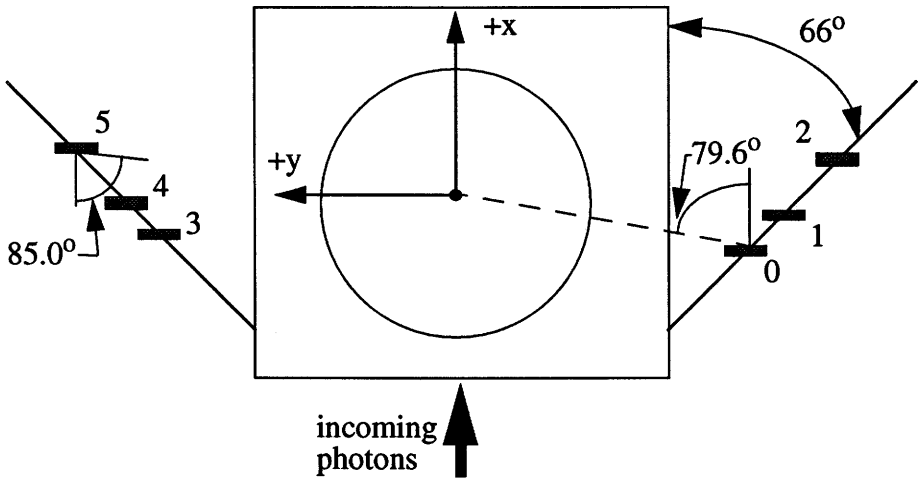

Figure 3.6. Schematic showing orientation of PS detectors.

Table 3.2. Placement of PS detectors

detector number	x (± 3 mm)	y (± 3 mm)	angle from normal (±0.5°)	Average energies for B=0.5 T
0	-60	-327	79.6	26.25
1	-17	-405	87.6	30.20
2	49	-550	84.9	34.40
3	-48	327	81.6	27.20
4	-14	406	88.0	30.43
5	48	552	85.0	34.36

3.4 Electronics

Figure 3.7 shows the schematic diagram of the fast electronics (CAMAC standard) set up used for this test and is mainly concerned with the X-(experimental) arm. The signature of an e^- - e^+ pair was a coincidence between any counter on the left and any counter on

the right side of the PS. This event is called an X-trigger. If the X-trigger itself is in coincidence with an electron in the focal plane of the tagger, the tagger electronics generates a signal called an X-reference. Thus the Boolean expression for the logic used to define a two-way hit is (1+2+3)•(4+5+6)•tagger, where "+" is the logical OR and "•" is the logical AND.

The six detector signals were treated identically. Passive splitters were used to keep the signals linear and avoid baseline drift (top of Figure 3.7) while providing input to a constant fraction discriminator (Ortec 934, CFD) and to analog to digital converters (LeCroy 2249A, ADC). The discriminators produced logic signals that were used for timing and triggering. The ADCs were gated by the tagger electronics every time an X-ref occurred. Gate duration was set at 50 nanoseconds (ns) and was provided by the X-reference signal from the tagger. The ADC gave a number proportional to the scintillator light output which in turn is proportional to the energy deposited in the scintillators. Pulses greater than -600 mV in amplitude were accepted by the ADC. Delays were required since the signals took a longer time to reach the tagger electronics than the ADCs. The delays were accomplished with variable lengths of cable.

Constant fraction discriminators were used to produce a trigger signal whose relative timing was almost independent of the pulse height of the input signal. The CFD input thresholds were set to 30 mV and the output widths to 15 ns. One set (six total) of discriminator signals was sent to the logic fanout (LC757) and another set of signals were fed into two 3-way logical ORs (365 AL) while a third set of signals went to TDCs for the PS and served as a stop signal.

The fanout served as a source of signals for the LC 4434 scaler module that counted hits in all PS detectors. The scalers were read and cleared every 30 seconds and were printed out at the end of each run (see Figure 3.9 for typical scaler outputs). Other outputs from the fanout were used for the tagger status word which records the hit pattern in the detectors. The fanout was also used for the halo detectors signal which was discriminated and counted by the scaler module.

The 365 AL logic unit could perform logical OR or AND functions. It was continuously updating therefore it could be retriggered while the current output pulse was being generated. The two outputs from each of the 3-way ORed modules were fed into another

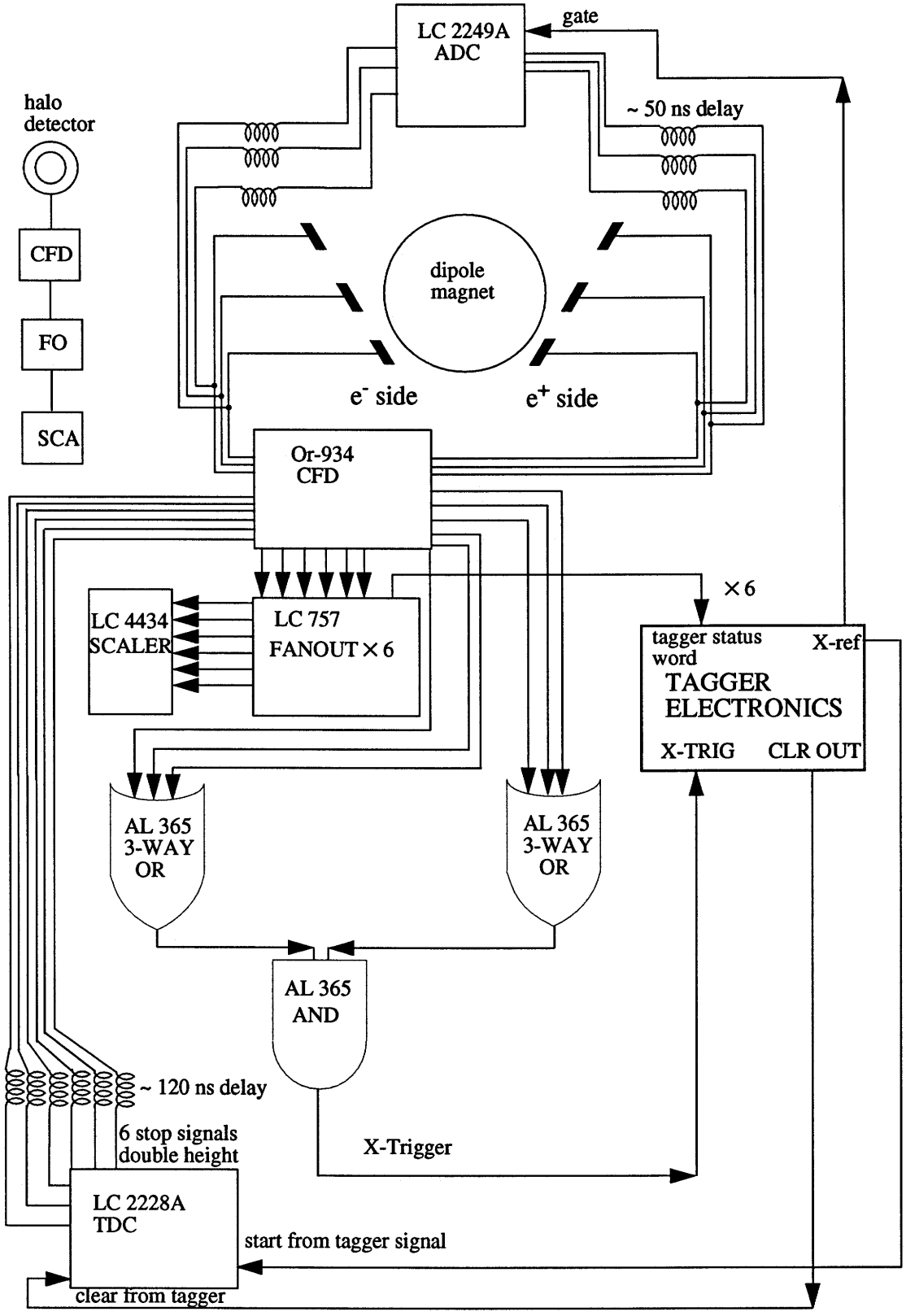

Figure 3.7. Schematic diagram of electronics setup.

365 AL module that functioned as a logical AND to generate the X-trigger. The timing window for two opposite hits in the PS was set to 35 ns. The timing window for the X-arm and tagger was set to ~40 ns.

The start for the PS TDCs came from the tagger when a hit occurred in the tagger focal plane. Stop signals (generated by the X-arm electronics) were doubled in height to keep thresholds constant and received a delay (based on the tagger time window) of ~120 ns again using the appropriate length of cable. Thus the six TDCs showed sharp spikes for valid events corresponding to the relatively constant time difference between starts and stops.

3.5 Data Acquisition

The VME fastbus data acquisition unit [Norum, 1993] made its debut in our test run to collect data from a CAMAC crate and send it to a SUN workstation running the SAL data acquisition/analysis software package LUCID [SAL, 1990]. This software package was specifically written for data acquisition and analysis in experiments performed at SAL. LUCID allowed us to read, analyze certain situations and write ADC/TDC values and tagged data for each event that was recorded.

Figure 3.8 shows a block diagram of data handling illustrating the relation between the hardware set up and software used in this test. The system's primary component is the VME front end computer, having 16 MB of dynamic RAM, VME and Ethernet compatibility, and can acquire data from CAMAC and/or FASTBUS modules. In our case only CAMAC modules were used. These modules are controlled by the front end via a parallel branch highway accepting electronically processed events from the detectors.

LUCID allowed the user to interact with the electronics and the data stream. LUCID has three primary components: the reader, writer and looker. The reader allows data to be acquired, either from the experimental electronics or from previously written events on tape or disk. The writer writes data for permanent storage and the looker samples and analyzes the incoming data to verify the proper operation of the experiment or to analyze the data.

The reader specifies the type and position of CAMAC modules used and any other variables required. It can also specify conditions that cause each type of event to be executed. Events are triggered by a CAMAC LAM (look at me) or by subsidiary triggers within other events. Finally the reader specifies actions to take in response to an event trigger. Many different types of triggers are allowed.

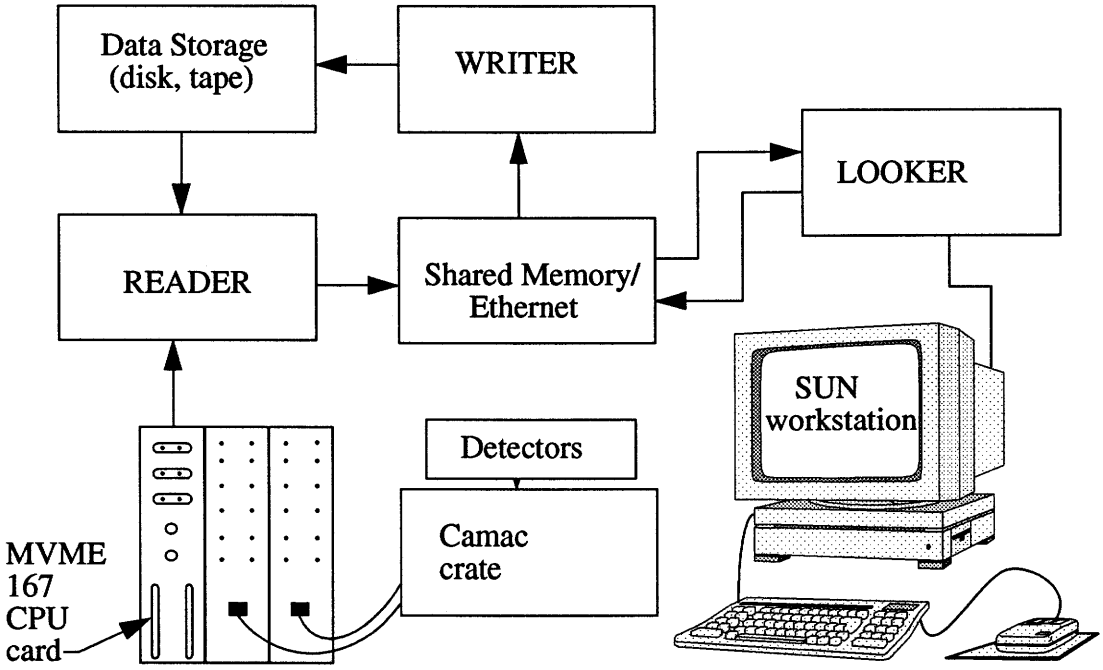

Figure 3.8. Block diagram of data acquisition system.

The writer's purpose is to save data produced by the reader for further off-line analysis. It is customary to have the writer interfacing with an Exabyte (EXB-8200) tape drive that writes to standard 8 mm video tape (Sony P6-120 MP). A single tape can hold up to 1.8 gigabytes of data. Once tapes were made and copied, it was possible to perform off-line analysis as many times as needed. The maximum rate of writing to tape in a continuous manner is approximately 245 kilobytes per second.

User written software for the looker allowed on-line sampling of data. When the looker is used for off-line analysis detailed code can be implemented to filter out unwanted events once a certain trigger has been met, such as a coincidence between the tagger and experimental arm, and manipulate the remaining events. With suitable coding

the looker processes the data based upon a given set of instructions. A quick first pass is normally obtained from on-line analysis whereas complex filtering is done in an iterative manner in off-line analysis.

3.6 Experimental procedure

Preparations for the test of the PS began in the fall of 1991. The dipole was first tested by measuring a calibration curve (magnetic field strength as a function of current applied to the coils). Other work included a center line field map of the dipole to determine the effective field boundary (refer to Appendix A.2) as well as applying the pertinent equations from beam optics, to find the focal plane. The beam line for the test was also designed. The actual test was carried out in May 1992. The equipment was set up and then the optical axis was surveyed onto the beam line with an accuracy of 1 mm. The first part was the commissioning of the PS, followed by an attempt to look for photon splitting events.

It should be noted that tagging efficiency runs (refer to Appendix D.2) were not carried out for this test of the pair spectrometer. However, we were more concerned with the satisfactory operation of the PS and how it responded under varying test conditions. This did not require knowledge of the incident flux of tagged photons unless cross sections were to be extracted from this test run.

As mentioned, the collimator used for the photon beam was quite small (3×3) mm since a small beam spot is desirable when detecting events due to photon splitting that occur at very small angles relative to the primary beam. To compensate for the size of the collimator (which reduces the number of tagged photons incident on the experimental target) we ran at relatively high beam currents (~10 μA) giving a nominal counting rate in a specific tagger channel (29) of 1 MHz.

Since we eventually planned to look for photon splitting events up to incident tagged photon energies of 150 MeV, we assumed the split photons would emerge with roughly half of this energy (of course they can have any combination of energies which add to the incident photon energy). To this end we measured tagged photons of energies between 50 and 70 MeV in our test run.

The bulk of the runs examined the performance of the spectrometer for varying conditions without the splitting target being present. The PS detectors were placed to *discretely* analyze electron/positron energies between 25 and 35 MeV with a single detector having an energy bite of 1.5 MeV (refer back to Table 3.2). The reconstructed photon energy measured by the PS was compared to the corresponding tagged photon energy. The geometry and thickness of converters were changed and their effects were observed. Other factors were also changed including the magnetic field strength, tagging rates, and so forth, however, the changes were made in a judicious manner since only one parameter, two at most, were different from the standard configuration in any given run.

All runs were compared to a run labelled as standard. The standard run had the following properties:

- a converter
- tagger channel 29 (E29) rate = 1 MHz
- tagger radiator 7 (Al, 0.1% L_R)
- sweep magnet after collimator
- PS field = 0.5 T and normal polarity
- tagger central momentum = 75 MeV/c

A run summary is given in Table 3.3 and labels any difference between the standard run (in an abbreviated form), the number of opposite side coincidences in the PS, and the total counts in the tagger focal plane which was used for normalization purposes.

Table 3.3. Run Summary

Run number	Remarks	PS (2-way) coincidences	Tagger channel sum ($x10^{11}$)
9	standard	41285	2.448
10	thin rad., std conv	33810	2.722
11	thick conv.	44944	2.060
12	no rad., thick conv	0	0.001

Table 3.3. Run Summary

Run number	Remarks	PS (2-way) coincidences	Tagger channel sum ($x10^{11}$)
16	magnet polarity reversed	46863	2.613
17	no B field, thick converter	444	1.734
19	no converter	4099	2.307
20	thin rad	102840	4.009
21	E29 rate is 3.8 MHz (340 s.)	52223	1.253
22	annular conv	9126	1.997
23	over/under conv.	4610	1.878
24	tagger magnet at 55 MeV	51937	0.815
25	standard	26906	1.544
26	blocked collima-tor	156	1.833
27	no sweep magnet	33357	1.922
28	half magnetic field strength	7787	1.629
31-48	dedicated halo detector runs	-	-
49	maximum B and 200 ns delay	1667	3.624
50	maximum B and no converter	76	1.686
51	max B and std converter	7681	0.551

Table 3.3. Run Summary

Run number	Remarks	PS (2-way) coincidences	Tagger channel sum ($x10^{11}$)
52	standard	12998	19254
53	tagger magnet to 90 MeV	4402	0.635
54	no converter	1315	0.868
55	thick converter	19254	1.081
56	up/down converter	2182	1.026

3.7 Raw Data

As mentioned in Section 3.4 a coincidence was desired between a recoiling electron striking the tagger focal plane and at least two charged particles hitting scintillation detectors on opposite sides of the pair spectrometer within a certain time interval. When this on-line condition was met a tagged photon energy was read from a look up table that had previously been prepared from the program "tageng" [Pywell, 1991]. The total energy detected in the PS was also calculated.

On-line acquisition consisted of recording total counts in all detectors along with their rates and reading registers, time-to-digital converters (TDCs), and analog-to-digital converters (ADCs) in order to increment the appropriate histograms on an event by event basis. Approximately 200 MB of data was written to disk (for over 60 runs) and copies were made and stored on tape for off-line analysis. At the beginning of every run, initialization of scalers occurred and at the end of a run the accumulation of specific scalers were stored and printed out. A typical printout of the scalers recorded for each run is shown in Figure 3.9. Definitions of the scalers follow:

- X-triggers- The number of PS hardware coincidences.
- accepted-triggers - The number of coincidences accepted by the tagger.
- interrupts - The number of coincidences accepted by the tagger and PS.
- real, beam, live time - The clock time, beam on time and acquisition time.
- tagger channel sum - The total hits in all channels (used for normalization).

```
Looker: Tagger status:
Looker: X - triggers:          38068.0
Looker: prescaled X - int.:    0.00000
Looker: fast clears:           0.00000
Looker: auto clears:           0.00000
Looker: accepted fast clears: 0.00000
Looker: accepted triggers:     31446.0
Looker: R - triggers:          0.00000
Looker: interrupts (total):    31012.0
Looker: real time [sec]:       1833.98
Looker: beam time [sec]:       1801.34
Looker: live time [sec]:       1786.85
Looker: tag_err_tagger_ctr:    0
Looker: tag_err_lucid_ctr:     1
Looker: Duty factor (inst.):  56.5823 +/- 0.153027
Looker: Duty factor (average):57.9861 +/- 0.000314012
Looker: Tagger channel sum:    1.54395e+11
Looker: Tagger eff. uncorr.:  2.00862e-05 %
Looker: Counter 0 total counts  3.13182e+06
Looker: Counter 1 total counts  1.67781e+06
Looker: Counter 2 total counts  1.72653e+06
Looker: Counter 3 total counts  4.00459e+06
Looker: Counter 4 total counts  4.36003e+06
Looker: Counter 5 total counts  4.91578e+06
Looker: Total halo counts are 2.99794e+07
Looker: total time of run is 1833.98
Looker: Tagger normalization is  8.41857e+07
Looker: average halo rate is 16346.7
Looker: Normalized halo rate is 19.4174
Looker: Average 0 detector rate is 1707.67
Looker: Normalized 0 detector rate is 2.02845
Looker: Average X-trigger rate is 20.7571
Looker: Normalized X-trigger rate is 0.0246563
Looker: number of events with 0 counters hit is 0
Looker: number of events with 1 counters hit is 0
Looker: number of events with 2 counters hit is 30865
Looker: number of events with 3 counters hit is 145
Looker: number of events with 4 counters hit is 3
Looker: number of events with 5 counters hit is 0
Looker: Total number of events is 31013.0
Looker: Same side 2-way coincidences are 0
Looker: Opposite side 2-way coincidences are 30865
Writer: End Run 25. FRI 3:55 PM.
```

Figure 3.9. Printout of scalers recorded after each run.

- total counts - For each detector the number of hits recorded.
- average counts - The total counts divided by the live time.
- normalized counts - The average counts divided by the tagger channel sum.

In addition to this the number of opposite side events with 1 to 6 counters hits was recorded. These were the scalers used in this analysis. Histograms were also incremented on-line. As an example the normalized (by the real time of run 9) X-triggers are given in Figure 3.10.

Figure 3.11 shows pulse_height histograms of the ADC spectra with the pedestals removed. Refer to the beginning of Chapter 4 for the cause of pedestals and compare Figure 3.11 to Figure 4.2. Peaks should be present in these spectra which indicate minimum ionizing particles, however, they were washed out in many cases due to the detectors being placed nearly edge-on to the analyzed electrons thus giving different path lengths and different deposited energies.

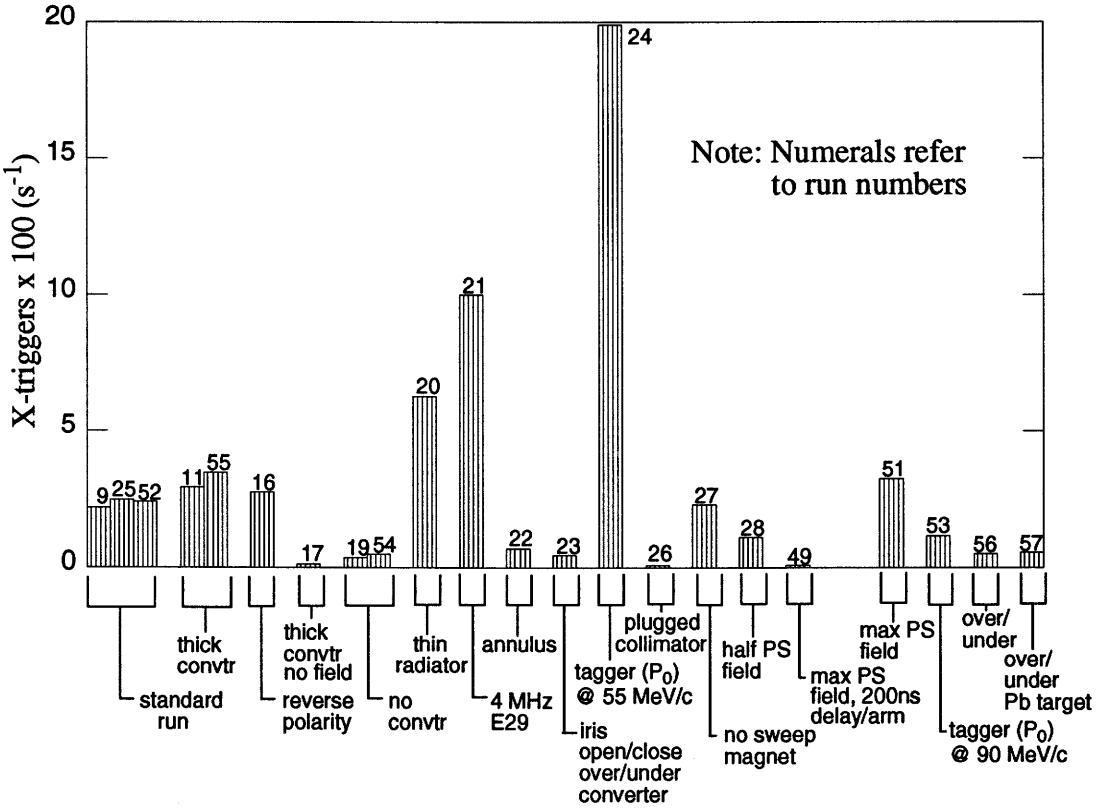

Figure 3.10. Histogram of normalized X-triggers.

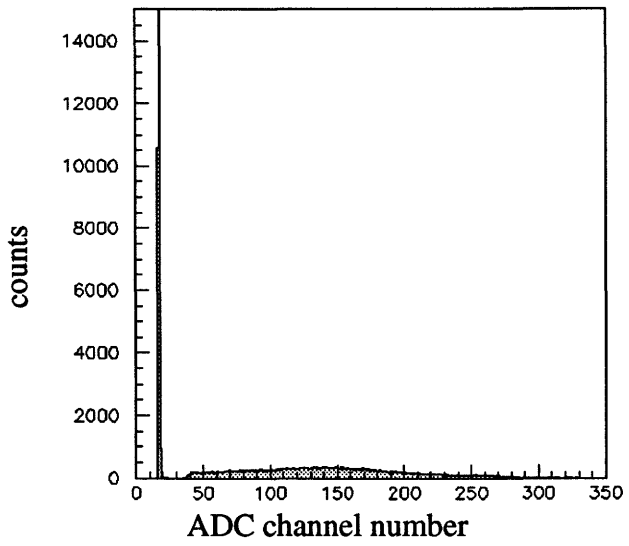

Figure 3.11. A single ADC histogram showing the pedestal and spectrum for one counter.

The TDC histograms for the 6 scintillation detectors (difference in time between any detector and tagger focal plane) were labelled *time_1* through *time_6*. Histograms of the relative timing difference between two opposite side detectors had nine possible combinations and were labelled *rtime*. These *rtime* histograms were constructed by subtracting the corresponding *time* histograms on an event by event basis. Finally there were tagger energy histograms generated when a coincidence took place between two opposite side detectors and a hit in the tagger focal plane.

Figure 3.12 shows a TDC histogram for a specific PS detector (the stop was given by the tagger and start by one of our detectors), a histogram of differences between two opposite side hits generated on an event by event basis and two uncut tagger energy histograms.

The shape of the raw tagger TDC spectra was characterized by a prompt peak and background (see Figure 3.4). The background should be a straight line meaning that accidentals are uncorrelated in time. Every time there was a hit in the tagger focal plane and a corresponding hit in the X-arm within a certain time interval (~40 ns) then a tagged photon event was triggered and the tagger TDC histograms were incremented. If three hits took place in the tagger focal plane during this time then 3 of 62 tagger TDC histograms were incremented.

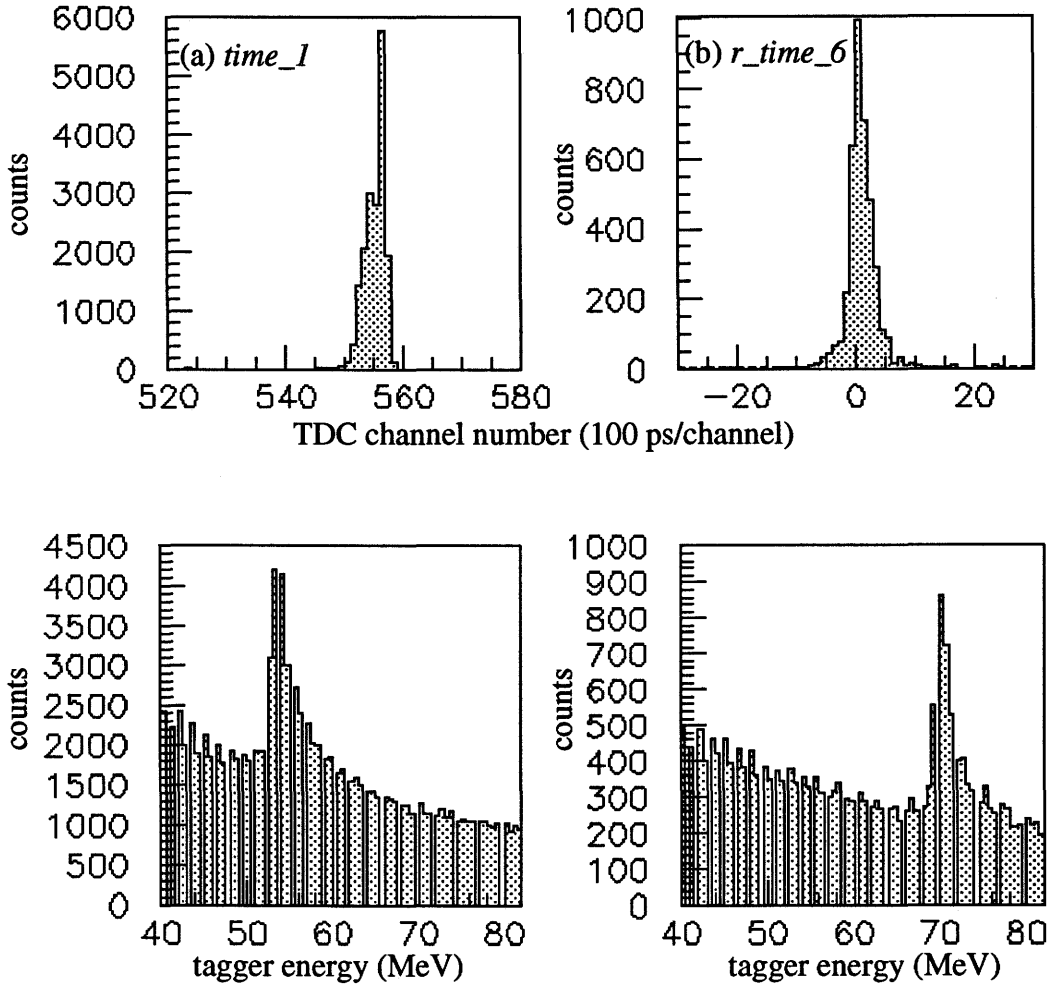

Tagger energy in 0.5 MeV bin widths

Figure 3.12. A tdc histogram of a PS detector (a), a relative timing histogram (b) and the tagger energy (c,d) for the nearest and farthest PS detectors.

3.8 Halo Detector

Figure 3.13 shows the count rate in the halo detector for various iris settings. It appears that the beam halo increases drastically when the iris begins to scrape the beam. A knee in the graph occurred at 9 - 10 mm corresponding to a similar beam diameter at the exit of the PS. Beam photographs at the exit of the yoke gave a horizontal size of about 6 mm and a vertical spread less than 8 mm. The diagonal of this beam spot photograph was about 9 mm in fair agreement with the knee of the graph. Recall that the beam was originally collimated by a 3x3 mm square hole and thus there was a poor shape match between the square collimated beam and the circular iris.

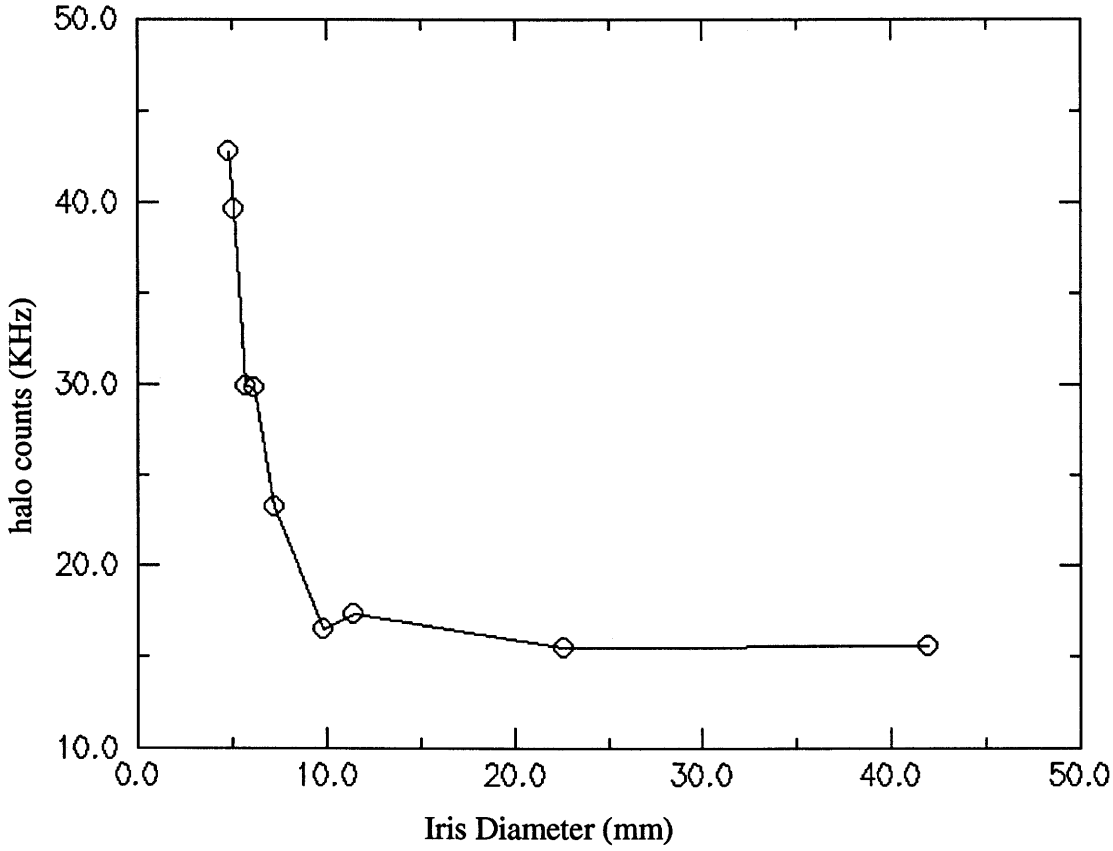

Figure 3.13. A plot of the beam halo as a function of iris opening.

Chapter 4. DATA ANALYSIS

As stated in Chapter 1, the purpose of this test was to calibrate the pair spectrometer as well as determine its energy resolution and to gain an understanding of the efficiency of the device. The primary objective of this chapter is to provide an explanation of the off-line analysis. Topics discussed include software cuts, kinematic constraints, corrected yield determination, normalizations, energy calibration, energy resolution, and efficiency of the pair spectrometer. This chapter ends with the relevant errors being explained and quantified.

4.1 Data Reduction

During the course of the test over 200 MB of data were collected and conveniently stored on a single 8 mm videotape. All the data were transferred to disk for easier off-line access. Once the data acquisition was completed three copies of the original tape were made and stored for safekeeping. For example, runs were grouped and classified as *standard* or *non-standard*. In the standard runs the device operated as a pair spectrometer but included runs with differing converter thickness or shape. The nonstandard included tests for backgrounds and were specified by indicating the difference from the standard configuration specified in Chapter 3, Section 6.

A systematic and iterative procedure was developed to filter and analyze the data. The procedure is described in the flowchart in Figure 4.1. Beginning at the top left corner of the flowchart and proceeding down the left hand column, the first box represents the raw data. This included on-line histograms and scaler readings and provided a starting point for data reduction. In the early stages of off-line analysis these histograms had software cuts placed on them to bring out certain conditions that were deemed significant and also for a first quick look at the performance of the PS. These cuts were relaxed as the analysis procedure was refined.

4.2 Removal of ADC pedestals

There was some work that was required before any software cuts could be applied. There were counts in the lowest active ADC channels that corresponds to that ADC not being hit during the event. In principle these should fill in only one channel of the ADC and give the zero offset which we call the "pedestal". In practice the effect of noise and dynamic baseline shifts in the ADC caused a gaussian response. The presence of the

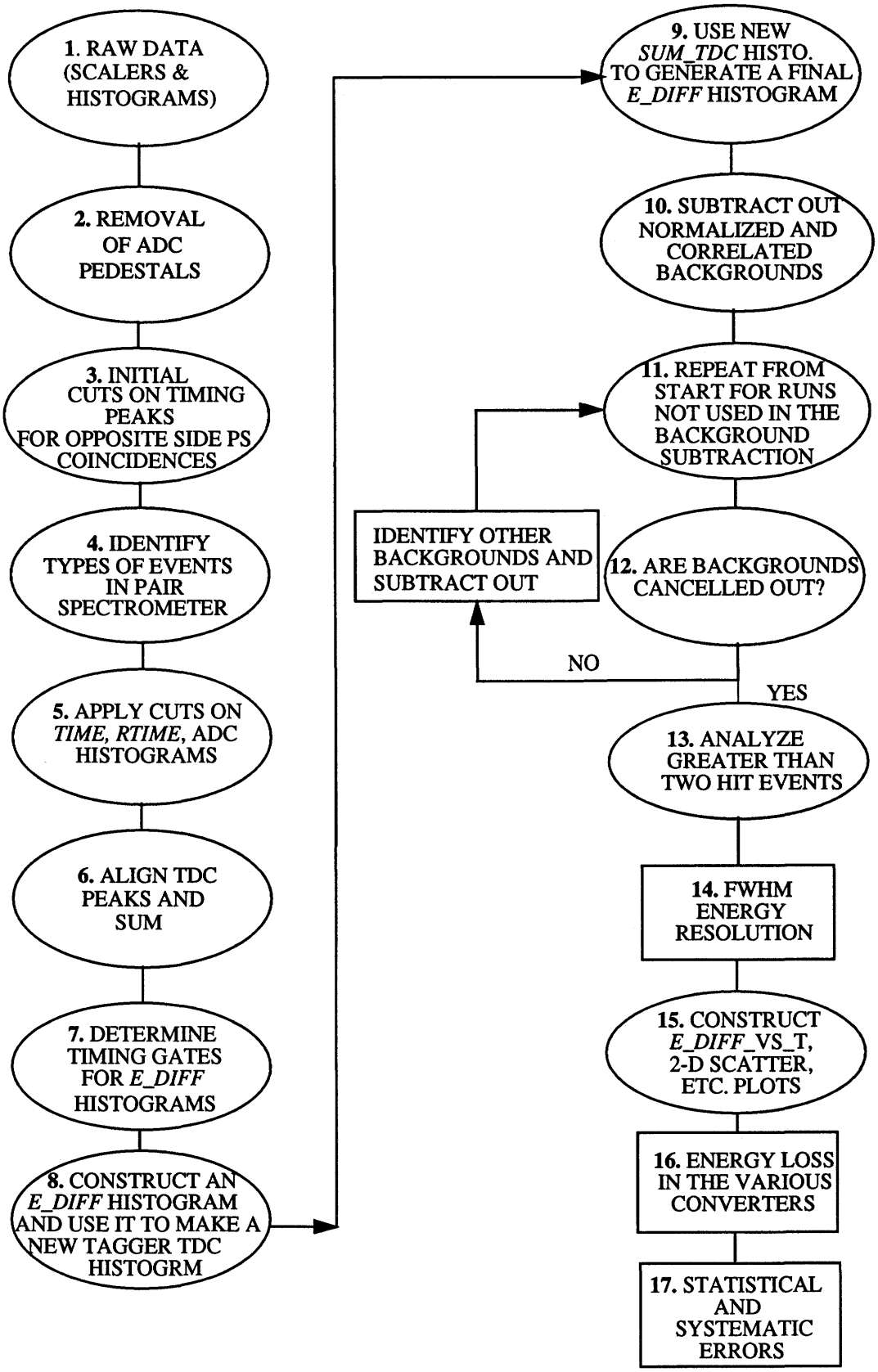

Figure 4.1. Flowchart of off-line analysis.

pedestals was removed by shifting the abscissa in the six ADC histograms. Shifting was determined by identifying the ADC channel with the largest number of counts and translating the remaining information by this amount. The pedestal corrected histograms are shown in Figure 4.2. The sharp rise at low pulse height was due to the hardware discriminator.

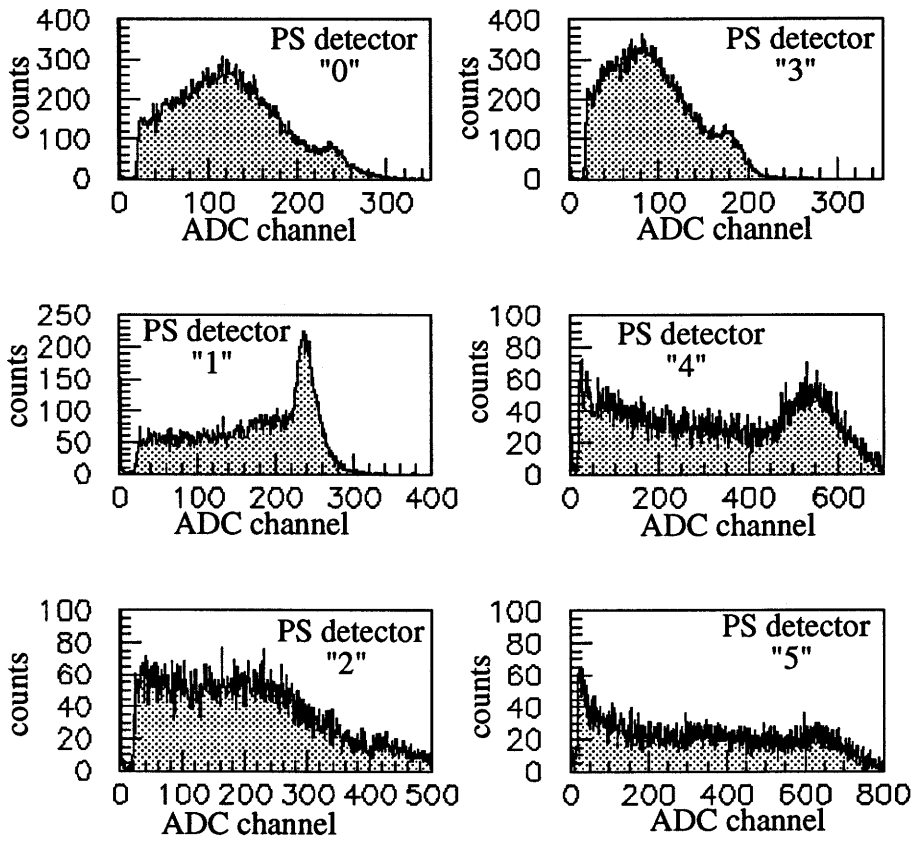

Figure 4.2. ADC pulse_height spectra with pedestals shifted.

4.3 Preliminary Cuts

The next step (oval #3), near the top left hand side in Figure 4.1, is labelled preliminary cuts on the tagger TDC prompt peaks. These peaks signified a constant time difference between the tagger and PS focal planes for valid events. Tight software cuts were initially placed on the tagger TDC prompt peaks for opposite PS side coincidences in order to get a quick analysis of our results. This allowed the on-line construction of tagger energy histograms (for each pair of opposite side detectors) which could be easily compared to the calculated energies determined from a knowledge of the magnetic field

and detector placement on the two PS focal planes (refer to Appendix B.1 for determination of energies in the PS). These tight tagger TDC cuts were later relaxed but retained for background subtraction.

4.4 Event Classification

The fourth step in Figure 4.1 refers to the classification of events in the test of the PS. Simple events were analyzed first (i.e. opposite side coincidences in the PS) and the more complicated (higher multiplicity) were reserved for later analysis. The valid X-trigger events included those where *more than one* counter fired on either side of the PS. Thus events were categorized and analyzed according to the number of counters hit in the PS in coincidence with a tagged photon event.

There were two types of PS events which should not be observed. These are zero or one hit events on the PS focal plane(s). This condition would have indicated a problem with the electronics and/or the logic used in computer code. In all instances there were no events of these types and reassured us that part of the hardware and software was working correctly.

The normal two hit events have already been described and are dealt with in detail. There were also three hit or greater events which were due to a valid two hit event either contaminated with random electrons arriving at the same time or from the initial pair produced in the converter suffering hard bremsstrahlung by one or both of the charged particles that allowed production of more pairs. Higher than four hit events were possible (due to a showering process) but none were observed. The reader may refer to Figure 3.9 for typical numbers of the types of events which did occur. The percentage of hits that were not simple opposite side coincidences in the PS was less than 0.5%.

4.5 Software Cuts

The fifth step in the flowchart was concerned with software timing cuts and initially the analysis was done exclusively on the two hit events. There were *time* histograms generated for each of the six PS detectors when at least two opposite side counters fired. The *time* histograms refer to the time delay between a hit in the tagger focal plane and a hit in one arm of the PS. Thus for a two hit event only two of the *time* histograms were incremented. Software cuts were placed tightly around the prompt peak ($\sim \pm 3\sigma$) on all six *time* histograms.

There are also 9 *r_time* histograms that were simply the difference in the *time* histograms corresponding to the two hit detectors in the PS generated on an event by event basis. The time difference between the two hit detectors should be a constant value and indeed these TDC spectra showed narrow peaks (see Figure 3.12.b). The full width half maximum of the peaks in the *r_time* histograms was always less than 1 ns (ten TDC channels). There were also software cuts placed on the nine *r_time* histograms in a similar manner to the *time* histograms. As expected with such narrow peaks the *r_time* cut did not reduce the data significantly.

At this stage pulse height threshold cuts could be put on the six ADC histograms for the PS detectors. However, as mentioned in Chapter 3, Section 7, the histograms were of poor quality so the wide software cuts had virtually no effect on the data reduction and for this reason the ADC cuts were removed in the final analysis leaving only the hardware cut due to the discriminator.

4.6 Tagger TDCs

As mentioned in Chapter 3, individual TDC histograms for each tagger channel were built for events that produced an X-Reference signal. This X-Ref was the common start for the tagger TDCs and the delayed stop was given by the specific tagger channel(s) that was struck. The most important spectra are these timings of pairs in the PS with respect to the electrons on the tagger focal plane. One of the 62 tagger TDC histograms has already been shown in Figure 3.4

The sixth step refers to the alignment and addition of the 62 tagger TDC histograms. Each tagger channel had a peak in a different place. Thus every channel has an offset associated with it to align all the peaks to a common point. The resulting histograms were then summed. This addition improves the statistics and allows a single software pass to be applied simultaneously to all channels. This summed and aligned histogram was used to determine timing gates between the tagger and experimental arm and this is the subject of the seventh oval.

Usually tagger TDC spectra would be obtained from a tagger efficiency run where a lead glass detector is used to absorb the tagged gamma rays and to produce clean, sharp spikes in each of the 62 timing histograms. A tagging efficiency run was not performed by our group and this was admittedly a mistake. The less sharply defined tagger TDC histogram (summed and offset) from the medium Cu foil runs were used for timing cuts.

The determination of the centroid peaks in the alignment procedure was easily done by eye since the peaks were sharp enough. This avoided the ambiguities which might have resulted from the use of computer code that usually requires a background having no slope and only a single primary peak. Equipped with the offsets the alignment and summing procedure was a simple off-line procedure. A new tagger timing histogram was incremented with the appropriate offset value (referenced to TDC channel number 1000). An improvement by a factor of three or four in the ratio of events inside the prompt peak to those outside from the resultant sum of the shifted 62 channel histograms was observed as compared to a single TDC spectrum. This may be seen by comparing Figures 3.4 and 4.3.

The sum of the offset tagger TDC peaks did not have a flat background as expected for random events and this is the reason for the eighth step in the analysis. Figure 4.3 shows a broad shoulder of X-triggered events that occurred at a later time (~ 5 ns) than events inside the prompt peak. This suggested that another process had taken place. Note that the time difference is larger for smaller TDC channels because the start for the tagger TDCs was given by the X-trigger and the stop by the delayed hit in one of the tagger focal plane detectors. The choice of the initial gate is explained in Section 4.7.

4.6.1 Multiple and Random hits

If a pair was detected in the X-arm electronics which triggered the tagger electronics then the hit pattern of the tagger focal plane was recorded. The tagger time window had a finite width (~ 40 ns) so there was a chance that more than one hit occurred in the tagger focal plane within this period. For the event in the PS, one of the hits in the tagger corresponded to the tagged photon which converted and was detected by the PS, while the others were random hits. The instantaneous rate of more than one hit in the same tagger

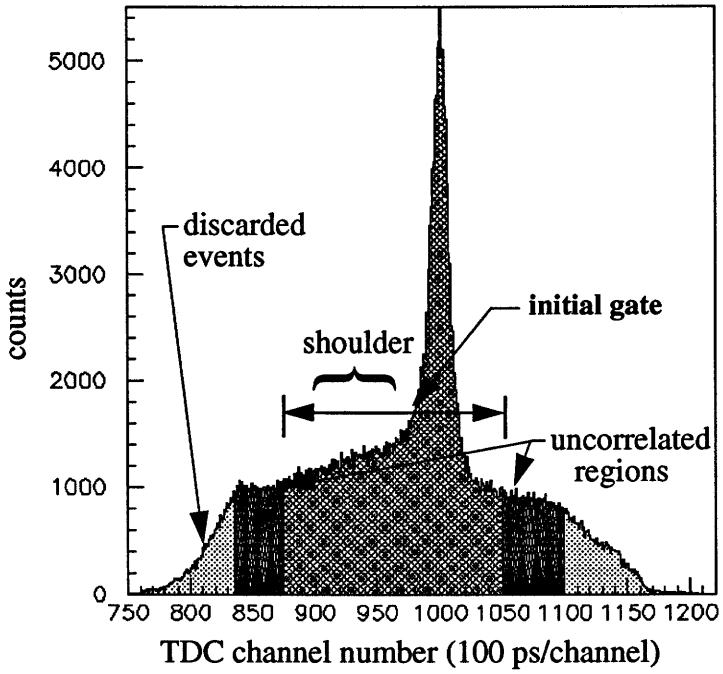

Figure 4.3. The software sum of 62 aligned tagger channels.

channel was ~ 4%. Of course the rate of multiple hits over the entire focal plane is much greater. See Figure 4.4.a. It is believed that these random events would be corrected for (on the average) by the subtraction of the uncorrelated events from the correlated events.

If the random electron arrived (in the same tagger channel) before the correlated one then the TDC stops prematurely. The smaller TDC value resulted and the event would fall in front of the prompt peak. This yields less correlated events in the timing peak. Thus it is expected that the tagger TDCs would have a background that is a straight line (since it was caused by random coincidences) but with a negative slope to account for these stolen coincidences. There is a correction factor for this effect that may be applied to each tagger channel on an individual basis [Vogt, 1992] and is much less than1%. This approach was not used here because this correction is most important when cross sections are to be extracted but was not required for the PS test. Further the shape of the background in Figure 4.3 (from smaller to larger TDC channels) appears flat then begins rising to the shoulder and then starts to fall in a linear fashion as predicted by the effect of stolen coincidences. This correction has no effect on the determination of the energy resolution and a negligible effect on the efficiency of the instrument.

4.7 Timing Gates for Energy difference histograms

Once the tagger TDCs were aligned and summed, the initial timing gate was determined. The subject of the seventh step in the flowchart is the placement of gates for the correlated region. The reduction in multiple hits in the tagger focal plane for events lying within the initial gate of Figure 4.3 with the previously discussed software cuts implemented (step 5) is shown in Figure 4.4.b. The events residing in the zero bin of multiple hits corresponds to events that did not pass the timing cut criterion. For comparison purposes the number of multiple hits for all X-triggers in the PS is shown as well in Figure 4.4.a.

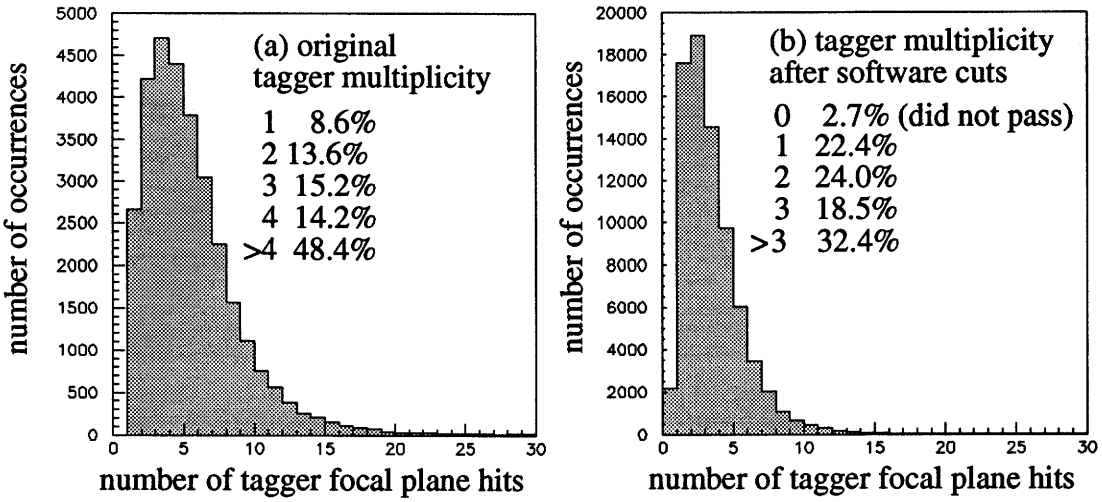

Figure 4.4. Multiple hits in the tagger focal plane.

To properly implement the subtracting of uncorrelated events requires a flat background or at least an understanding of the background processes. This fact is the reason why a second generation *e_diff* histogram was generated. More will said on this in the next section.

4.8 Energy Difference histograms

For three detectors on each side of the PS, there exist nine opposite side pairs and hence nine nominal photon energies. These energies are listed for a particular field setting in Appendix B.1, Table B.2. An energy difference (PS energy - tagger energy) was binned

in one of nine *e_diff* histograms if the tagger TDC was within the initial gate shown in Figure 4.3 according to which combination of opposite side detectors (in the PS) were struck.

All nine *e_diff* histograms are shown in Figure 4.5 for a standard run after the timing software cuts previously described had been implemented using the initial gate from Figure 4.3. The numbering system for these histograms begins with detector 0 and 3 and continues with 0 and 4 and so on. The individual numbers of each *e_diff* histogram are shown in parentheses and the detectors used are given to the right of this in Figure 4.5. Note that all the *e_diff* peaks are centered at or near an energy difference of zero which is very satisfying since the PS energy should match that given by the tagger. For comparison the scaled backgrounds from the uncorrelated regions are also shown as the darker region under the curve. The method of scaling the backgrounds is discussed under the background subtraction section.

Note that the *e_diff* spectra are not gaussian in appearance. The left hand side of these histograms had a broad shoulder which rises to the peak height in these histograms. Events that appeared on the left side of the *e_diff* histograms corresponded to the case where the tagged photon energy was greater than that detected by the PS. The baseline on the right hand side had a shoulder, too, that was higher than that on the left side. These effects are discussed with emphasis on their shape in Chapter 5.

NOTE: All histograms have a bin width of 0.5 MeV.

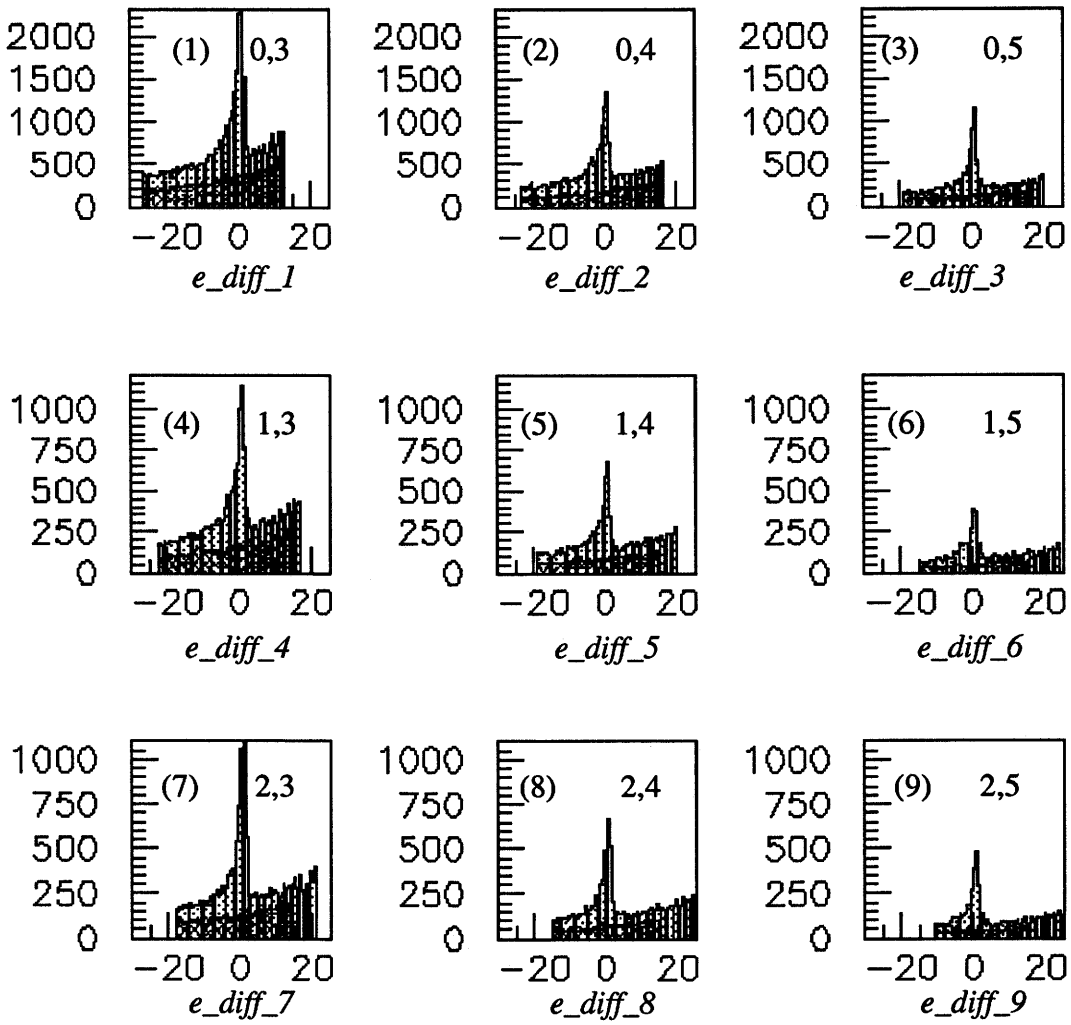

Figure 4.5. The first generation *e_diff* histograms.

4.8.1 Second generation Tagger TDC and *e_diff* histograms

Returning to Figure 4.1, the ninth step (at the top of the second column) is concerned with building the final *e_diff* histograms. Software cuts between [$-15 \leq e\_diff \geq 10$] MeV were placed on this energy histogram which allowed generation of a second summed and offset tagger TDC histogram. This *new* TDC spectrum then had software limits placed on the peak position and on part of the uncorrelated region allowing a *new* set of *e_diff* (correlated and background) histograms to be generated. It was these second generation *e_diff* histograms that aided the determination of the energy resolution of the PS.

The justification for this ninth step was that the second set of tagger TDC histograms had a flat background and supported the claim that the shoulder in the original tagger TDC spectra was to due to purely random events which did not pass the kinematic test. The second generation tagger TDC histogram and the reduction of multiple hits in the tagger focal plane due to the events inside this prompt peak are shown in Figure 4.6. The zero bin in Figure 4.6.b indicates events that did not pass the software cuts but are displayed in this channel to conserve the area.

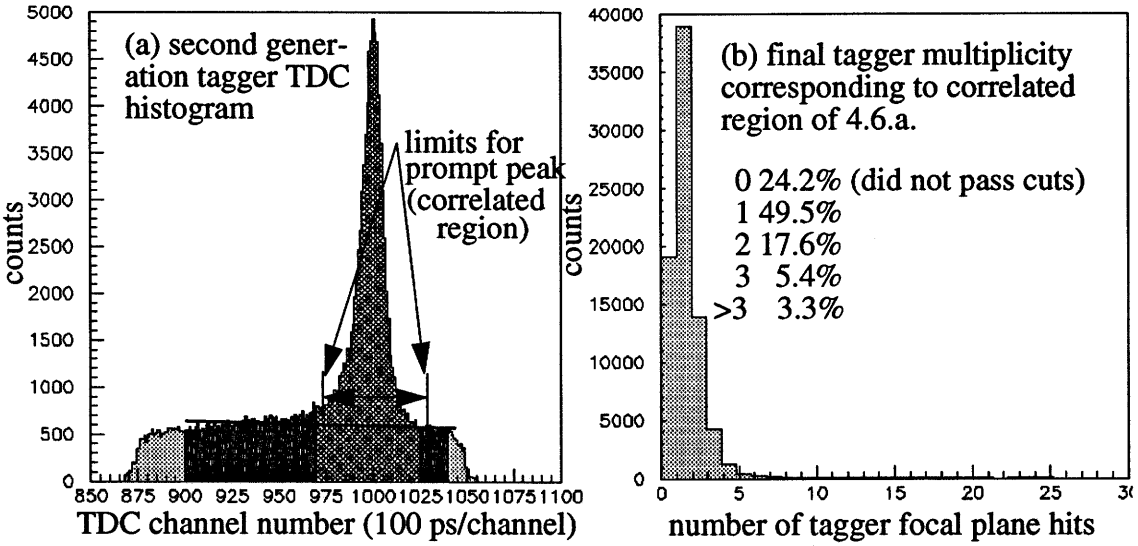

Figure 4.6. Final tagger TDC histogram and tagger multiplicity.

4.9 Background Subtraction

Once the second set of *e_diff* histograms was generated the tenth step of the data analysis consisted of subtracting the background events. The method of determining the actual correlated yield (for the standard conditions but different converters) consisted of two steps. The first part removes the uncorrelated events from each individual run or group of runs (this is shown in Figure 4.7 for the standard configuration). The second part of this tenth step consisted of subtracting correlated events caused by other processes (i.e. conversion due to air, etc.) that were correlated in time with hits in the tagger focal plane. The runs that determined the correlated backgrounds had to be normalized by the total tagger channel sum in order to be subtracted from the standard configuration runs.

4.9.1 Standard Conditions

Subtracting uncorrelated events is not a trivial problem since care must be taken not to subtract too much and remove valid events or to subtract too little leaving unknown backgrounds still present. Again, the purpose of background subtraction is to obtain the number of true correlated events within the PS such that useful quantities can be examined. The main quantities of interest are energy resolution and efficiency of the device. When this instrument is used to study the photon splitting reaction these parameters are necessary to extract cross sections.

Limits ($\sim \pm 3\sigma$) on the tagger TDC prompt peak were chosen as shown in Figure 4.6.a. Inside this region, which we refer to as the foreground, there are correlated events and uncorrelated events. A corresponding cut was made on the portion of the spectrum where only uncorrelated events were located. As mentioned, the linear background was necessary to verify that these events were truly random. It is always desirable to make the background cut region as large as possible, to have enough statistics on background events.

Two sets of *e_diff* histograms were generated (one for the correlated region of the TDC spectrum and the other for the uncorrelated regions) and it was a simple matter to subtract these two sets of histograms with the appropriate scaling factor. The scaling factor was the ratio of the widths (in the second tagger TDC histograms) of the foreground region to the sum of the widths of the two background regions and was denoted by K. Equation 4.1 relates the true correlated yield, N_{corr} to the foreground, N_{fore} and background, N_{back} yields.

$$N_{corr} = N_{fore} - K \cdot N_{back} \tag{4.1}$$

The standard configuration (medium square converter), second generation (for studying the energy resolution) *e_diff_1* histogram is shown with the foreground events and the scaled background events in Figure 4.7(a). The histogram that results after subtracting the uncorrelated region is shown in Figure 4.7(b). Note that backgrounds still persist on the right side of *e_diff* spectra shown in Figure 4.7.b and this precipitates the second part of the tenth step in the analysis: removal of the correlated background processes. This method is given in the next section once a description of the features of the nonstandard runs is presented.

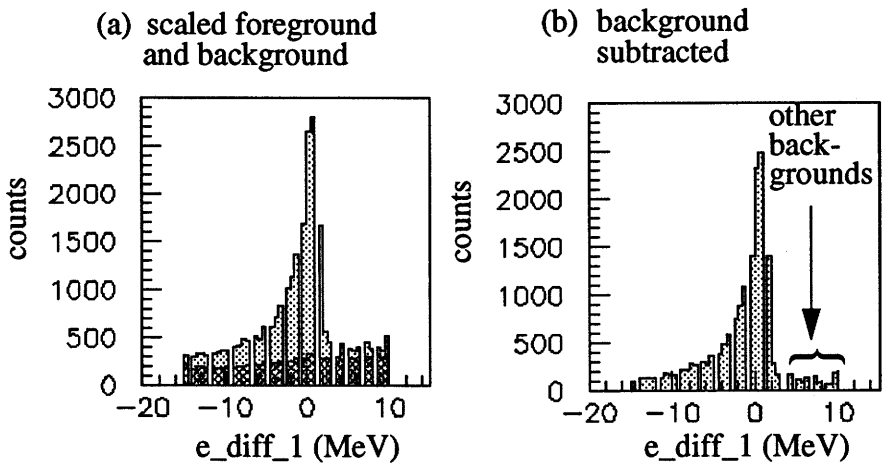

Figure 4.7. Subtraction of the uncorrelated events in the *e_diff(1)* histogram for the standard run

4.9.2 NonStandard Conditions

Nonstandard runs had one or two of the parameters from the standard configuration altered and some were required for the correlated background subtraction (the tenth step of the data analysis in Figure 4.1). From the effects of each nonstandard condition, conclusions were made concerning the behavior of the PS. The order of discussion of these runs proceeds from the simplest setup and progresses to the more complicated cases. It will be useful to refer to the histogram of normalized X-triggers given (for the most important runs) in Figure 3.10.

The simplest nonstandard run was with no tagger radiator in place (# 12) and this allowed the undisturbed electron beam to continue into the beam dump. This condition corresponded to few electrons in the tagger focal plane and even fewer X-triggers. There was a small X-trigger rate that was about 2% of the standard run and was attributed to accidentals caused by the electron beam. Thus even without the presence of tagged photons there is a detectable coincidence rate due to the electron beam alone.

The tagger radiator #7 (115 μm) was added and the collimator was plugged (run 26) to virtually stop the photon beam. This situation gave the normal number of counts in the tagger focal plane but no tagged photons hit the converter. The purpose here was to get an indication of room background. The normalized X-trigger rate was less than 5% of the

standard run and implied that room background had a minimal effect on the number of X-triggers in the standard runs. The *e_diff* spectra did not show the characteristic structure and are not presented here.

The next run to be considered was with the PS magnetic field turned off (run 17) and the thickest converter in place. The X-trigger rate was 50% greater than with the collimator plugged but only 5% of the standard. Again the *e_diff* spectra appeared to have no structure. However, the number of counts seen in the halo detector (with maximal iris setting) was seven times greater than the standard configuration. More charged particles were accepted by this annular detector (as expected) since no magnetic field was present to deflect them.

The conversion due to air (run 19) was easily studied by removing the converter and leaving everything else unchanged with respect to a standard run. The normalized X-trigger rate was 17% of the standard run and is partly due to the low density of air relative to copper. The *e_diff_1* histogram is shown for this case in Figure 4.8.a once the uncorrelated events have been subtracted. Note that there is no broad tail (on the left side of this histogram) that signifies energy loss. It was this run that was used to account for background correlated yields for the standard runs.

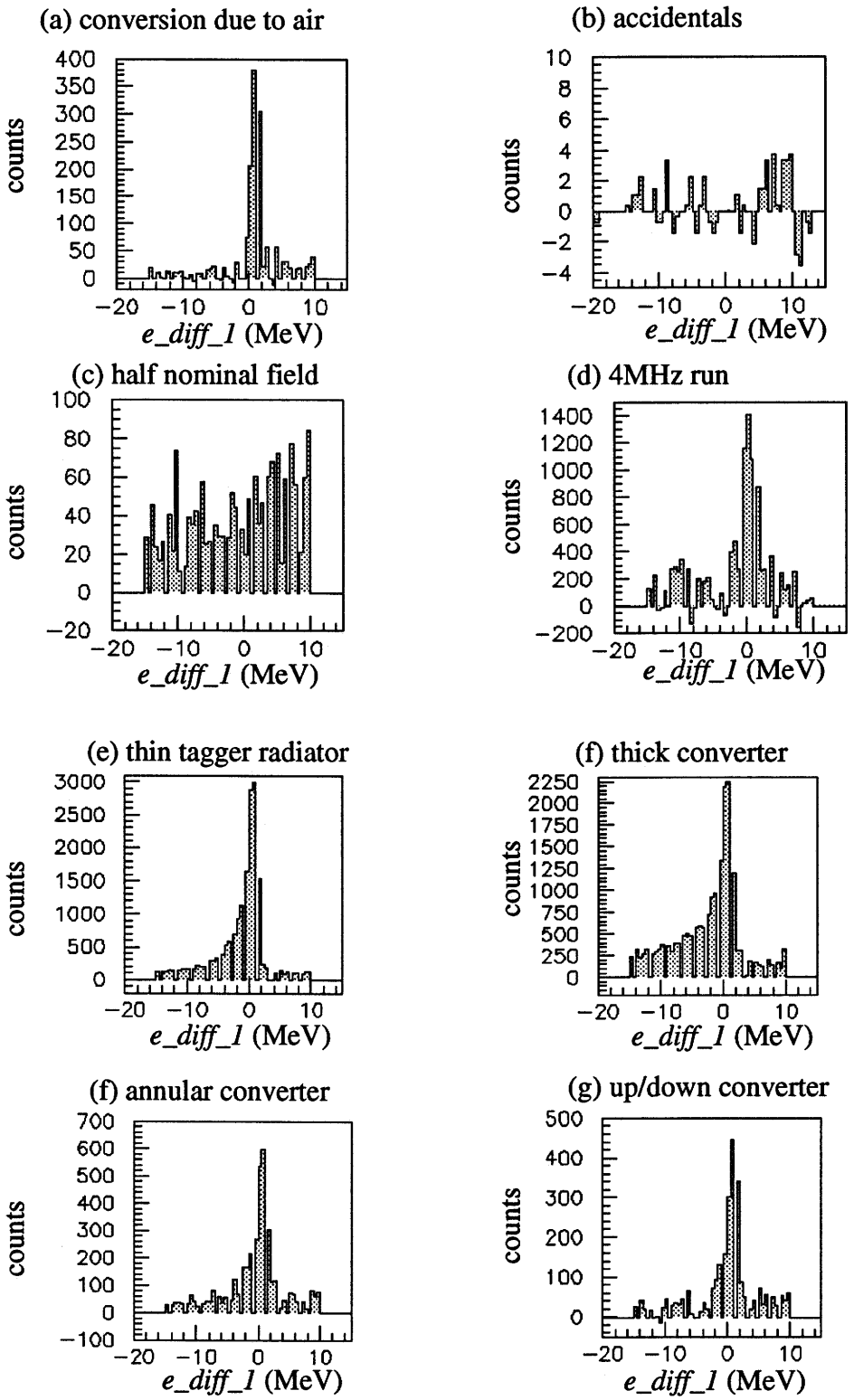

Figure 4.8. Uncorrelated events subtracted and tagger channel sum normalized *e_diff* spectra for selected runs.

One run was done with the signals from one arm of the PS delayed by 200 ns (run 49) and this ensured only accidental coincidences. There was a X-trigger rate which was of the same order of magnitude as the plugged collimator rate. The normalized and uncorrelated subtracted *e_diff* spectra is shown in Figure 4.8.b, no peak is seen.

When the tagger count rate (indexed by tagger channel 29) was increased by a factor of 4 to 4MHz (run 21) the X-trigger rate rose by 400% relative to the standard configuration. This appears realistic since one expects the trigger rate to rise linearly, however, the background rate rises as the square to give a factor of 16. The summed tagger TDC histograms are shown for this run, before and after software cuts, to illustrate their poor quality in Figure 4.9. The tail that described the energy loss in the converter is seen in Figure 4.8.d. At first sight it may be argued that the efficiency is lower at this higher rate but the reason is due to improper background subtraction. The background can not be subtracted in the manner stated earlier since the summed timing histogram did not have a flat background region (even after software cuts) and there was no well defined prompt peak. On this basis all that can be said is that the PS cannot accept these higher count rates. Further testing is needed to determine the maximum count rate that can be safely processed by the PS.

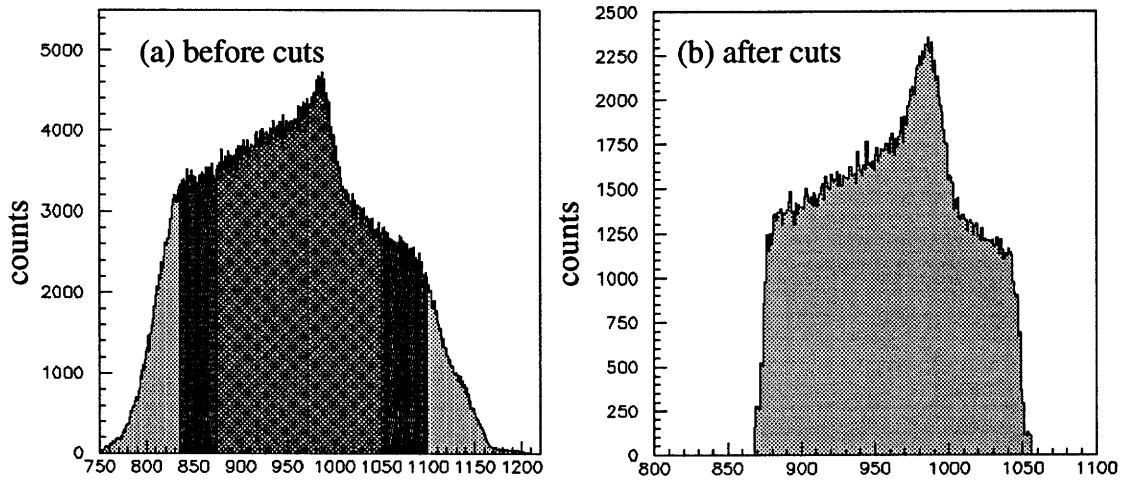

Figure 4.9. Before (a) and after (b) summed tagger TDC histograms for the 4MHz run.

A thin tagger radiator (12 μm Al) was inserted (run 20), with everything else unchanged from the standard configuration, and the normalized X-trigger rate was 2.5 times greater than the standard run, medium converter. Under these conditions a greater fraction of the photon beam was able to pass through the small collimator since there was less multiple scattering of the electrons in the tagger radiator. Once the uncorrelated background events were removed it was observed (Figure 4.8.e) that the peak in the *e_diff* histogram was ~ 20% higher than that seen in Figure 4.7 for the standard configuration. This thin radiator minimized multiple scattering of the electron beam within the radiator.

Insertion of the annular converter (run 22), again the only difference from the standard configuration, resulted in a normalized X-trigger rate about one third of the standard run. Recall that there was not a good geometrical match since the tagged photon beam passed through a square collimator prior to the converter. The reasons for choosing this geometry for the converter are apparent when one considers the photon splitting experiment and the detection of photons at small angles relative to the primary photon beam. If it is assumed that a point electron beam spot was incident on the radiator then the width of the beam at the converter should be less than 4.5 mm. The inner annulus of the converter had a diameter of 7 mm thus only photons that were 3.5 mm off axis were converted. The *e_diff* spectra is shown in Figure 4.8.f once the uncorrelated events had been subtracted.

A run was done with an up/down type of converter which was designed to let the primary beam pass through similar to the annular converter. The X-trigger rates should be smaller than for the annular converter since only vertically diverging photons were converted. This was found to be the case as the X-trigger rate was about 25% lower than that using the annular foil.

The polarity of the dipole (run 16) in the PS was reversed to study any asymmetry that may exist. We expected no difference and this was verified with count rates almost identical to the standard run. The PS dipole can have either polarity and more importantly the location of the beam dump had no noticeable effect on the PS when electrons or positrons were being accepted in the PS arm that was on the same side as the dump.

The tagger central momentum was set to 55 MeV in run 24 (as opposed to ~75 MeV for the standard run) to move the primary beam out of the beam dump and to let it hit the wall of the experimental hall. The X-trigger rate rose a dramatic 130 times the standard rate, however, the *e_diff* spectrum had no discernible peak at 0 MeV. The conclusion is that the PS detectors recorded charged particles from the beam striking the wall.

Run 28 was performed with the PS magnetic field at half the value of the standard runs. In this situation there should be no real events and all events detected will be randoms or backgrounds. This run was normalized and used to subtract uncorrelated backgrounds explicitly along with conversion due to air. Accidental coincidences were subtracted out implicitly for each run by subtracting a scaled portion of uncorrelated events.

Once the correlated backgrounds were subtracted then the process had to be repeated for the nonstandard runs. The eleventh step in Figure 4.1 relates this method. This was not a difficult procedure since it had already performed for the standard configurations but it was time consuming.

4.10 Validity of Background Subtraction

Firstly it should be mentioned that all of our runs appeared to be reproducible. Most runs were repeated once and some runs were performed three times at different stages during the test. This reaffirmed our confidence in the experimental setup.

A consistency check was made on the final *e_diff* histograms as referred to in the twelfth step of Figure 4.1. The criterion was that an average background on the right hand side of the *e_diff* histograms would be zero. This side was chosen because the effects resulting from the unknown energy loss in the converter are present only on the left portion of the *e_diff* histograms. In almost all cases the average background on the right of the prompt peak in the second generation *e_diff* spectra was indeed zero within experimental error.

The main exception to the zero background condition were the thickest converter runs. The highest energy losses of the charged pairs occurred in this converter and a nonzero background persisted after normalization to the same tagger channel sum as the medium converter. It appears that the introduction of a thicker converter gave rise to more

side reactions that cannot be accounted for by simply scaling the tagger channel sum to the medium converter. These secondary reactions that simulate charged pairs being detected by the PS increase in a nonlinear manner (∝ thickness squared) whereas the first pair production is proportional to the thickness of the converter.

Additionally a run with the medium converter but without the sweep magnet gave a nonzero background. This may be partly attributed to photons that interacted prior to the sweep magnet to produce charged particles which were accepted by the pair spectrometer at the same time as one or two charged particles from a valid tagged photon event. Some of these uncorrelated charged particles were of higher energy since they appeared on the right hand ($E_{ps} > E_{tag}$) side of the *e_diff* spectra.

It was apparent that the sweep magnet bent charged particles out of the photon beam since the run with no sweep magnet (run 27) had a peak that was ~4% higher than that with the sweep magnet. Thus it is assumed that less than 5% of the events seen in the PS were caused by charged particles produced upstream of the converter when no sweep magnet was in place (see Figure 4.12.f).

4.11 Greater than two hit events

The thirteenth step in the data analysis is the three hit events in the PS, these only constituted 0.5% of all events. Nevertheless they were analyzed based on the same criteria as two hit events (i.e. by using the difference in energy between the PS and tagger).

It is believed that multi-hit events were caused by a valid tagged photon event where one photon of the produced pair which was accepted by the PS and the other hit(s) was the result of room backgrounds. Recall that the X-trigger was composed of charged pairs hitting the PS in coincidence with tagged photons. Therefore the chances of 3 hits within the timing window (~45 ns) of the PS being caused by all accidentals is negligible.

Even the three hit coincidences where a real pair due to a tagged photon and the third charged particle due to a random hit was accepted by the PS had an estimated count rate that was slightly larger than one every 1000 seconds. This was obtained from Equation 4.2 where $\dot{N}_{AB}$ is the counting rate for valid two hit events (20 s^{-1}) and $\dot{N}_C$ is the singles rate for a particular detector (~ 1800 s^{-1}) in one arm of the PS focal plane and τ is the coin-

cidence resolving time. However, the rate of three way hits in the PS was about two orders of magnitude greater than this so there are other factors which have not been accounted for.

$$\dot{N}_{ABC} = \dot{N}_{AB}\dot{N}_{C}\tau \tag{4.2}$$

The lego plot for three hit events in the PS is given in Figure 4.10 and indicates that all events took place at a tagged photon energy between 78 and 79 MeV. This fact can not be easily explained.

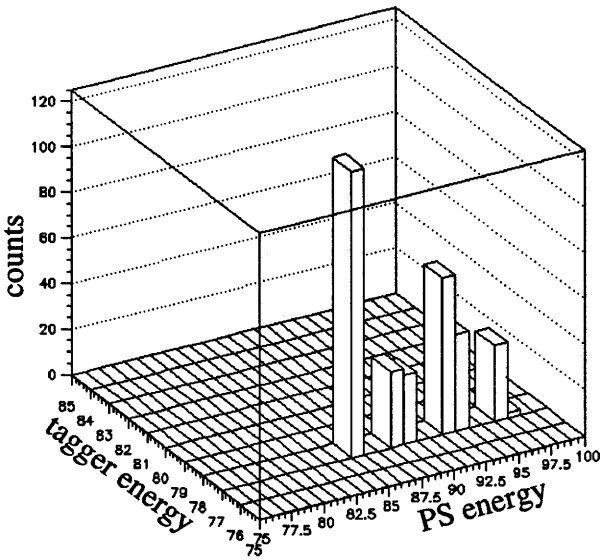

Figure 4.10. The tagger energy for 3 hit events in the pair spectrometer.

4.12 Energy Resolution of the PS

The fourteenth step in the flowchart was concerned with the energy resolution of the PS. Some care must be taken in interpreting the FWHM of the *e_diff* spectra as the energy resolution of the PS. To clarify this, Figure 4.11 illustrates how the *e_diff* histograms were filled by tracing the energy difference from tagger channel 41 to tagger channel 47 for the nearest set of PS detectors (using the standard configuration).

Note that all spikes have their yields background corrected and normalized. In Figure 4.11.h the results of the parts (a) through (g) are given and this allows comparison to Figure 4.12.a, the total number of hits accepted by the PS for the standard converter foil. The slight discrepancy (in height) was caused by multiple hits in the tagger focal plane.

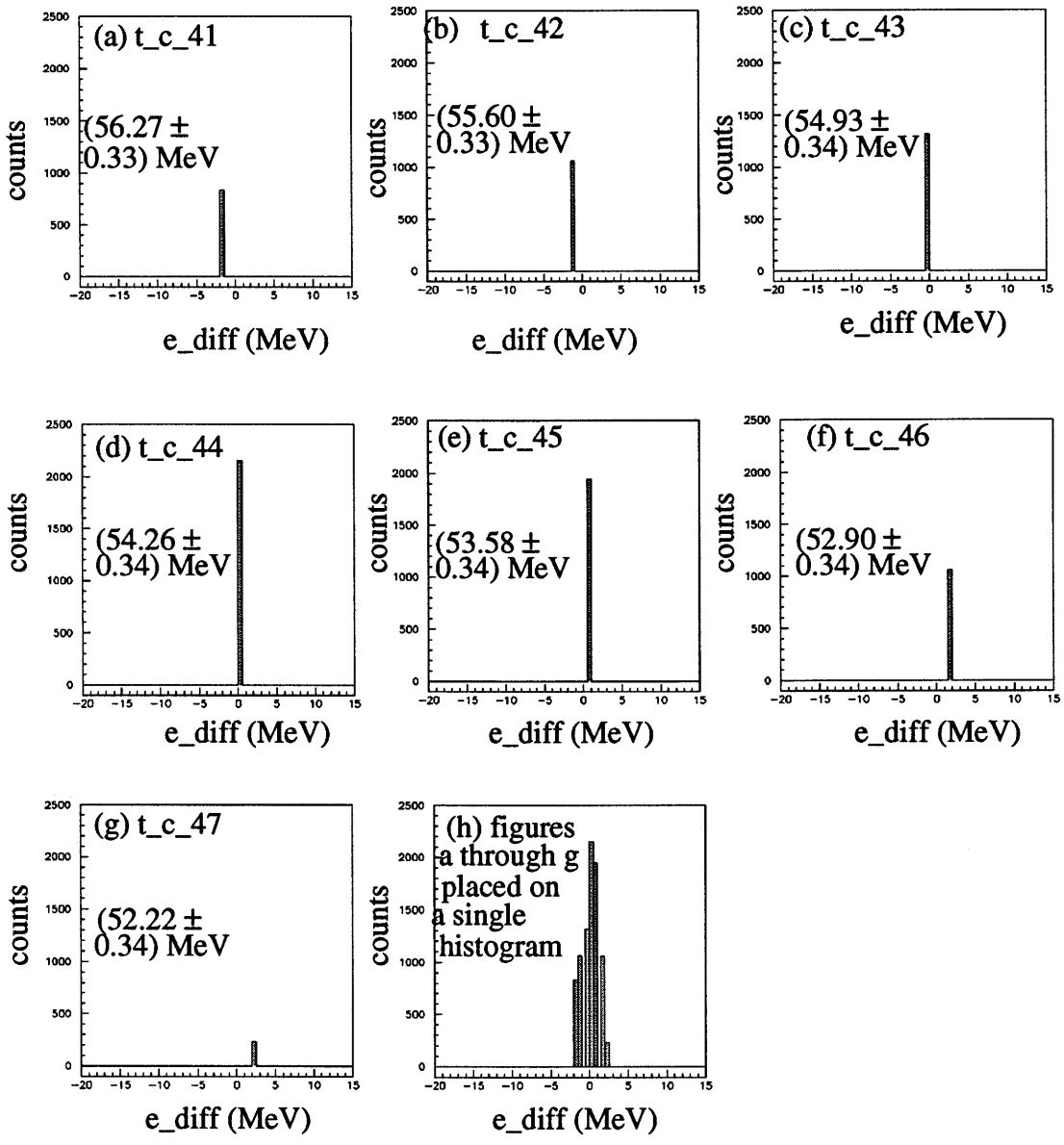

Figure 4.11. The *e_diff* spectrum for several tagger channels and their superposition.

Final results for several test conditions are given in Figure 4.12 and have been background corrected and scaled to the same number of hits in the tagger focal plane as the standard converter. The FWHM energy of the spectra shown in Figure 4.12 was 1.5 MeV for the three square converters and are labelled a, b, c. The thinnest converter foil had the same number of counts in the prompt peak but the thickest converter had a peak height that was ~ 10% lower than the other two. This can easily be understood when the effects

of multiple scattering are considered. Even though the thicker foil (for a given material) produces more pair production most of these pairs are scattered out of the acceptance of the PS.

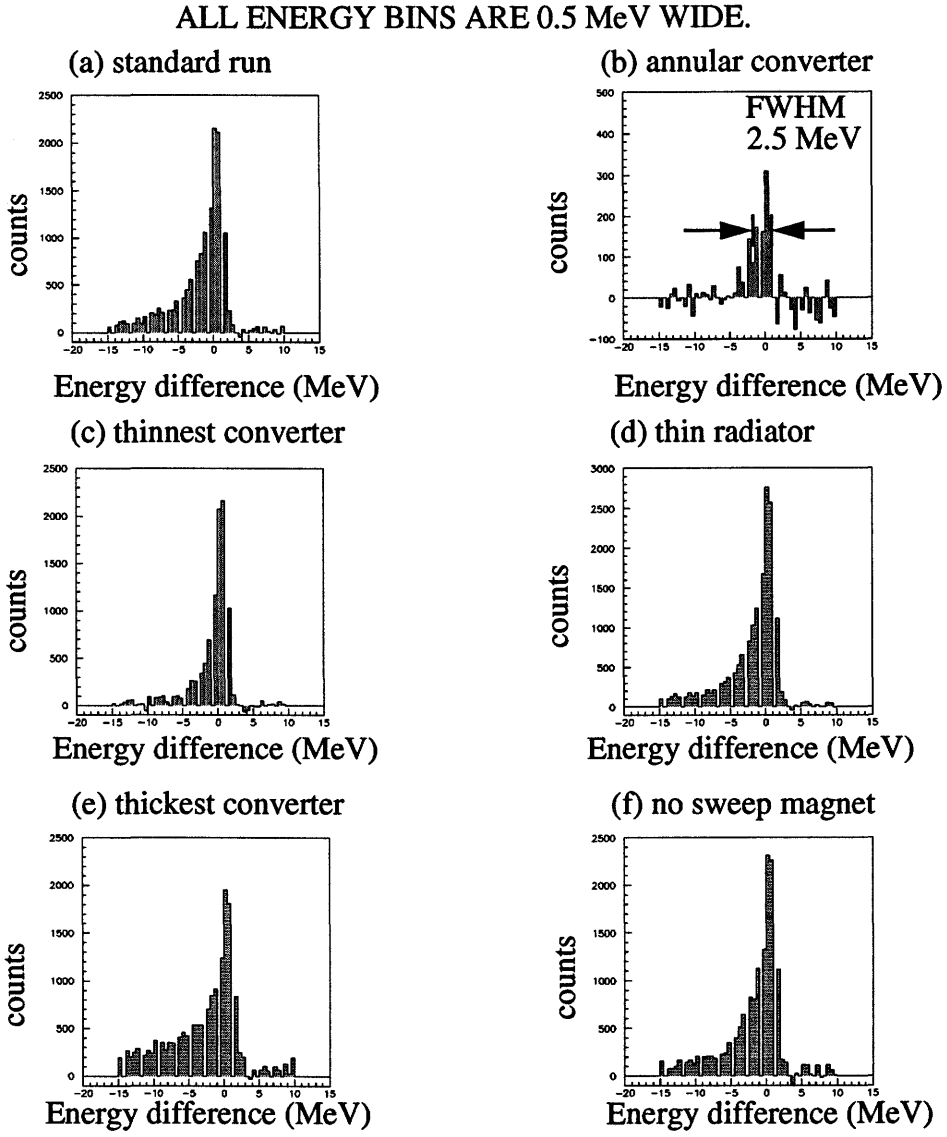

Figure 4.12. Normalized yields (to standard run) from second generation *e_diff* spectra.

The annular converter had a FWHM of 2.5 MeV and the energy spectrum is shown in Figure 4.12.b. This converter gave satisfactory results but at greatly depressed count rates despite normalization to the tagger channel sum of the standard run. The over/under converter (runs 23, 56) had less than satisfactory performance and a central peak that was difficult to identify. The air gap in the over/under converter was too large. Vertically off-

axis photons converted and subsequently they multiple scattered (in the converter) reducing the acceptance of the system. This is true to a lesser extent for the annular converter. Recall that the vertical angular acceptance for the PS was about ±40 mr.

Figure 4.12.d reveals that the thin tagger radiator #3 (12 μm) gave the highest normalized yield as expected. Thus there is justification for this thin radiator to be employed in future uses of the PS, despite its thinness.

4.12.1 Contour, Lego Plots

The presentation of results relating to the performance of the PS is now given according to the fifteenth step in the flowchart. A contour plot of the tagged photon energy versus the corresponding energy of the PS was constructed for the standard run after the second generation *e_diff* histograms were produced. The result is in Figure 4.13.a and a straight line fit was applied having a slope of 1.08 ± 0.03 ($\chi^2 = 0.87$) between 50 and 70 MeV. There are data at only five energies rather than nine since the symmetry of placement of the detectors caused four of the energies to be degenerate. Following the numbering convention used in Section 4.8, Figure 4.5 the first degeneracy is between *e_diff* spectra 2 and 4 while the second degeneracy results from detectors that formed *e_diff* spectra 3 and 5. The others are indicated in Appendix B, Table B.2. A line is drawn to guide the eye for the case of the tagger energy equal to the pair spectrometer energy.

In Figure 4.13.b a three dimensional plot was made corresponding to the contour plot and gives another representation of the excellent agreement obtained between the pair spectrometer and tagged photon energy.

The five distinct bands are also shown in Figure 4.11.a and denote the energy difference between the PS and tagger for events inside the second generation tagger TDC (where $-15 \leq e\_diff \geq 10$ MeV) prompt peak of Figure 4.6.

There were fewer events having an *e_diff* greater than zero since these were caused by multiple hits in the tagger focal plane (or room backgrounds) that had one photon which was accepted by the PS which had a higher energy than the registered tagged photon that did not get accepted. In the bottom half of Figure 4.11.a there is energy loss in the converter after the creation of a pair that is always present and hence more counts appeared here. The lego plot of the same situation is given in Figure 4.11.b.

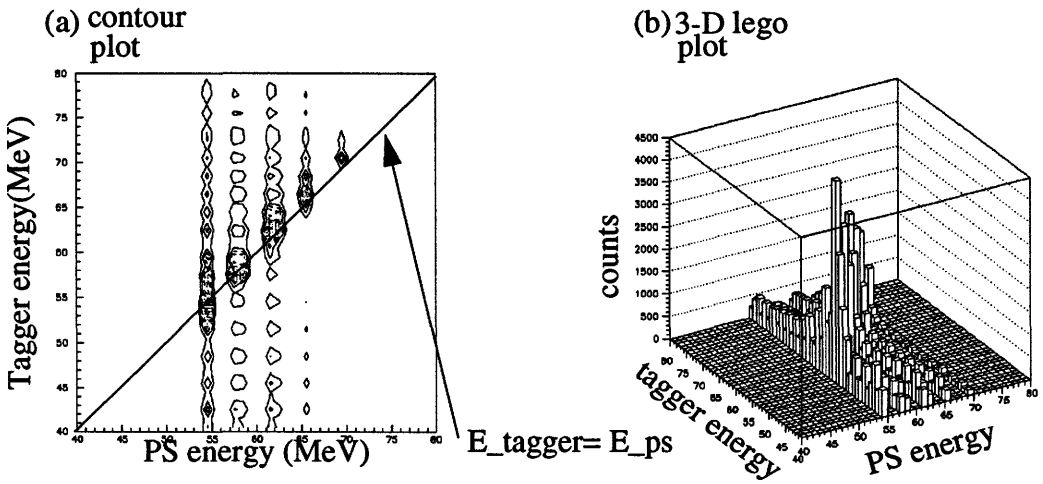

Figure 4.13. A contour plot of the PS detected energy versus that seen by the tagger (a) and the same plot in three dimensions (b).

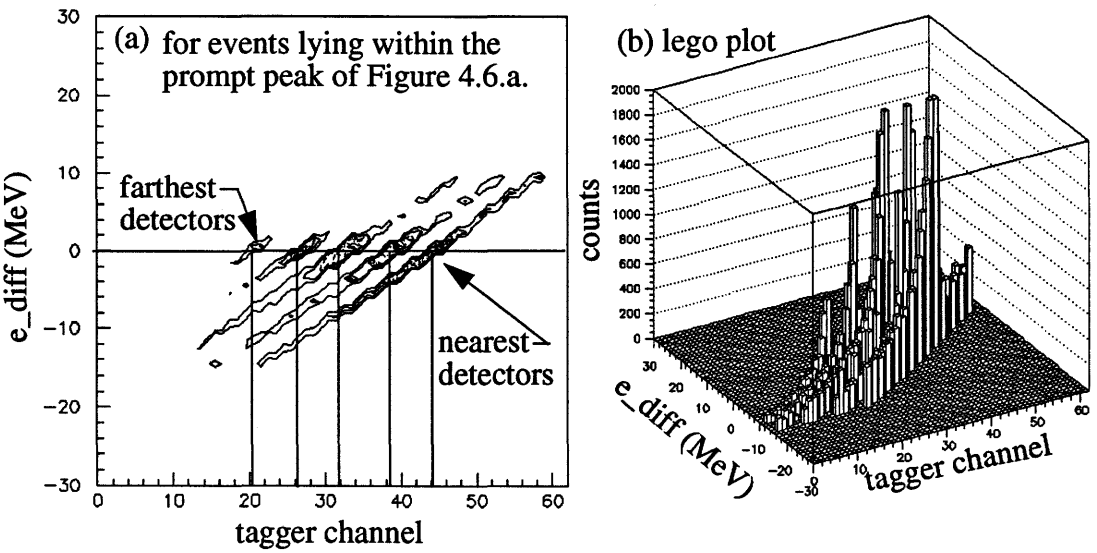

Figure 4.14. The energy difference as a function of tagger channel.

4.13 Comparison of Experimental and Theoretical energy losses

The sixteenth and second last step in the data analysis concerns the energy loss of pairs produced in the converter. In order to understand the efficiency of the instrument which includes the effects of energy loss and multiple scattering in the converter, a complete simulation of the PS is required. Before doing this, however, some idea of the magnitude of the effect from the collisional and radiation energy losses for electrons passing through the copper foils is useful. Expected energy losses for a particle travelling the entire foil thickness in the various converters are shown in Appendix C and some results are reproduced in Table 4.1.

The ionization loss varies logarithmically with energy and linearly with the atomic number Z as shown in Appendix C, Equation C.1. The energy loss due to bremsstrahlung, however, varies almost linearly with energy and quadratically with Z (see Equation C.5). Another difference between these two processes is that most of the energy loss from radiation is carried away by a single photon while in collisions there is nearly a continuous degradation in energy. In copper, above the critical energy of 24.8 MeV the energy loss due to radiation begins to exceed that from collisions. Thus in our momentum range the energy loss due to radiation was slightly greater than that for collisions.

The energy loss in the converter was studied with reference to Figure 4.12. and the experimental values are compared to the calculated mean energy losses in Table 4.1. The three square converters and the annular converter were considered. These experimental energy losses were roughly estimated since too many parameters were required to fit the data with the required precision. The most likely energy loss due to ionization and radiation (from Appendix C) for charged pairs (assuming conversion in the middle of the foil) striking the nearest PS detectors is given in Table 4.1 and is equivalent to a single charged particle travelling the entire foil thickness.

Table 4.1: Energy losses

Converter thickness ([mm, L_R])	Mean energy loss of charged pairs [MeV]	Estimated energy loss from Figure 4.12 [MeV]
square (4.55, 31.8)	26.48	> 15.0
square (1.60, 11.2)	9.31	~ 15.0
square (0.70,4.9)	4.08	9.4
annular (1.25, 9.1)	7.27	~ 5.0

The difference in the heights and lengths of the energy loss tails between the standard, thin and thick converter are clearly visible in Figure 4.12. The thinnest converter with its thickness of 4.9% radiation lengths (0.70 mm Cup) gave the lowest energy loss as expected (about 5 MeV). The thickest square converter had the highest (albeit unknown) energy loss.

The estimated energy loss was greater than the calculated mean energy loss in all cases. The energy loss tail was cut off prematurely for the thickest converter since this tail extends beyond 15 MeV.

Particles undergoing collisions have a statistical variation of energy loss. In the literature [Leo, 1987] various distributions have been formulated based on the parameter κ, the ratio between the mean energy loss and the maximum energy transfer allowed by a single collision to quantify the variance of the ionizing collisions. The corresponding distribution for the case of radiation loss by charged particles has the number of particles experiencing a given radiative loss proportional to the inverse of the emitted photon's energy. Thus the energy loss for a given charged particle can be given within some range that is most likely with a certain degree of confidence.

4.13.1 Simulating the Acceptance of the PS

The simulation software package *GEANT* [*GEANT*, 1991] was used to model the energy loss and multiple scattering due to the various secondary interactions of the photons for the 0.7 and 1.6 mm copper foils. *GEANT* gave the vertical and horizontal projections of the angles of the charged particles leaving the converter as shown in Figure 4.15 for 1,000,000 photons having an incident energy of 55.0 MeV. Naturally these projections should be identical, however, they were used to determine the absolute efficiency of the PS for the nearest set of detectors which has a different acceptance in the horizontal and vertical planes. Software limits were placed on the horizontal and vertical angles corresponding to the acceptance in these directions by the PS.

In the vertical plane the charged particles are predominantly limited by the height of the plastic scintillators used for the PS detectors. The vertical angle limit (±40 mr) for the charged particles being accepted into a given detector was calculated in Section 2.4.2 assuming a point beam spot at the converter. For the horizontal acceptance the software package *Raytrace* gave point to point focussing for radial angles up to 200 mr.

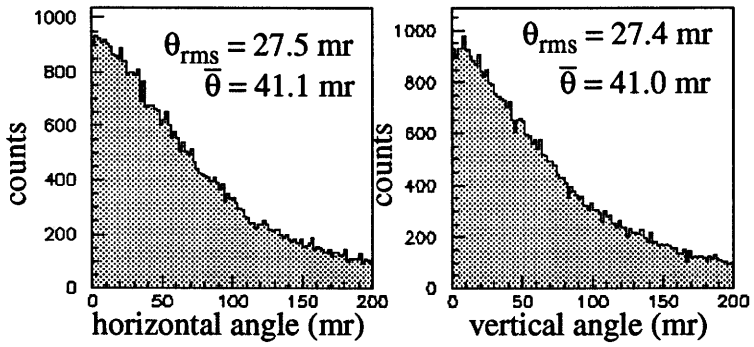

Figure 4.15. The horizontal and vertical angles (with respect to the incident beam) of the charged particles leaving the thinnest converter.

The simulation results of energy loss for two square converters is presented in Figure 4.16. Once angular software cuts were applied the width of the peak was less than 1.0 MeV. This implies that the intrinsic resolution of the PS was less than 1.0 MeV since the FWHM of the *e_diff* spectra was about 2.0 MeV. Figure 4.17 takes slices of Figure 4.16 (b) and (d) in 0.5 MeV bites and gives the simulated response to a monochromatic beam that was also shown using the experimental configuration in Figure 4.11.

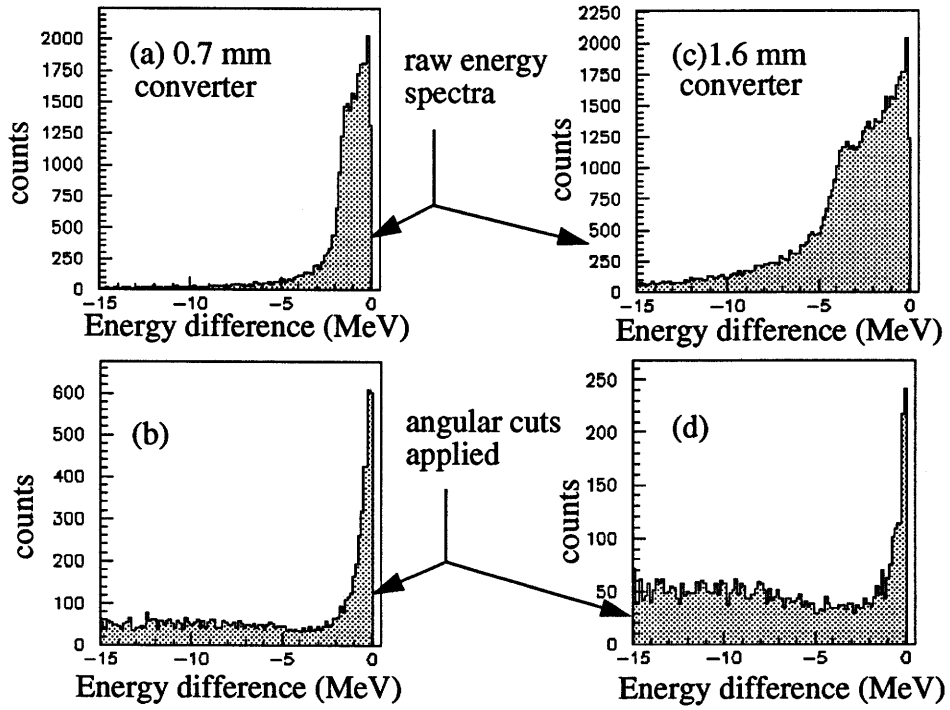

Figure 4.16. The *e_diff* spectra for charged pairs from the conversion of a 55 MeV photon.

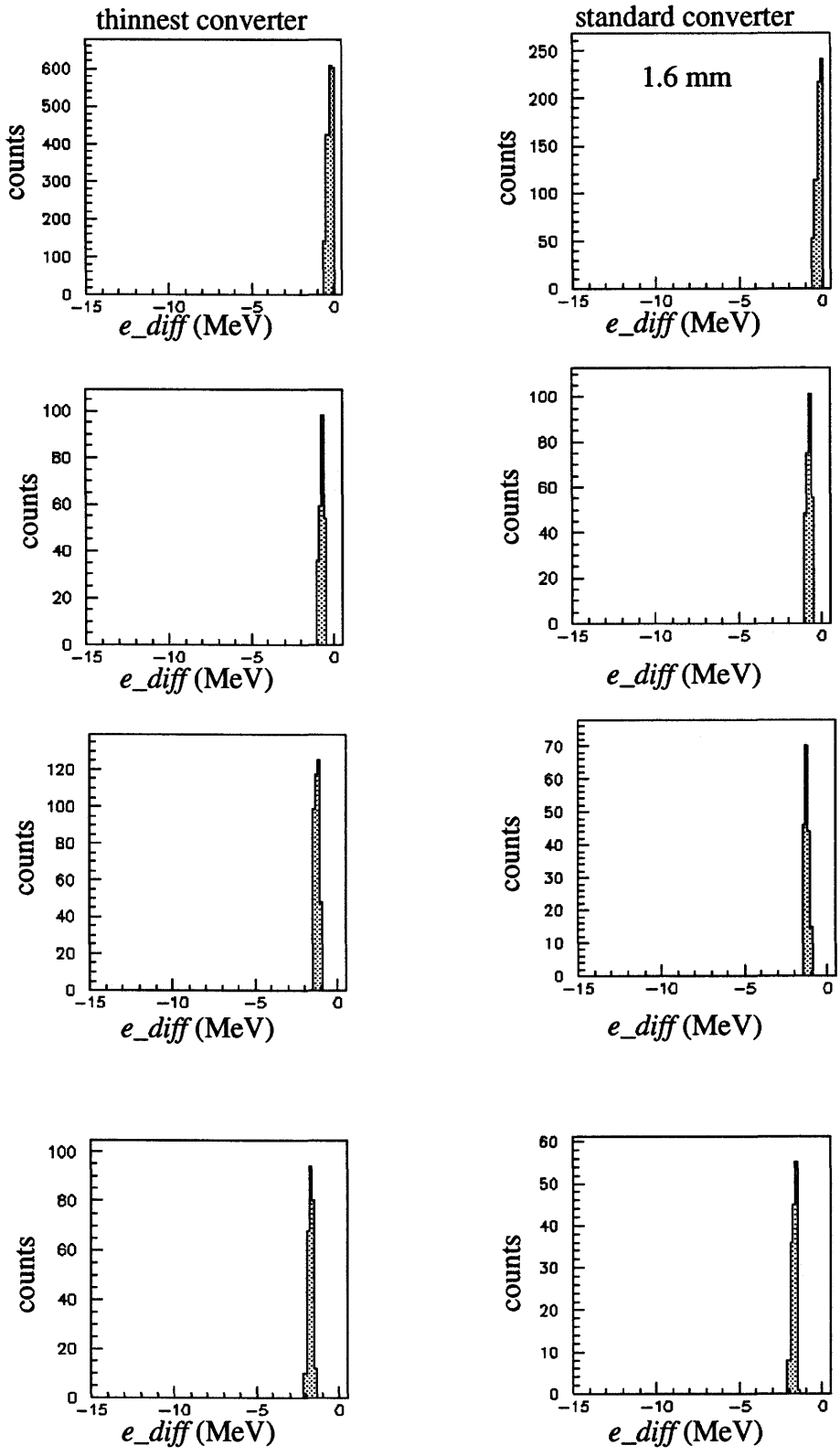

Figure 4.17. Results of the *GEANT* simulation for two foils.

To compare figures 4.17 and 4.11 an adjustment had to be made to Figure 4.11 since the energy bin with the most counts present in this figure corresponded to an energy difference between 0.0 and +0.5 MeV while it should be in the energy bin between 0.0 and -0.5 MeV due to energy loss considerations. This was caused by the finite energy bite of the PS detectors and calibration error of the PS. Additionally, tagged photons were used from adjacent tagger channels so energies varied from (55 to 57) MeV while the simulated results had a constant incident photon energy. The relative heights of the counts in each of the energy bins of the simulated results scale in the same manner as the counts in the test run of the PS. The scaling ratios of the simulated results are within 10% of scale factors associated with the shifted test results. On this basis, one can use the efficiency calculated by the simulation to infer the efficiency of the PS.

4.14 Systematic and Statistical errors

The final point in the data analysis includes a discussion of the errors associated with the commissioning tests of the PS. These errors were quantified and the reasons for their values are indicated. Systematic errors exist in the tagged photon energy calibration, PS energy resolution, and acceptance of the PS. In all cases statistical errors were negligible compared to the systematic errors since we acquired large numbers of events.

The final *e_diff* histograms were calculated based on knowledge of the tagged photons' energies. When this test was performed the electron beam energy was measured by one of two bending magnets (B701 and B303) and thus was dependent on how precise these magnets were in their energy determination. What was just as critical in the tagged photon energy determination, however, was the calibration of the tagger magnet. The uncertainty in the tagged photon energy is less than 1 MeV.

It was clear that the *e_diff* spectra were not gaussian in shape. This attribute was a hindrance since the FWHM criterion is normally applied to gaussian responses, only. Thus determination of the error in the energy resolution of the PS is difficult.

The focal plane detectors do not introduce any new errors if they are positioned properly since they are virtually 100% efficient provided the high voltage on the phototubes was set correctly and the discriminators that receive these analog pulses were adjusted to the correct levels. However, the focal plane was approximated by a straight line even though it had a slight curve associated with it (< 2%).

The determination of the effective field boundary had a small systematic error (± 5%), however, slight inaccuracies in the magnetic field strength can propagate through the magnetic system and give large deviations in the momentum determination of the detected charged particles. As an example, it has been calculated that a 2% change in the magnetic field at 0.5 T results in a proportional displacement of about 9.0 mm along the focal plane for a 25 MeV particle. This is the limit for a charged particle to still strike the PS detector since it was 25 mm wide and 25 mm tall. It is also known that the entrance and exit effective field boundaries are not the same due to differences in the yoke configuration. This effect and others are shown in Table 4.2.

Table 4.2: Systematic Errors

Quantity	Systematic error
Acceptance (per detector)	~ 5%
PS detector placement	< 1%
Effective field boundary	< 5%
Electron beam energy	< 1MeV
Detection efficiency	~ 1%

Chapter 5. CONCLUSIONS AND RECOMMENDATIONS

This chapter begins with a discussion of the *e_diff* spectra. The angular acceptance of the PS is estimated by placing vertical and horizontal angular limits on the pairs. Experimental results and results of the simulations will be compared. The conclusions follow from the commissioning test run. Recommendations are described which are incorporated in the final configuration of the pair spectrometer. Recent test results using this final configuration end the main body of this thesis.

5.1 Discussion of Results

The purpose of the data analysis was to bring the data to a form where three quantities could be studied. These are the energy calibration of the PS with respect to the tagger; the energy resolution of the PS and the efficiency of the device.

An example is given to refresh the reader and emphasize some important points concerning the spectrometer. Consider the *e_diff* spectrum shown in Figure 5.1. Recall that a tagged photon could interact at any depth in the converter. If conversion occurred at or near the front of the converter then the charged particles still had to traverse the rest of the copper foil where they lost energy according to the thickness of converter that was remaining. Thus the tagged photon energy would have to be greater than that reconstructed by the PS to account for this energy loss and would appear on the left hand (negative) side of the spectrum. The long tail on the negative side of the *e_diff* spectra was also due to a detected PS energy lower than the corresponding tagged photon energy but this was caused by bremsstrahlung of the pairs. This radiative tail is software truncated in the present case.

It is apparent that the peak position in the *e_diff* histograms was due to tagged photons that converted very close to the downstream side of the converter. Note that the energy bin ranging from 0.0 to 0.5 MeV in these spectra had the highest number of counts present but it was just pointed out that this difference should be equal to or less than zero due to energy loss considerations. The ambiguity is easily resolved since there is a finite calibration error between the pair spectrometer and tagger.

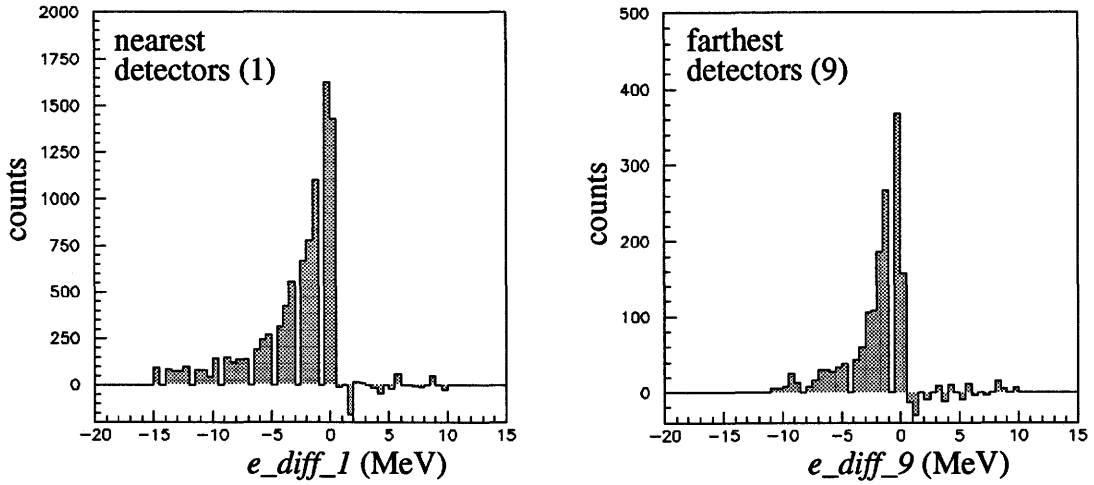

Figure 5.1. The normalized *e_diff* spectra for a reverse polarity run.

There were still counts present on the right hand side of the peak in some of the *e_diff* spectra once all backgrounds were accounted for but in almost all cases they averaged to zero. In the thickest converter configuration and a few other runs (i.e. no sweep magnet present) backgrounds on the right side of the peak persisted with an average slightly larger than zero. This is understandable if one considers that the thickest converter introduced secondary interactions that were proportional to the square of the converter thickness. Thus the thickest converter foil did not scale to the standard configuration in a linear manner.

Since the peaks in the energy difference histograms fell near zero, the span of the tagger focal plane moves with respect to the peak for higher (lower) energies of tagged photons. This was seen in Figure 4.5 and Figure 5.1 where the sharp cutoff at -10 MeV (for *e_diff_9)* was due to the low energy end (for recoiling electrons) of the tagger focal plane acceptance that corresponded to the upper limit of high energy tagged photons for this tagger setting.

5.2 Estimation of Photon Splitting Count Rate

It has been previously stated in a SAL proposal [Retzlaff,1991] and alluded to in the first Chapter that at exiting angles between 7 and 15 mr the cross section for photon splitting was conservatively assumed to be 150 μb for tagged photons in the 130 - 170 MeV energy range. This gives a photon pair rate of 160/s for 1×10^8 γ/s incident on the 0.6 L_R lead target (3.4 mm). Both Retzlaff and Milstein assumed a tagging efficiency of 50% but

a more realistic estimate (for the tagging facility at SAL) is 10% using a lead collimator having a 4 mm diameter which would be placed approximately 80 cm downstream of the tagger radiator. This leads to a rate of 16 split pairs per second or ~1×10^6/day. If the overall acceptance for both photons incident on the PS is sufficient (~3×10^{-6}) then a few split photon pairs per day should be detected.

Recall that the acceptance of the pair spectrometer can be roughly estimated from Equation (2.4.2). The first term to consider is the conversion probability. For a gold converter of 2.8% L_R (0.1 mm thickness) the pair production conversion probability at 100 MeV is 1.7% for a single photon. We used copper converters with the thinnest being 4.9% L_R (5.948×10^{21} cm^{-2}) and for photons between 50 to 70 MeV the pair production conversion probability is ~ 0.4%. The screened cross section for pair production in copper was numerically integrated [Asai, 1994]. For the thinnest foil this probability was greater than 2% (this factor becomes 4×10^{-4} for two photons) for the momentum range used in the test and provided the PS *sees* all the charged pairs produced.

The solid angle subtended at the target by the annular converter for photons between 7 and 15 mr is 0.5 msr, however, this has already been accounted for in determining the number of photon pairs incident on the converter. Assuming a geometrical detection acceptance of 20% (Höistad *et al.* had 26%) and that 90% of the events do not appear in the radiative tail gives an overall acceptance of ~2.8×10^{-6} over the stated photon energy range, however, more PS detectors are required to cover the energy acceptance. Thus two to three splitting events per day could be detected using the final configuration of the spectrometer.

Experimental results gave about 6000 events detected in the prompt peak (over a energy difference bite of 1.5 MeV) for the nearest detectors (i.e. one pair of detectors) and assuming this was caused by a single tagger channel having a rate of about 1 MHz (or 50,000 s^{-1} assuming a 5% tagging efficiency, see Appendix E.2) and a run period of 5000 seconds we obtained a rough idea of the acceptance (~ 5×10^{-4}, for a single photon at a PS detected energy of 54.47 MeV). For two photons to be recorded the acceptance would be squared (1.4×10^{-8}). This is in fair agreement with the previous estimate. If the number of PS detectors was increased by a factor of 16 (i.e. 32 focal plane detectors) then so would the acceptance for a single photon and would give 6.4×10^{-5} for two photons.

Results of the Monte Carlo simulation using the angular cuts dictated by the PS geometry and the same energy bite of 1.5 MeV (for an incident photon energy of 55 MeV) gives an acceptance of 4×10^{-4} for a single photon and two detectors. Again multiplying by 16 and squaring this result gives an acceptance of 4.1×10^{-5} for a photon pair.

5.3 Conclusions

The PS is a useful device for measuring the energies of gamma rays and was found to have a FWHM energy resolution under 2.0 MeV for tagged photons between 50 and 70 MeV. The thicker converters did not improve the efficiency of the PS (in fact they worsened it) since the extra conversions were scattered out of the PS acceptance and all that was detected was the back edge or downstream side of these converters. For this reason the thickness of converters did not have an appreciable effect on the resolution.

The difference in absolute energy determination between the PS and SAL tagger was less than 1.0 MeV using the contour plot of Figure 4.12. However, when a linear fit was performed (once the lowest detected photon energy was subtracted, i.e. 54 MeV), the proportionality constant was 1.08 ± 0.03 and the intercept was 0.03 ± 0.25. The χ^2 was 0.87 indicating that the errors allowed too much variance in the fit. According to this fit there is a 2.7 MeV difference between the PS and tagger for a 54 MeV photon which is difficult to believe after viewing Figure 4.12.

For the nearest detector the nominal momentum was (26.25 ± 0.75) MeV/c. Thus (on average) the energy span of a single PS detector was 1.5 MeV at a magnetic excitation of 0.5 T. This compares to an energy bite of less than 0.70 MeV for a single tagger channel having a photon energy of 54.26 MeV (tagger channel 44).

The experimentally determined efficiency for a single photon incident on the PS was estimated to be 1×10^{-4} at (55.00 ± 0.75) MeV. If 32 detectors are used then the acceptance would increase by a factor of 16 since there are 16 times as many detectors. Squaring this for two photons and assuming all photon pairs are incident on the PS converter yields a photon splitting rate of roughly 2-3 per day.

The #3 tagger radiator (12 microns Al) or thinner should be used for future applications of this instrument since the highest number of normalized counts were for this thickness of radiator. Similarly a copper converter foil of thickness less than 1 mm will

improve efficiency by keeping the charged pairs from being scattered out of the acceptance of the PS. This is understandable since multiple scattering within the radiator and converter of the charged particles is reduced as the thickness is decreased.

5.4 Recommendations

Improved performance would be obtained in all converters by decreasing their thickness and in the case of the annular converter, enlarging its outer diameter while minimizing the inner air gap. This increases the number of split photon pairs incident on the converter.

Incorporation of a vacuum chamber from the radiator to the dipole and in the air gap between the dipole faces would further reduce room backgrounds. This would remove the effect of air conversions, energy loss due to the air and any small angle scattering experienced by the charged particles.

The scintillation detectors should be placed normal to the charged particles' trajectories which enables more events to be recorded and gives the same path length through each scintillator. Additionally more detectors should be placed on the focal plane (preferably side by side) to give a larger energy acceptance. There is a case to be made for placing the scintillator faces between edge-on and normal to the charged particles' trajectories in order to more closely match the magnet's intrinsic resolution to the detectors'.

The detection efficiency of the scintillation counters is affected by how close to the magnet the scintillation counters can be placed even with extensive shielding. Magnetic field strengths as small as 5 Gauss seriously impair the performance of the phototube. Thus at high field settings it is imperative that the nearest focal plane detectors have adequate magnetic shielding.

A thorough understanding of the effective field boundary is required for accurate energy determination. A careful study of the fringing field should be carried out to be able to know the magnet properties for future use (possible double focussing applications).

5.4.1 Final Configuration of Pair Spectrometer

In the period following the tests described in this thesis, the final configuration of the PS was developed and most of the recommendations have been implemented. However, further improvement would result if a permanent structure was attached to magnetically shield the phototube cathodes especially those near the magnet. This is imperative for high excitations of the dipole.

This device may be used over a broad energy range, from (30 - 180) MeV, when measuring the tagged photon's energy provided that different magnetic field settings are used. If one is interested in using the PS as an electron beam monitor or to detect electrons that are products of a nuclear reaction then the energy scale is halved.

Currently 32 focal plane detectors have been installed utilizing Hamamatsu (1450) photo-multiplier tubes. These tubes were chosen since they gave high gains and were less expensive than the corresponding photomultiplier tubes available from Philips. They had 10 amplifying stages and a spectral range from 300 to 650 nm. Manufacturer's stated rise times were 1.8 ns.

The experimental setup for photon splitting was briefly described in Section 5.2. The 4 mm diameter lead collimator will have a length of 150 mm and will likely be placed 80 cm downstream of the tagger radiator. The object here is to shield the PS converter from γ-rays directly from the radiator. Following this is the splitting target (0.6 L_R Lead) and after a drift of 100 cm will be the PS converter which is annular and will have a thickness less than 0.7 mm copper (but a higher Z material will likely be used) as well as inner and outer diameters of 19 and 35 mm, respectively. Note that the entire setup from radiator to just before the PS detectors will be under vacuum and is depicted in Figure 5.2.

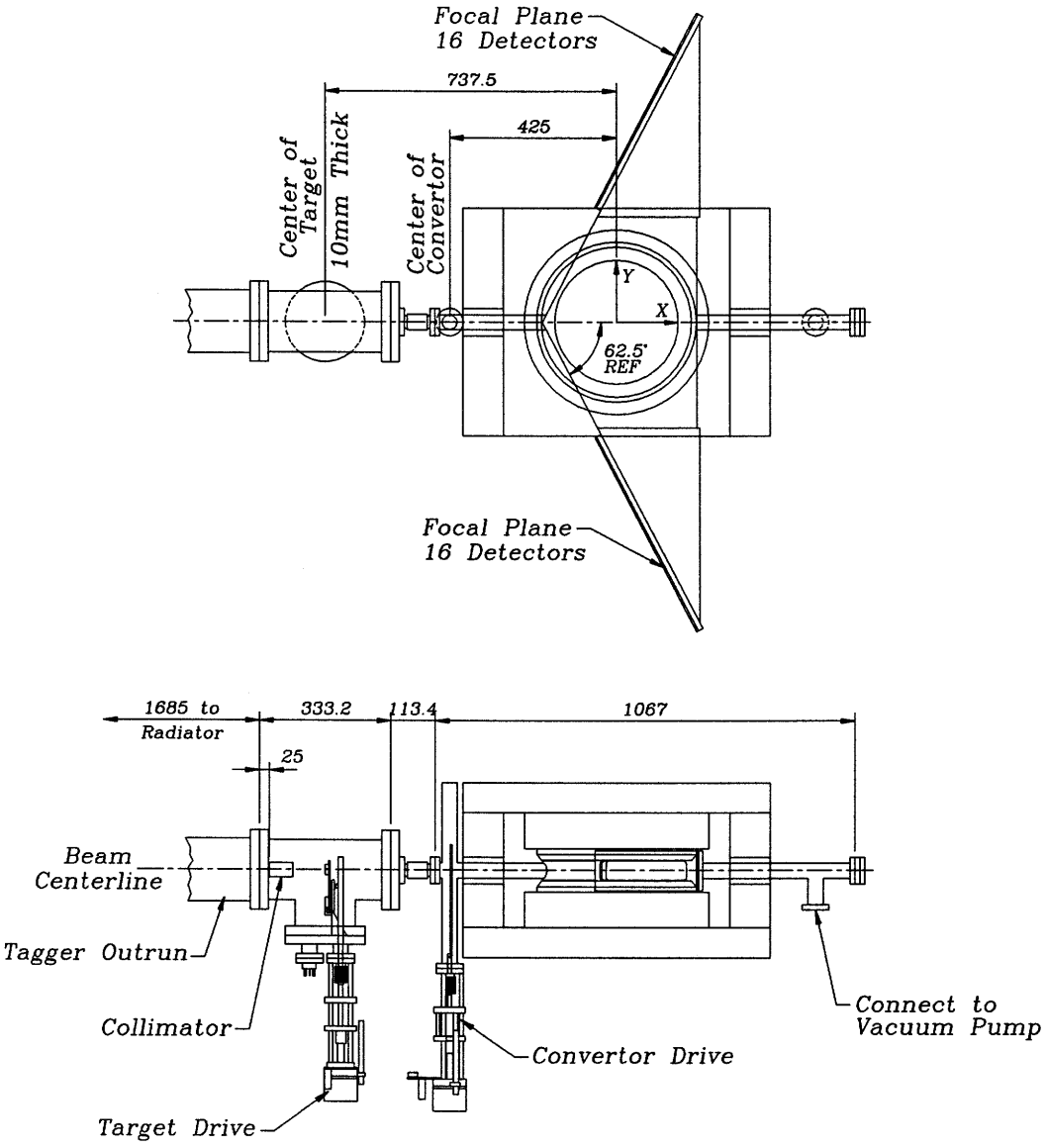

Note: All Dimensions are in Millimeters

Figure 5.2. The SAL pair spectrometer.

5.5 Recent Results

In February, 1994 SAL tagger energy calibration tests were performed and one test was done to check the energy calibration of the final bending magnet prior to the tagger. The electron beam was passed through the switched off SAL tagger and was directly incident on the PS. Figure 5.3 gives results for a pulsed beam energy of 59.5 MeV. A determination of the dispersion was carried out using the fitted results that gave the PS channel that was struck and is presented in Appendix B.2. It was reassuring that the dispersion was consistent with that calculated by the Browne-Buchner equations and the software packages *Raytrace* and *Transport*. Regardless of the method the momentum dispersion was found to be about 6.00 mm/% with a variance less than 0. 50 mm/%.

More tests were conducted on the PS magnet and are tabulated in Table 5.1 for different tagger settings and PS dipole excitations, along with the span of the energies capable of being measured by the PS.

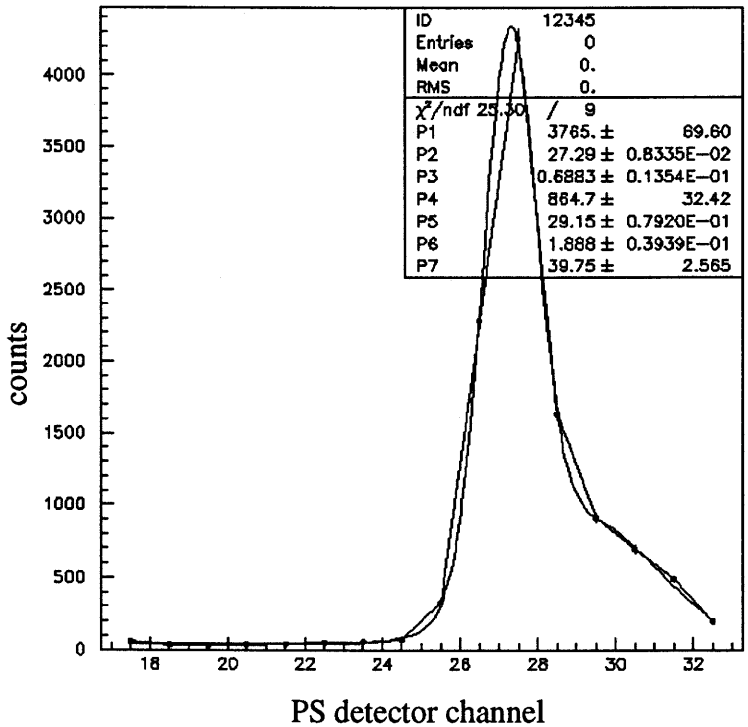

Figure 5.3. Pulsed beam data for 59.5 MeV.

From these recent tests and others the EFB was determined to be different upon entrance and exit of the charged particles as well as a function of the magnet excitation. This was due to the yoke not being cylindrically symmetric. At a magnetic field strength of 0.5 T the entrance EFB was 219 mm and upon exit it was 223 mm which is close to the previous value of 210 ±10 mm.

As of now the PS in its final form is ready for use but further simulations should be carried out on this configuration to optimize the choice of target and converter for use in the photon splitting experiment.

Table 5.1: Energy ranges for the PS

tagger setting	tagger focal plane energy range (MeV)	PS field (Gauss)	PS Energy range [MeV]
380	43 - 80	5335	60 - 82
		4089	46 - 62
		3255	36 - 50
500	67 - 100	6961	78 - 108
		5335	60 - 82
640	85 - 113	9050	100-140
		6961	78 - 108

REFERENCES

Adler and Cohen, 1966 — A. W. Adler and S. G. Cohen, Phys. Rev. **146**, 1001 (1966).

Amendt, 1991 — D. Amendt, *Differential Cross Sections for Compton Scattering off the Proton at 185 MeV,* M. Sc. thesis, Univ. of Sask., (1991) unpublished.

Asai, 1993 — J. Asai, private communication (1993).

Barber, 1933 — N.F. Barber, *Proc. Leeds Phil. Lit. Soc. Sci. Sect.* 2, 427-434 (1933).

Baier *et al.*, 1974 — V. N. Baier *et al.*, Phys. Lett. **49B**, 385 (1974).

Bartholomew *et al.*,1979 — G. A. Bartholomew and G.E. Lee-Whiting, NIM **162**, 239 (1979).

Berger and Seltzer, 1983 — M. J. Berger and S. M. Seltzer, *Tables of Energy-Losses and Ranges of Electrons and Positrons*, Nat. Acad. Sci.-Nat. Res. Coun. Publ. 1133 p.205 (1964), also National Publications SP-3012 (1964) and SP-3036 (1966).

Boccaletti *et al.*, 1966 — D. Boccaletti *et al.*, Nuovo Cimento **43A**, 115 (1966).

Bolsterli, 1954 — M. Bolsterli, Phys. Rev. **94**, 367 (1954).

Bukhvostov *et al.*, 1963 — Bukhvostov *et al.*, Soviet Phys. JETP **16**, 462 (1963).

Brown *et al.*, 1970 — K. L. Brown, B. K. Kear, and S.K. Howry, *Transport* SLAC Report No. 91, Stanford, Calif).

Browne *et al.*, 1956 — C. Browne and W. Buechner, The Review of Scientific Instruments Vol. 27 No. 11 (1956).

Constantini et al., 1971 — V. Constantini *et al.*, Nuovo Cimento **2**, 733 (1971).

Davies et al., 1954 — H. Davies, H. A. Bethe, and L. C. Maximon, Phys. Rev. **93**, 788 (1954).

Dallin, 1990 — L. O. Dallin, *High Duty Factor Monochromatic Extraction from Eros*, Ph.D. thesis, Univ. of Sask., (1990) unpublished.

Fernow, 1986 — R. C. Fernow, *Introduction to Experimental Particle Physics*, Cambridge University Press, 1986.

Hallin and Vogt, 1994 — E. Hallin and J. M. Vogt, private communication (1994).

Höistad *et al.*, 1990 — Höistad *et al.*, NIM **A295**, 172 (1990).

Jarlskog *et al.*, 1973 — G. Jarlskog *et al.*, Phys. Rev. **D8**,3813 (1973).

Johannessen *et al.*, 1980 — A. Johannessen, K. Mork, and I. Overbo, Phys. Rev. **D22**, 1051 (1980).

Klein and Nishina, 1929 — G. Klein and Y. Nishina, Z. Physik **52**, 853 (1929).

Kowalski 1986 — S. Kowalski and H.A. Enge, *Raytrace* (Laboratory for Nuclear Science, Department of Physics, 1986).

Laxdal, 1980	R. E. Laxdal, *Design of an Energy Compression System for the Saskatchewan Linear Accelerator,* M. Sc. Thesis, Univ. of Sask. (1980) unpublished.
Leo, 1987	W. R. Leo, *Techniques for Nuclear and Particle Physics Experiments*, Springer Verlag, (1987).
Livingood, 1969	J. J. Livingood, *The Optics of Dipole Magnets*, Academic Press, (1969).
Maric and Mobius, 1959	Z. Maric and P. Mobius, Nucl. Phys. **10**, 135 (1959).
Miller *et al.*, 1988	Miller *et al.*, NIM **A270**, 431 (1988).
Milstein *et al.*, 1991	A. Milstein and B. Wojtsekhowski, Novosibirsk preprint (1991).
Mladjenovic, 1979	M.S. Mladjenovic, NIM **162**, 193 (1979).
Neal et al., 1968	R. B. Neal *et al.*, *The Stanford Two Mile Accelerator,* W. A. Benjamin, Inc., New York (1968).
Norum, 1993	W. E. Norum, IEEE Trans. in Nuc. Sci., accepted for publication, (1994).
Pywell, 1992	R. Pywell, private communication (1992).
SAL, 1990	Saskatchewan Accelerator Laboratory, *LUCID Data Acquisition and Analysis System User's Guide*, Version 1.2 (1990).
Retzlaff, 1991	G. A. Retzlaff, *Photon Splitting in a Nuclear Coulomb Field*, SAL Proposal 048, (1991).
Shima, 1966	Y. Shima, Phys. Rev. **142**, 944 (1966).
Siegbahn, 1966	K. Siegbahn, *Alpha-, Beta-, and Gamma Ray Spectroscopy*, North Holland Publishing Company, Amsterdam, (1965)
Siegbahn, 1950	Siegbahn and Johansson
Vogt, 1992	J. M. Vogt, private communication (1992).
Vogt *et al.*, 1993	Vogt *et al.*, **NIM A324**, 198 (1993).
Vogt *et al.*, 1994	J. M. Vogt and R. Florizone, NIM **A339**, 425 (1994).
Williams, 1935	E. J. Williams, Kgl. Danske Videnskab. Selskab, Mat. - fys. Medd. **13**, No. 4 (1935).

APPENDICES

A.1 Excitation Curves

Measurements were made of the magnetic induction at the center of the dipole as a function of the current supplied to the coils to generate an excitation curve and verify the adequacy of the power supply and the field strength. The magnetic field was measured with a RFL model 902 Hall probe having a sensitive area of (20 x 8) mm. The resulting curve is shown in Figure A.1.

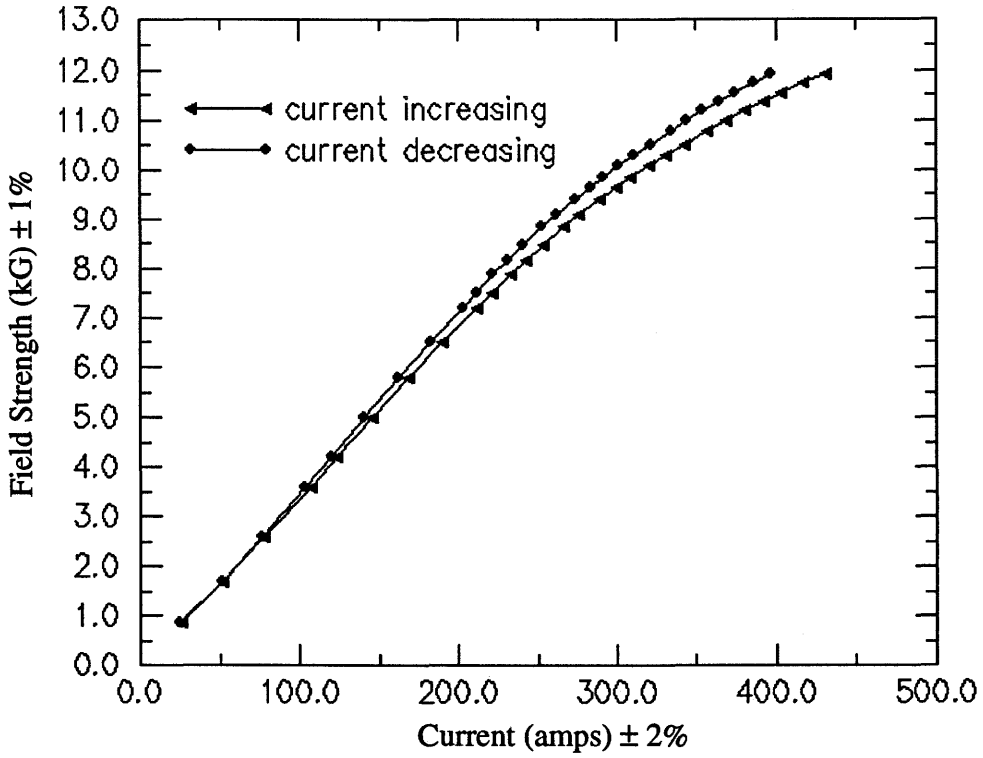

Figure A.1. Excitation curve: magnetic field strength as a function of current.

Note that the graph does not have the expected shape of a magnetic hysteresis curve. This was due to the magnet already having been cycled to a large value of current but less than the maximum (400 A). In the normal operation of the dipole, care was taken to cycle it to maximum current and then down to the desired current to obtain consistent readings of the magnetic field strength by remaining on the same portion of the hysteresis curve.

The accuracy of the Hall probe was 0.25% ± the last digit on all ranges (stated by the manufacturer) at best, however, we believe it was higher due to large drifts (±20 G) when zero point calibration was performed for the probe. Eventually the magnetic field strength was absolutely determined by an NMR probe. The ability of the Hall probe to respond in a linear manner to small variations in field strengths is critical to mapping the dipole at a given excitation.

A.2 Determination of the effective field boundary

For a dipole the magnetic field strength is constant in the center and gradually drops to zero beyond the edges of the poles. A measurement of the magnetic field strength through the centerline of the PS dipole was performed to determine the effective field boundary (EFB) using the same Hall probe as mentioned in Appendix A.1. The method consisted of moving the probe, in 1 cm increments, along the magnetic midplane of the dipole from a large enough distance such that no magnetic field was detected, through the maximum in magnetic field strength and then out through the other side. The curve produced relates the magnetic field component, B_v to the distance from the dipole center, r.

While the trajectory of a charged particle through a field of the form shown in Figure A.2 can be obtained by numerical integration of the equations of motion, for most practical purposes the first order methods discussed in Chapter 2 are used. The concept of an effective field boundary replaces the gradual drop of the field by a sharp transition from full field to zero. It can be shown (Livingood, 1969) that the effective edge concept is valid provided that this edge is some distance beyond the iron pole faces and that areas A and B are equal as shown in Figure A.2. The distance at which this occurs is slightly larger than the actual radius of the pole pieces. Whenever using beam optics equations the object and image distances as well as the distance between magnetic elements need to be referenced to the effective field boundaries. If the magnetic element is unsymmetrical then the effective boundaries will be different and this situation must be taken into account in the design equations.

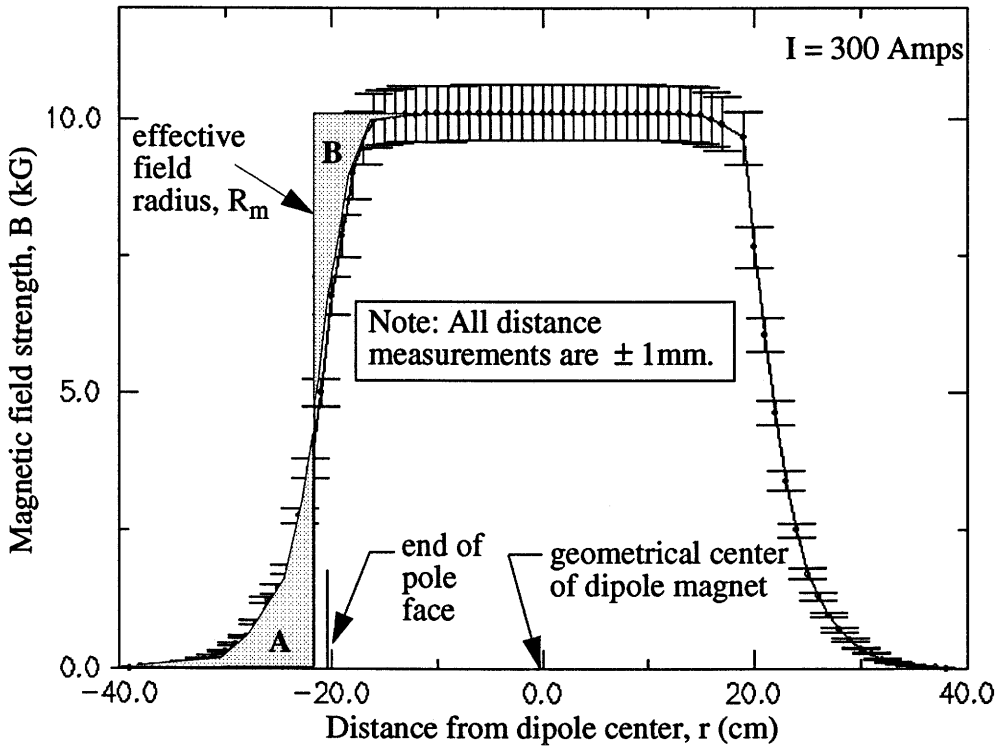

Figure A.2. The effective field boundary of the PS dipole.

Nominal settings chosen for the original determination of the EFB were an excitation of 300 A producing a maximum magnetic field of 10.1 kG. In our case the pole radius was 202 mm and the calculated EFB was 210 mm ± 10 mm (R.E. Pywell, 1992). Of course this boundary is a function of field strength and the error is only an estimate.

The actual path that the charged particles followed, however, was not through the two holes cut in the yoke. The entrance was through the upstream hole in the yoke and the exit was on the right or left hand side of the magnet due the charged particles being deflected. These two sides had less yoke present than the front and back portions and for this reason had a different fringe field and thus different effective edges. As mentioned in Chapter 5 the actual effective edges were calculated from a run with the final configuration of the PS in February, 1994 and are stated there. It was reassuring that these recent results were indeed within 10 mm of the EFB used throughout this thesis.

B.1 Calculation of momentum of charged particles

The momentum of a charged particle striking the focal plane was obtained for the central trajectory with normal entry and exit. We denote a point on the focal plane by the coordinates (x_f, y_f) and must calculate the radius of curvature, r_b, of the arc from O′ to (x_m, y_m) the edge of the effective field which is assumed to be the circle of radius r_m. Figure B.1 depicts the geometry with the appropriate coordinate axis superimposed. The procedure is to trace back from the focal plane coordinates to the effective edge by constructing a straight line from the focal point to the center of the effective field (point O).

Applying the above procedure, the first step for the momentum determination involves calculating the coordinates of the particle at the exit EFB (x_m, y_m). Equations B.1 to B.10 give the machinery required for the calculation. The first three equations are relative to the O coordinate system (centered at the geometric center of the EFB) and give the desired coordinates using the equation for a straight line and a circle. Substituting (B.1) into (B.2) yields (B.3). The only requirement is that the origin O, coordinates for the exit edge and focal plane are all collinear. This condition is automatically satisfied using the Browne-Buchner configuration as mentioned in Chapter 2.

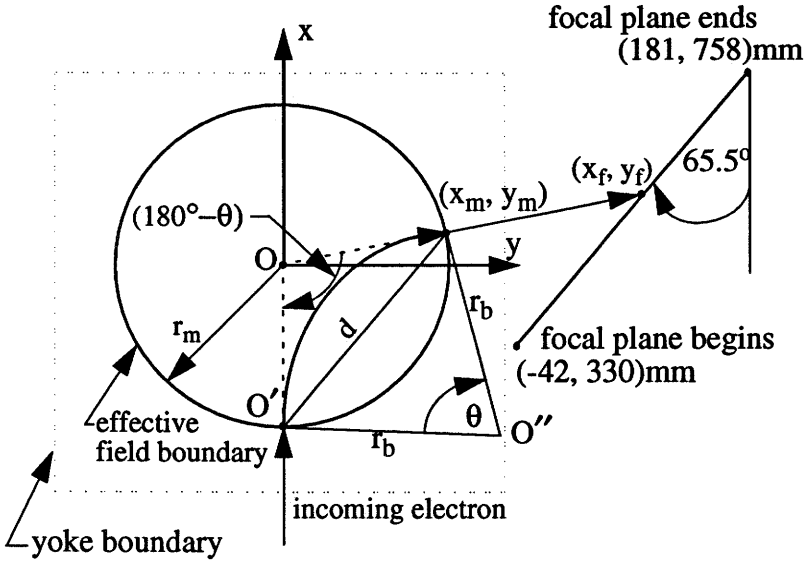

Figure B.1. Geometry for determination of focal plane coordinates.

$$y_m = \frac{x_m \cdot y_f}{x_f} \tag{B.1}$$

$$x_m^2 + y_m^2 = r_m^2 \tag{B.2}$$

$$(x_m)^2 = \frac{r_m^2}{1 + \left[\frac{y_f}{x_f}\right]^2} \tag{B.3}$$

Another Equation (B.4) arises from the cosine law using angles θ and (180° - θ) and equating the two expressions using the common side, d. This equation was not solved for the bend radius due to its nonlinearity but it provided a simple check for the calculated bend angle. Further, the derivative of the bend angle with respect to the bend radius gave the matrix element R_{21}, the variation of the radial slope versus the radial displacement, <x′|x>, and is shown in Equation (B.5). Appendix B.2 uses this formula to check with the *Transport* generated value.

$$\cos(\theta) = \frac{r_b^2 - r_m^2}{r_b^2 + r_m^2} \tag{B.4}$$

$$R_{21} = \frac{\partial\theta}{\partial r_B} = \frac{\partial\theta}{\partial\cos\theta} \cdot \frac{\partial}{\partial r_B}\cos\theta = \frac{-4 r_B r_m^2}{\sin\theta\left(r_B^2 + r_m^2\right)^2} \tag{B.5}$$

Without complications the origin can be shifted to O′ by the following transformation Equations (B.6) and (B.7).

$$x' = r_m + x_m \tag{B.6}$$

$$y' = y_m \tag{B.7}$$

The equation of the arc centered at O″ can be described with respect to O′ using Equation (B.8). Substituting for the various quantities and solving for r_b gives the bending radius of the particle trajectory in the uniform magnetic field as shown in Equation (B.9). The momentum in MeV of the particle can be calculated from (B.10) since the magnetic field (Tesla) and bending radius (cm) is known. A simple program was written that tabulated energies for various positions on the focal plane using a constant effective field boundary of 210 mm.

$$(x')^2 + (y' - r_b)^2 = r_b^2 \tag{B.8}$$

$$r_b = \frac{r_m(r_m + x_m)}{y_m} \tag{B.9}$$

$$p = 2.998 B r_b \tag{B.10}$$

The inverse process can be used to determine the focal plane positions given the momentum of the particle. The same equations could be used but quadratic equations are involved so the algebra is more tedious. A simpler method involves using the equations specifically developed for beam optics.

The radial magnification, M_x, is simply defined as the image width divided by the object width (i.e. x_i/x_o). An equivalent description can be found in the references (Livingood, 1969) for the general case. For the simplified case of motion in a uniform magnetic field having normal entry and exit the correct expression is given by Equation (B.11) where L_{ox} is the radial object distance measured in multiples of bending radius (i.e. S_o/ρ) and θ is the bend angle. With the magnification defined the image distance, L_{ix} can be described as shown in Equation (B.12).

$$M_x = -\frac{1}{L_{ox}\sin\theta - \cos\theta} \tag{B.11}$$

$$L_{ix} = -M_x(L_{ox}\cos\theta + \sin\theta) \tag{B.12}$$

Once the image distance from the effective edge S_{ix}, is known it may be broken up into (x,y) components using the bend angle to determine (x_f, y_f). Again a simple program was written to calculate the focal plane positions for a given magnetic field strength and momentum.

Some values of focal plane positions are tabulated in Table B.1 for a magnetic field of 0.5 T and momentum of the electrons ranging from (25 -35) MeV/c using an effective field boundary of 210 mm. The coordinates given are for the center of the detectors. The nine combinations of tagged photon energies that may be detected are given in Table B.2 and were the values used in constructing the *e_diff* spectra.

Table B.1. Focal plane positions as a function of momentum.

Momentum (MeV/c)	x_f (mm)	y_f (mm)
25.00	-64.9	279.3
26.00	-57.1	296.8
26.25 (0)	-55.0	301.3
27.00	-48.6	315.3
27.20 (3)	-46.8	319.2
28.00	-39.3	335.1
30.00	-18.2	378.6
30.20 (1)	-15.9	383.3
30.43 (4)	-13.2	388.8
34.00	37.6	488.1

Table B.1. Focal plane positions as a function of momentum.

Momentum (MeV/c)	x_f (mm)	y_f (mm)
34.36 (5)	43.8	499.8
34.40 (2)	44.5	501.1
35.00	55.4	521.7

Table B.2. The expected energies of tagged photons measured by the PS.

Number	Energy [MeV]
1	54.47
2	57.70
3	61.63
4	58.42
5	61.65
6	65.58
7	62.62
8	65.85
9	69.78

B.2 Dispersion of the pair spectrometer

Having defined the magnification in Appendix B.1, another quantity given in Equation B.13 for normal entry and exit of a reference ray through a uniform field dipole is the resolution function, F. It is commonly used to define the dispersion coefficient (D) as given by B.14, where ρ is the bend radius.

$$F = 1 - \frac{1}{M_x} \tag{B.13}$$

$$D = -FM_x\rho = \rho(1 - M_x) \tag{B.14}$$

The dispersion is equal to the total radial displacement of the image divided by the beam's momentum deviation (Δp/p) when the object is considered as a point source. Recall from Chapter 2 that this is the matrix element X_{13} or $\langle x|\delta\rangle$. Using the above equations the dispersion has been determined for the pair spectrometer at two magnet excitations and the results are presented in Table B.3.

Table B.3. Calculated Dispersion of the PS.

B (T)	Momentum (MeV/c)	ρ(m)	M_x	D(m)
0.8276	60.0	0.2418	-1.2557	0.5454
0.8276	60.6	0.2442	-1.2872	0.5585
0.5000	26.0	0.1734	-0.7112	0.3242
0.5000	26.3	0.1754	-0.7227	0.3022

Note that the dispersion coefficient may be altered to give units of 5.45 mm/% at 60.0 MeV. This is in fair agreement with the *Transport* simulation of the PS (6.06 mm/% @ 60.0 MeV).

The dispersion was also calculated from pulsed beam measurements using the PS in its final configuration. However, only two (of a possible three) energies were used since they were within calibration error. The energies were 57.29 (27.5) and 69.77 (24.5) MeV where the numbers in parentheses denote the middle of the channel that was struck most often using the final configuration of the PS. The coordinates on the focal plane corresponding to these two energies were (19.20, 450.75) and (56.75, 521.25) mm, respectively. The distance along the focal plane was calculated to be 79.88 mm. Assuming that the dispersion is a linear function of the particle's momentum divided by the magnetic field strength, the difference between p/B was (69.22 - 73.06) or 3.844 MeV/T. For a magnetic field strength of 0.8276T this difference equalled 3.181 MeV. Thus the displacement along the focal plane, κ divided by the change in energy was 79.88/3.18 = 25.13 mm/MeV.

Continuing with the discussion 60 MeV, κ =1507 mm and at 60.6 MeV, κ =1521 mm with respect to an arbitrary reference point and this gives a difference of 14 mm along the focal plane for a 1% change in energy. According to the conventions used in beam optics the dispersion is measured normal to the optical axis. From Figure 2.15 the angle of the focal plane with respect to this normal was 65.5°and taking the projection of the focal plane along this direction amounts to taking the cosine of this angle (0.4147). The disper-

sion measured normal to the optic axis needs to be scaled by 0.4147 and gives D = 5.8 mm/%, a difference of ~ 6% when compared to the calculated dispersion from Equation B.14. It was known that the effective field boundary used in the beam optics equations was too small, therefore there was less effective field present and less bending of the particles resulting in a lower dispersion than calculated by the other methods that incorporated the true EFB.

Another method can be used based on the Browne-Buchner condition. From Equation (2.12) using 60 MeV, R_m = 0.220 m (this is closer to the true EFB), and a bend radius of 0.242 m, $\Delta\kappa/\Delta p$ = 23.8 mm/MeV and gives a dispersion of 14.3 mm/% measured parallel to the focal plane. Converting this to the usual notation yields D = 5.9 mm/%.

B.3 Simulations and the Transfer Matrix

The following output given in Figure B.1 was produced by *Raytrace* (Kowalski *et al.*) for a magnetic field of 0.5 Tesla, an EFB of 210 mm and an object distance of 215 mm. In the top drawing the initial angular displacement was 50 mr and in the bottom drawing the initial radial displacement was 5 mm In both cases the incident energy was 26.25 MeV. The transfer matrix was in excellent agreement with that produced by *Transport.*

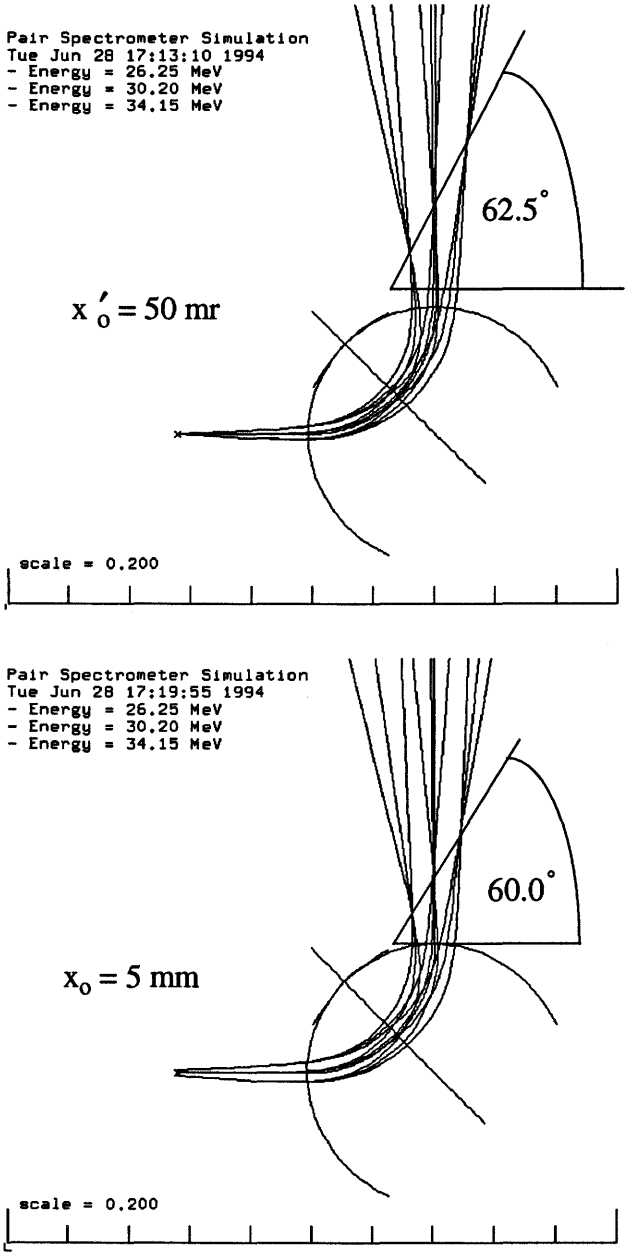

Figure B.2. Sample output from Raytrace.

The transfer matrix for the PS was calculated using *Raytrace* (for the previously stated parameters) and is shown in Equation B.15 and B.16 for the bend and nonbend planes respectively. The transfer matrix accounts for the beam leaving the converter until it

strikes the focal plane. From the formalism in Section 2.2 the transfer matrix was determined and is given in Equation B.17. Differences are due to a non point source in the software codes since the same effective field boundaries were used.

$$R_{PS_x} = \begin{bmatrix} -0.768 & -0.001 & 0.289 \\ -57.150 & -1.416 & 9.354 \\ 0.000 & 0.000 & 1.000 \end{bmatrix} \tag{B.15}$$

$$R_{PS_y} = \begin{bmatrix} 1.550 & 0.079 & 0.000 \\ 23.046 & 1.838 & 0.000 \\ 0.000 & 0.000 & 1.000 \end{bmatrix} \tag{B.16}$$

$$\left(R_{x,\,calc} = \begin{bmatrix} -0.721 & 0.000 & 0.301 \\ -56.213 & -1.388 & 9.837 \\ 0.000 & 0.000 & 1.000 \end{bmatrix} \right), \left(R_{y,\,calc} = \begin{bmatrix} 1.000 & 0.0618 & 0.000 \\ 0.000 & 1.000 & 0.000 \\ 0.000 & 0.000 & 1.000 \end{bmatrix} \right) \tag{B.17}$$

The software package *Transport* (Brown *et al, 1966)* enabled determination of the transfer matrix for the dipole magnet. The following parameters were used in the code:

Beam parameters:

Energy - 26.25 MeV

beam size - 3 × 3 mm

Dipole parameters:

object distance - 21.5 cm

magnetic field strength - 0.5 T

length - 30.67 cm

bend angle - 100.3°

image distance - 9.63 cm.

Figure B.3 gives the input code and complete transfer matrix for the bend and nonbend planes. Those who are familiar with *Transport* will notice the σ (beam) matrix presence. Note that *Transport* gives $R_{12} = 0$ which indicates point to point imaging. There is excellent agreement for the bend planes in all three methods. The analytical equation derived in Equation B.5 gives the same matrix element R_{21} as Equation B.5 to 1 part in 10,000.

```
1TRANSPORT 4/15/83
1
0PAIR SPECTROMETER

0    0
    15.                          11.00000   "MeV "        0.00100 ;
     1.000000        "beam"       0.00000     0.00000     0.00000     0.00000     0.00000    26.25000;
     3.0             "DR1 "       0.21500;
         (dipole 1 >> )
     4.000           "DIP1"       0.30671     5.00000     0.00000;
     3.0             "DR2 "       0.09632;
    13.                           4.00000;
    13.                           1.00000;
0SENTINEL
1PAIR SPECTROMETER

 *BEAM*          1.     "beam"     26.25000 MeV
      0.000 M                                                          0.000   0.000 CM
                                                                       0.000   0.000 MR      0.000
                                                                       0.000   0.000 CM      0.000   0.000
                                                                       0.000   0.000 MR      0.000   0.000   0.000
                                                                       0.000   0.000 CM      0.000   0.000   0.000   0.000
                                                                       0.000   0.000 PC      0.000   0.000   0.000   0.000   0.000
 *DRIFT*         3.     "DR1 "      0.21500 M
      0.215 M
 *BEND*          4.     "DIP1"      0.30671 M        5.00000 KG        0.00000      (     0.175 M   , 100.349 DEG )
      0.522 M
 *DRIFT*         3.     "DR2 "      0.09632 M
      0.618 M
 *TRANSFORM 1*
             -0.72069   0.00000   0.00000   0.00000   0.00000   0.30133
            -56.17448  -1.38739   0.00000   0.00000   0.00000   9.83733
              0.00000   0.00000   1.00000   0.06180   0.00000   0.00000
              0.00000   0.00000   0.00000   1.00000   0.00000   0.00000
             -0.98373  -0.04181   0.00000   0.00000   1.00000  -0.13444
              0.00000   0.00000   0.00000   0.00000   0.00000   1.00000
                                                                       0.000   0.000 CM
                                                                       0.000   0.000 MR      0.000
                                                                       0.000   0.000 CM      0.000   0.000
                                                                       0.000   0.000 MR      0.000   0.000   0.000
                                                                       0.000   0.000 CM      0.000   0.000   0.000   0.000
                                                                       0.000   0.000 PC      0.000   0.000   0.000   0.000   0.000
0*LENGTH*          0.61803 M
```

Figure B.3. Transport output for the PS.

C.1 Energy loss due to collisions of charged particles in Copper

A modified Bethe-Bloch formula was used for determining the energy lost by electrons and positrons in the Copper (Z=29) converters. There is a slight difference in the average energy loss between the two particles (2% @ 100 MeV). The formula used was developed by Berger and Seltzer [Berger and Seltzer, 1964] and is shown in Equation (C.1).

$$-\frac{1}{\rho}\left(\frac{dE}{dx}\right)_{coll} = \frac{2\pi N_A r_0^2 mc^2}{\beta^2}\frac{Z}{A}\left\{\log\left[\frac{\tau^2(\tau+2)}{2\left(\frac{I}{mc^2}\right)^2}\right] + F^{\pm}(\tau) - \delta\right\} \qquad \text{(C.1)}$$

where

$$F(\tau)_{electron} = 1-\beta^2+\frac{\left[\frac{\tau^2}{8}-(2\tau+1)\log 2\right]}{(\tau+1)^2}+ \qquad \text{(C.2)}$$

and

$$F(\tau)_{positron} = 2\log 2-\frac{\beta^2}{12}\left[23+\frac{14}{\tau+2}+\frac{10}{(\tau+2)^2}+\frac{4}{(\tau+2)^3}\right] \qquad \text{(C.3)}$$

where

mc^2 = rest energy (0.510976 MeV)

τ = kinetic energy in units of mc^2

β = velocity/c

Z = atomic number (Z=29)

A = atomic weight (A = 63.546 g/mole)

ρ = density (8.96 g/cm^3)

I = mean excitation energy

δ = density effect correction

N_A=Avogadro's number (6.0222 x 10^{23} atoms/mole)

$r_0^2=(e^2/mc^2)^2$ = 7.94030 x 10^{-26} cm^2

Equation (C.4) gives the energy loss due to radiation. It is obtained from an integration of the bremsstrahlung cross-section times the photon energy over the possible range of energies. The expected energy loss due to collisions (summed with radiation in parenthesis) is given for a single electron in Table C.1.

$$-\left(\frac{dE}{dx}\right)_{rad} = NE_0\Phi_{rad} \qquad \text{(C.4)}$$

where

$$\Phi_{rad} = \frac{1}{E_0}\int h\nu \frac{d\sigma}{d\nu}(E_0, \nu)\, d\nu \qquad \text{(C.5)}$$

Table C.1. Ionization (plus radiation) energy losses as a function of thickness.

Energy [MeV]	Energy lost for 4.55 mm Cu [MeV]	Energy lost for 1.60 mm Cu [MeV]	Energy lost for 1.30 mm Cu [MeV]	Energy lost for 1.25 mm Cu [MeV]	Energy lost for 0.70 mm Cu [MeV]
25.00	6.35 (12.73)	2.23 (4.48)	1.81 (3.64)	1.74 (3.50)	0.98 (1.96)
26.25 (0)	6.37 (13.11)	2.24 (4.61)	1.82 (3.74)	1.75 (3.60)	0.98 (2.02)
27.20 (3)	6.38 (13.37)	2.24 (4.70)	1.82 (3.82)	1.75 (3.67)	0.98 (2.06)
30.20 (1)	6.41 (14.29)	2.26 (5.02)	1.83 (4.08)	1.76 (3.93)	0.98 (2.20)
30.43 (4)	6.42 (14.29)	2.26 (5.05)	1.83 (4.10)	1.76 (3.94)	0.99 (2.20)
34.36 (5)	6.46 (15.54)	2.27 (5.47)	1.85 (4.44)	1.77 (4.27)	0.99 (2.21)
34.40 (2)	6.46 (15.55)	2.27 (5.47)	1.85 (4.44)	1.77 (4.27)	0.99 (2.39)

For two electrons travelling the entire distance of the converter (neglecting the small effect due to positrons) the total energy loss is twice that given in parentheses. For example, in the medium thickness converter (1.60 mm) the expected energy loss in the Cu foil is about 9.0 MeV at 25 MeV. If it is assumed that both charged particles are produced in the middle of the foil, then the average energy loss is that given in brackets for both particles.

D.1 Tagger focal plane energies

The following table is a copy of our lookup table generated from "tageng".

Tagger Field (BO) : 0.479 Tesla

Segment Number	Central Momentum (%)	Central Momentum (MeV/c)	Momentum Spread (MeV/c)	Photon Energy (MeV)	Energy Spread (MeV)
1	-17.92	61.24	+/- 0.27	80.52	+/- 0.27
2	-17.19	61.79	+/- 0.28	79.98	+/- 0.28
3	-16.45	62.34	+/- 0.28	79.42	+/- 0.28
4	-15.70	62.90	+/- 0.28	78.87	+/- 0.28
5	-14.96	63.45	+/- 0.28	78.31	+/- 0.28
6	-14.20	64.02	+/- 0.28	77.75	+/- 0.28
7	-13.45	64.58	+/- 0.28	77.19	+/- 0.28
8	-12.69	65.15	+/- 0.28	76.62	+/- 0.28
9	-11.93	65.72	+/- 0.29	76.05	+/- 0.29
10	-11.16	66.29	+/- 0.29	75.48	+/- 0.29
11	-10.39	66.86	+/- 0.29	74.90	+/- 0.29
12	-9.61	67.44	+/- 0.29	74.32	+/- 0.29
13	-8.83	68.02	+/- 0.29	73.74	+/- 0.29
14	-8.05	68.61	+/- 0.29	73.16	+/- 0.29
15	-7.26	69.20	+/- 0.29	72.57	+/- 0.29
16	-6.47	69.79	+/- 0.30	71.98	+/- 0.30
17	-5.68	70.38	+/- 0.30	71.39	+/- 0.30
18	-4.88	70.98	+/- 0.30	70.79	+/- 0.30
19	-4.07	71.57	+/- 0.30	70.19	+/- 0.30
20	-3.27	72.18	+/- 0.30	69.59	+/- 0.30
21	-2.46	72.78	+/- 0.30	68.98	+/- 0.30
22	-1.64	73.39	+/- 0.30	68.38	+/- 0.30
23	-0.82	74.00	+/- 0.31	67.77	+/- 0.31
24	0.00	74.61	+/- 0.31	67.15	+/- 0.31
25	0.83	75.23	+/- 0.31	66.53	+/- 0.31
26	1.66	75.85	+/- 0.31	65.92	+/- 0.31
27	2.49	76.47	+/- 0.31	65.29	+/- 0.31
28	3.33	77.10	+/- 0.31	64.67	+/- 0.31
29	4.17	77.73	+/- 0.31	64.04	+/- 0.31
30	5.02	78.36	+/- 0.32	63.41	+/- 0.32
31	5.87	78.99	+/- 0.32	62.77	+/- 0.32
32	6.72	79.63	+/- 0.32	62.14	+/- 0.32
33	7.58	80.27	+/- 0.32	61.49	+/- 0.32
34	8.44	80.91	+/- 0.32	60.85	+/- 0.32
35	9.31	81.56	+/- 0.32	60.21	+/- 0.32
36	10.18	82.21	+/- 0.33	59.56	+/- 0.33
37	11.05	82.86	+/- 0.33	58.90	+/- 0.33
38	11.93	83.52	+/- 0.33	58.25	+/- 0.33
39	12.81	84.17	+/- 0.33	57.59	+/- 0.33
40	13.70	84.83	+/- 0.33	56.93	+/- 0.33
41	14.59	85.50	+/- 0.33	56.27	+/- 0.33
42	15.48	86.17	+/- 0.33	55.60	+/- 0.33
43	16.38	86.84	+/- 0.34	54.93	+/- 0.34
44	17.28	87.51	+/- 0.34	54.26	+/- 0.34
45	18.19	88.18	+/- 0.34	53.58	+/- 0.34
46	19.10	88.86	+/- 0.34	52.90	+/- 0.34
47	20.01	89.54	+/- 0.34	52.22	+/- 0.34
48	20.93	90.23	+/- 0.34	51.54	+/- 0.34
49	21.85	90.92	+/- 0.34	50.85	+/- 0.34
50	22.77	91.61	+/- 0.35	50.16	+/- 0.35
51	23.70	92.30	+/- 0.35	49.47	+/- 0.35
52	24.64	93.00	+/- 0.35	48.77	+/- 0.35
53	25.57	93.69	+/- 0.35	48.07	+/- 0.35
54	26.51	94.40	+/- 0.35	47.37	+/- 0.35
55	27.46	95.10	+/- 0.35	46.66	+/- 0.35
56	28.41	95.81	+/- 0.35	45.96	+/- 0.35
57	29.36	96.52	+/- 0.36	45.24	+/- 0.36
58	30.32	97.23	+/- 0.36	44.53	+/- 0.36
59	31.28	97.95	+/- 0.36	43.81	+/- 0.36
60	32.24	98.67	+/- 0.36	43.09	+/- 0.36
61	33.21	99.39	+/- 0.36	42.37	+/- 0.36
62	34.18	100.12	+/- 0.36	41.65	+/- 0.36

Figure D.1. The tagged photon energy range for E_{e^-}=146 MeV.

D.2 Tagger efficiency calculations

The nominal procedure to measure the tagging efficiency is to place a lead glass Cerenkov detector after the collimated photon beam. The lead glass is assumed to be 100% efficient in photon detection. The number of events in the lead glass is compared to the number of recoil electrons seen in the tagger focal plane. The number of tagged photons that make it through the collimator divided by the total number of tagged photons (recoil electrons in the tagger focal plane) is the tagging efficiency.

Efficiency measurements need to be corrected for backgrounds due to air and this can be accomplished with the tagger radiator out condition. Thus every tagging efficiency measurement consists of two parts: one with the radiator in; the other with the radiator out.

As mentioned in the body of the thesis the tagging efficiency was not measured for this test so an absolute efficiency of the PS can not be precisely determined. An estimate, however, can be made based on the beam energy (146 MeV), collimator size (3 x 3 mm, square) and measurement of tagging efficiency under similar conditions. A reasonable figure for the tagging efficiency is $(4 \pm 2)\%$ [Hallin, Vogt, 1994]. A larger collimator will likely be used in future uses of the PS to increase the tagging efficiency.